NASA-CR-54792

HYDRODYNAMIC JOURNAL BEARING PROGRAM

QUARTERLY PROGRESS REPORT NO. 1
For Period : May 29, 1965 Thru July 29, 1965

By

J. D. McHUGH, H. E. NICHOLS,
W. D. C. RICHARDS, and H. C. LEE

prepared for
NATIONAL AERONAUTICS AND SPACE ADMINISTRATION
CONTRACT NAS 3-6479

SPACE POWER AND PROPULSION SECTION
MISSILE AND SPACE DIVISION
GENERAL ELECTRIC
CINCINNATI, OHIO 45215

Requests for copies of this report should be referred to:

National Aeronautics and Space Administration
Office of Scientific and Technical Information
Washington 25, D.C.
Attention: AFSS-A

HYDRODYNAMIC JOURNAL BEARING PROGRAM

QUARTERLY PROGRESS REPORT NO. 1

Covering the Period
May 29, 1965 through July 29, 1965

by
J.D. McHugh and H.E. Nichols
W.D.C. Richards and H. C. Lee

Approved by
E. Schnetzer, Manager
Development Engineering

Prepared for

NATIONAL AERONAUTICS AND SPACE ADMINISTRATION

Contract NAS 3-6479

Technical Management
NASA - Lewis Research Center
Nuclear Power Technology Branch
Joseph P. Joyce, Technical Manager

RESEARCH AND DEVELOPMENT CENTER
SPACE POWER AND PROPULSION SECTION
MISSILE AND SPACE DIVISION
GENERAL ELECTRIC COMPANY
CINCINNATI, OHIO 45215

TABLE OF CONTENTS

TABLE OF CONTENTS - Continued

LIST OF TABLES

LIST OF ILLUSTRATIONS

LIST OF ILLUSTRATIONS

ABSTRACT

The Space Power and Propulsion Section, in cooperation with the Research and Development Center of the General Electric Company, has been under contract since April 29, 1965 to the National Aeronautics and Space Adminstration for the design, fabrication, and testing of journal bearings which possess characteristics required for use in space power systems. Requirements include long term unattended operation under zero "g" conditions using low viscosity lubricants such as potassium at 1200°F.

The program represents a continuation of work carried out under contract NAS 3-2111[18], and involves the testing and evaluation of bearings under conditions of angular and transverse linear misalignment, and non-rigid bearing supports. The 4 pad pivot-pad and the 3-lobed journal bearings shall be tested after the bearing test assembly including instrumentation have demonstrated the ability to obtain the required data.

The program will be a continuation of experimental investigations paralleled by analytical studies. These analytical investigations will compare the physical testing of bearing parameters with results based on theoretical assumptions. The goal of such experiments is to generalize the various bearing parameters thereby extending the usefulness of the results as

design tools. The experimental tool of this program is a high speed test assembly comprised of a rotor and two test bearings which permits interchangeability of bearings and rotor. The lubricant will be distilled water, temperature-controlled to simulate the kinematic viscosity of potassium. The stability behavior of the rotating shaft will be measured with non-contacting Bently inductance gages. (Appendix B).

The specific requirements of the system are:

1.	Shaft speed	3600 to 30,000 rpm
2.	Inlet lubricant temperature	70 to 150°F
3.	Inlet lubricant supply pressure	0 to 150 psia
4.	Bearing linear misalignment	0 to 0.004 $\pm$ 0.0005 in.
5.	Bearing angular misalignment	0 to 400 $\pm$ 12 sec.
6.	Bearing L/D ratio	1
7.	Diametral clearance	0.005 in.

The program will be performed in two tasks, the first of which will be the modification of the existing bearing test assembly and instrumentation and a demonstration of the ability to obtain accurate data. Task II will involve testing and analysis of the 4 pad pivot-pad and 3-lobed bearings.

The present report covers progress during the quarter ending July 29, 1965.

SUMMARY

During this first quarter, test assembly design requirements and the program objectives were defined. Several meetings were held between SPPS, R&DC and NASA personnel.

The available test assembly which was used on the previous program (Contract NAS 3-2111) has been modified to permit dynamic calibration of the Bently inductance type proximity probes in a water environment. A test shaft is supported on two 7207 class 5 preloaded angular contact ball bearings, lubricated with spindle oil. The Bently probes must demonstrate an accuracy of $\pm$ 50 micro-inches and a zero shift within 25 micro-inches to fulfill contract requirements. Bench testing of the Bently probes to improve their accuracy is presently underway. In addition, the testing and monitoring equipment is being set up.

The high speed test rig which will be procured for the ensuing test program has been designed, and the manufacturing drawings have been completed. Instrumentation and measurement equipment has been defined and assemblage of this equipment has begun. In parallel with the above mechanical design and testing effort, analysis of the fundamental rotor-bearing system dynamics has begun.

The program schedule is shown in Figure 1.

Forecast

During the next quarter, ending November 30, 1965, procurement of the hardware for the follow up tests along with the test rig mounting structure and temperature control equipment will be expedited (Reference Figures 6 and 12). Also, preliminary component testing will be undertaken in preparation for assembly into the ensuing test unit. These preliminary component tests include items such as torque calibration, force button calibration, calibration of the Bently probes and check out of all monitoring equipment.

I. INTRODUCTION

For long duration space power missions, a prime requisite is substantial on-board electric power. In the period 1970 - 1975, for example, the National Aeronautics and Space Administration anticipates that power requirements may range from 1 to 10 kilowatts for extended duration.[1] Energy conversion methods have therefore been under intensive study.

A large background of knowledge exists in the conversion of available energy to electrical power through Rankine and Brayton thermodynamic cycles using rotating machinery. Dynamic conversion machines therefore are strong candidates for space power systems to convert solar or nuclear heat energy to electrical power.

To support the rotating shafts of conventional machinery, the designer must select between fluid-film (sliding) and rolling element bearings. When long-life is critical, such as for the steam turbines of central power generating stations, fluid-film bearings are the universal choice.

Well designed fluid-film bearings separate surfaces in relative motion by a thin fluid film, avoiding metal to metal contact and the consequent wear. Such bearings have permitted continuous operation of equipment for over 25 years with no

bearing wear[2]. Fluid-film bearings are therefore a logical choice for supporting the rotating components in space-power systems.

Several potential advantages exist if the thermodynamic cycle fluid used in the space-power system also lubricates the fluid-film bearings. The sealing problem between lubricant and thermodynamic fluid is eliminated; bearing spans may be reduced, reducing weight and raising the critical speed; the allowable operating temperature is higher than with conventional lubricants, hence temperature gradients and cooling requirements are improved, and the complexity of the lubricating system is greatly reduced.

The use of the thermodynamic cycle fluid however is not without potential problem areas. One of these arises from the low viscosity candidate thermodynamic fluids, such as potassium and sodium, and the high speeds of the rotating machinery. It can be anticipated that such bearings will be operating well into the turbulent fluid-film regime. The shaft speeds of space-power systems are comparable to those of conventionally lubricated high speed machinery which borders on turbulent bearing operation. Owing to the much lower viscosity of the space-power system lubricants, however, the transistion speed to turbulent bearing operation is about 30 times lower than comparable conventionally lubricated machinery[3].

In the laminar flow regime, theoretical solutions of plain bearing performance have been well verified by experiments. A completely theoretical approach to turbulence, however, is

prevented by the fact that the number of variables exceeds the number of equations. Therefore, the analysis of bearings in turbulent flow must depend on accurate experimental in-information[4]. Quantitative calculation procedures for turbulent bearing performance have only recently begun to emerge[5], [6], [7], [8]. Much remains to be done before turbulent fluid-film bearing performance calculations become well-established.

Other potential problem areas exist for fluid-film bearings apart from the uncertainty of performance under turbulent conditions. Experience has demonstrated that lightly-loaded, high speed journal bearings can permit a shaft whirling or instability which can limit attainable rotor speed or result in bearing damage[9], [10]. Space vehicles may be required to operate unattended for long periods of time in a zero-gravity environment, resulting in conditions conducive to shaft whirling. The stability of rotors supported on fluid-film bearings is therefore an additional area of concern for space-power systems.

The General Electric Company has conducted under a previous contract, NAS 3-2111, an investigation of rotor-bearing system stability with the fluid-film bearings in turbulent flow. Six different self-acting fluid-film bearings were tested in a special variable speed test assembly to obtain a comparison of rotor

stability and bearing power loss. The parameters which were varied included speed, lubricant viscosity, static and dynamic loads, bearing clearance and rotor mass distribution. A tabulation of the range of variables is shown in Table 1.

Distilled water was chosen as the test fluid to simulate the low viscosity of potential thermodynamic working fluids (sodium and potassium) while permitting relative ease of observation of rotor-bearing performance. Tests were carried out with water temperature ranging from 70°F to 120°F, and no-load bearing radial clearances varying from approximately 0.0005 to 0.0025 inches. As indicated in Figures 2 and 3, the resulting bearing Sommerfeld and Taylor numbers for the water-lubricated tests were comparable to those of a potassium lubricated bearing between 800° and 1300°F, and with clearances between 0.4 and 0.7 those of the water tests.

In the tests conducted under the previous program, neither the three-lobe nor the tilting pad bearing permitted the rotor to exhibit a potentially destructive fractional frequency whirl. All test bearings, however, permitted synchronous shaft orbiting due to residual unbalance. The maximum speed attempted with the three-lobe and tilting pad bearings was 21,500 rpm, and was arbitrarily limited because of the amplitude of the synchronous shaft orbiting.

The present program continues the investigation of the tilting pad and three-lobe bearing under additional test conditions such as variable, deliberate bearing misalignment, non-rigid bearing supports and constraints on pad pivoting of the tilting pad bearing. The shaft residual unbalance will be reduced to a value of 0.1 gram inch or lower to permit higher rotational speeds to be investigated.

The behavior of a rotor on fluid-film bearings is a complex system phenomenon; different rotors on a given set of bearings can be expected to produce different behavior. It is therefore important to separate the bearing component characteristics from the overall system behavior. The bearing characteristics can then be applied to rotor configurations other than the particular one under test. To establish these characteristics, measurements will be made of the dynamic radial force transmitted through the bearing as well as the shaft motion. The dynamic bearing spring and damping coefficients will then be computed from these measurements.

Prior to tests on the three-lobe and tilting pad bearing, the capabilities of the revised and improved test assembly will be demonstrated using the two axial groove test bearing. The repeatability of test data will be evaluated, as well as the ability of the assembly to produce controlled misalignment. When a satisfactory level of performance has been demonstrated, tests will be commenced on the three-lobe and tilting pad bearing types.

II. Rotor-Bearing System Dynamic Analysis

1. Purpose of Analysis

The dynamic behavior of a rotor supported on fluid-film bearings is a complex system phenomenon. The response of a system to a disturbance depends upon the characteristics of the individual components of the system (bearings, rotor, foundation) and the interaction between them. Thus, the rotor response to unbalance depends upon its mass, elasticity, mass distribution and the restoring force and damping in the fluid-film bearings. Analysis shows that the bearing spring and damping characteristics in turn are highly complex, dependent upon shaft speed, bearing geometry and clearances, lubricant properties, the magnitude of steady and dynamic loads (11,12).

Not only is the rotor response to finite unbalance loads dependent upon the bearing dynamic coefficients, but the stability of a well-balanced rotor against fractional-frequency whirl also depends on these coefficients (12). The dynamic bearing properties may be calculated for a given bearing by making simplifying assumptions, i.e., assuming zero tangential velocity of the shaft center and linearizing the spring and damping forces about a steady-state position. When the bearings are operating in the turbulent flow regime, a further uncertainty exists owing to the semi-empirical approach necessary in turbulent analysis.

Some information exists comparing the calculated and measured response of an unbalanced rotor based on linearized theoretical bearing dynamic coefficients (14, 15, 16). No values of dynamic bearing coefficients based on direct measured force and displacement values, however, are reported in the literature for comparison with theoretical values. Such information can be of great value in generalizing test results so that the behavior of other rotor systems may be predicted, including both stability and response to unbalance forces. Moreover, the present program is intended to study the

effect of bearing misalignment; experimental dynamic bearing coefficients will allow quantitative comparison of aligned and misaligned bearing characteristics for dynamic as well as static conditions.

A mathematical model of a rotor-bearing-foundation system has been assumed so as to simulate the bearing test assembly. The equations describing this system have been programmed for computer solution. The program may be used in three different ways:

1. To calculate from experimental data the dynamic bearing spring and damping coefficients producing the observed test rotor response at a particular operating condition.
2. To predict the response (including vibration amplitude) of an arbitrary rotor-bearing-foundation system to unbalance load given either theoretical or experimental dynamic bearing coefficients.
3. To predict the stability threshold of the test rotor, or an arbitrary rotor, given the dynamic bearing coefficients.

Thus, the basic purpose of the analysis is to permit the bearing dynamic characteristics to be determined from the observed overall system behavior, thus providing results of general usefulness. Other important purposes are to provide a tool for guiding the experiments, and to check the validity of linearized bearing coefficients in establishing the response and stability behavior of the test and other rotor configurations.

2. Determination of Bearing Characteristics from Experimental Data

It is assumed that the bearing fluid film characteristics can be described by the first order Taylor expansion of the bearing force change with respect to

shaft center displacement change and velocity (11). Thus, the eight parameter model of bearing film is characterized by the following equations:

$$-F_x = K_{xx}X + C_{xx}\dot{X} + K_{xy}y + C_{xy}\dot{y}$$

$$-F_y = K_{yx}X + C_{yx}\dot{X} + K_{yy}y + C_{yy}\dot{y} \qquad (1)\ *$$

where F's are dynamic film forces and (xy) are journal displacements (with respect to bearings) from an initial steady-state position produced by a steady, unidirectional load. Thus in Figure 3, point 0 represents the steady-state position of the shaft axis with no unbalance load. The x and y directions are any arbitrary coordinate axes intersecting at point 0. For convenience, however, one of the axes may be taken as parallel to the steady applied load direction.

With such a model, the steady-state dynamic response of the rotor-bearing system is harmonic in nature. In the general case, under an unbalance load the locus of the shaft center in the bearings is an ellipse, as shown in Figure 4. The major axis of the ellipse is at an angle with respect to the coordinate axes.

With an elliptical shaft orbit, the displacement and force in the two coordinate directions may be written as:

$$x = x_c \cos \omega t + x_s \sin \omega t \qquad y = y_c \cos \omega t + y_s \sin \omega t$$

$$F_x = F_{xc} \cos \omega t + F_{xs} \sin \omega t \qquad F_y = F_{yc} \cos \omega t + F_{ys} \sin \omega t$$

The more compact and convenient form is:

$$x = Xe^{-i\omega t},\ y = Ye^{-i\omega t},\ F_x = F_X e^{-i\omega t},\ F_y = F_Y e^{-i\omega t}$$

Where $X = X_c + iX_s$, $Y = y_c + iy_s$, $F_X = F_{xc} + i F_{xs}$, $F_Y = F_{yc} + i F_{ys}$

The quantity ω is the shaft rotational frequency for a dynamic load caused by unbalance.

*(Nomenclature in Appendix A)

The elliptical shaft orbit may be written simply using the coordinate axes (x',y') coinciding with the major and minor axes of the ellipse, as shown in Figure 5. Thus,

$$x'(t) = a \cos(\omega t - \phi)$$

$$y'(t) = b \sin(\omega t - \phi)$$

Referring to the coordinate system x,y at an angle α with respect to x',y',

$$x' = x \cos\alpha + y \cos\alpha$$

$$y' = y \cos\alpha - x \sin\alpha$$

and

$$x = \sqrt{x_c^2 + x_s^2} \quad \cos(\omega t - \phi_x)$$

$$y = \sqrt{y_c^2 + y_s^2} \quad \sin(\omega t - \phi_y)$$

This establishes the relationship between (a, b, ϕ, α) and (x_c, x_s, y_c, y_s).

The eight parameter model of the fluid-film force may also be expressed in dimensionless terms and in complex notation as:

$$-\bar{F}_x = (\bar{K}_{xx} - i\,\bar{C}_{xx})\,\bar{X} + (\bar{K}_{xy} - i\,\bar{C}_{xy})\,\bar{Y} = \bar{A}\bar{X} + \bar{B}\bar{Y}$$

$$-\bar{F}_Y = (\bar{K}_{yx} - i\,\bar{C}_{yx})\,\bar{X} + (\bar{K}_{yy} - i\,\bar{C}_{yy})\,\bar{Y} = \bar{C}\bar{X} + \bar{D}\bar{Y}$$

where $\bar{A} = \bar{K}_{xx} - i\,\bar{C}_{xx}$ $\quad \bar{B} = \bar{K}_{xy} - i\,\bar{C}xy$ etc.

$$\bar{F}_{x,y} = \frac{1}{W} F_{x,y}, \quad \bar{K}_{xx} = \frac{C}{W} K_{xx}, \quad \bar{C}_{xx} = \frac{C}{W}\,\omega\, C_{xx} \text{ etc.}$$

The factors C and W have dimensions, length and force, respectively. A common practice is to use the bearing clearance for C and the bearing load for W.

The linearized model of the bearing fluid film requires 8 coefficients to describe the change of force with respect to displacement and velocity in the two coordinate directions. Measurement of forces and displacements in the two coordinate directions, however, yield only four values at one bearing. Two independent sets of measurements are required, which cannot be satisfied by two unbalance levels. One technique to achieve the independent sets of measurements is to apply a given unbalance both symmetrically and anti-symmetrically. The former tends to produce a translatory whirl, in which the shaft axis describes a cylinder. The latter (unsymmetric) unbalance produces a conical whirl, in which the shaft axis locus describes a double cone.

Denoting these independent sets by $(\bar{X}_1, \bar{Y}_1, \bar{F}_{x1}, \bar{F}_{y1})$ and $(\bar{X}_2, \bar{Y}_2, \bar{F}_{x2}, \bar{F}_{y2})$, then

$$\begin{aligned} A\bar{X}_1 + B\bar{Y}_1 &= -\bar{F}_{x1} \\ A\bar{X}_2 + B\bar{Y}_2 &= -\bar{F}_{x2} \\ C\bar{X}_1 + D\bar{Y}_1 &= -\bar{F}_{y1} \\ C\bar{X}_2 + D\bar{Y}_2 &= -\bar{F}_{y2} \end{aligned} \qquad (2)$$

One determines $\bar{A}$, $\bar{B}$, etc. from Equation (2) and then $\bar{K}_{xx}$, $\bar{C}_{xx}$ etc. are obtained. A computer program is currently being written to calculate the eight bearing parameters from input experimental data on forces and displacements

3. Rotor-Bearing System Dynamic Model

Figure 4 shows the rotor-bearing-pedestal system. A flexible shaft is supported on fluid-film bearings possessing stiffness and damping. The bearing housing also possess mass and elastic support. The symmetric rotor has two concentrated masses, each with one-half the total mass and in a distance such

that the moment of mass inertia about the mass center is equal to the transverse moment of inertia of the rotor, that is,

$$(1/2)M\xi^2 b^2 = I_T$$

At the equal distances from the mass center, external forces are applied. The magnitude and direction may be different. The equations of motion are, in vector form,

$$\bar{R}_5 - \bar{R}_3 - (1/2)(1-\xi)(\bar{R}_4 - \bar{R}_3) = -\alpha_{55}M\ddot{\bar{R}}_5 - \alpha_{56}M\ddot{\bar{R}}_6 + \alpha_{51}\bar{Q}_1 + \alpha_{52}\bar{Q}_2$$

$$\bar{R}_6 - \bar{R}_3 - (1/2)(1+\xi)(\bar{R}_4 - \bar{R}_3) = -\alpha_{65}M\ddot{\bar{R}}_5 - \alpha_{66}M\ddot{\bar{R}}_6 + \alpha_{61}\bar{Q}_1 + \alpha_{62}\bar{Q}_2$$

$$-\frac{b}{2}(\eta-1)\bar{Q}_1 - (1/2)b(1-\xi)M\ddot{\bar{R}}_5 - (1/2)b(1+\xi)M\ddot{\bar{R}}_6 + b\bar{F}_2 + (1/2)b(1+\eta)\bar{Q}_2 = 0 \qquad (3)$$

$$\frac{b}{2}(\eta-1)\bar{Q}_2 + \frac{b}{2}(1-\xi)M\ddot{\bar{R}}_6 + \frac{b}{2}(1+\xi)M\ddot{\bar{R}}_5 - b\bar{F}_1 - \frac{b}{2}(1+\eta)\bar{Q}_1 = 0$$

$$M\ddot{\bar{R}}_1 + k\bar{R}_1 - \bar{F}_1 = 0$$

$$M\ddot{\bar{R}}_2 + k\bar{R}_2 - \bar{F}_2 = 0$$

where: $\bar{R}_j = x_j\bar{i} + \bar{y}_j\bar{j}$ $\qquad j = 1,2,.....6$

$\bar{F}_r = \bar{i}F_{xr} + \bar{j}\bar{F}_{yr}$ $\qquad r = 1,2$

The influence coefficients α_{ab} represents deflection at a due to unit force at b. The external forces are denoted by Q's. The film forces F's are:

$$-F_{x1} = K_{xx}(X_3 - X_1) + C_{xx}(\dot{X}_3 - \dot{X}_1) + K_{xy}(y_3 - y_1) + C_{xy}(\dot{y}_3 - \dot{y}_1)$$

$$-F_{x2} = K_{xx}(X_4 - X_2) + C_{xx}(\dot{X}_4 - \dot{X}_2) + K_{xy}(y_4 - y_2) + C_{xy}(\dot{y}_4 - \dot{y}_2)$$

$$-F_{y1} = K_{yx}(X_3 - X_1) + C_{yx}(\dot{X}_3 - \dot{X}_1) + K_{yy}(y_3 - y_1) + C_{yy}(\dot{y}_3 - \dot{y}_1)$$

$$-F_{y2} = K_{yx}(x_4 - x_2) + C_{yx}(\dot{x}_4 - \dot{x}_2) + K_{yy}(y_4 - y_2) + C_{yy}(\dot{y}_4 - \dot{y}_2)$$

The subscripts are station numbers as shown in Figure 2. The use of symmetry reduces Equations (3) to:

$$\begin{aligned} &\alpha_1 M\ddot{\bar{R}}_o + \bar{R}_o - \bar{R}_s = \alpha_2 \bar{Q}_R \\ &M\ddot{\bar{R}}_o - \bar{F}_R = \bar{Q}_R \\ &m\ddot{\bar{R}}_b + k\bar{R}_b - \bar{F}_R = 0 \end{aligned} \qquad (4\text{-A})$$

$$\begin{aligned} &\alpha_3 M\ddot{\bar{W}}_o + \bar{W}_o - \xi\bar{W}_s = \alpha_4 \bar{Q}_w \\ &\xi M\ddot{\bar{W}}_o - \bar{F}_w = \eta\bar{Q}_w \\ &m\ddot{\bar{W}}_b + k\bar{W}_b - \bar{F}_w = 0 \end{aligned} \qquad (4\text{-B})$$

Where $\alpha_1 = \alpha_{55} + \alpha_{56}$, $\alpha_2 = \alpha_{51} + \alpha_{52}$, $\alpha_3 = \alpha_{55} - \alpha_{56}$, $\alpha_4 = \alpha_{51} - \alpha_{52}$

$$\bar{R}_o = \bar{i}\,(x_5+x_6) + \bar{j}(y_5+y_6) \qquad \bar{R}_s = \bar{i}(x_3+x_4) + \bar{j}(y_3+y_4)$$

$$\bar{R}_b = \bar{i}\,(x_1+x_2) + \bar{j}(y_1+y_2) \qquad \bar{W}_o = \bar{i}\,(x_6-x_5) + \bar{j}(y_6-y_5)$$

$$\bar{W}_s = \bar{i}\,(x_4-x_3) + \bar{j}(y_4-y_3) \qquad \bar{W}_b = \bar{i}\,(x_2-x_1) + \bar{j}(y_2-y_1)$$

$$\bar{Q}_R = \bar{i}\,(Q_{x1}+Q_{x2}) + \bar{j}(Q_{x1}+Q_{x2}) \qquad \bar{Q}_w = \bar{i}(Q_{x2}-Q_{x1}) + \bar{j}(Q_{y2}-Q_{y1})$$

$$\bar{F}_R = \bar{i}\,F_{x1}+F_{x2}) + \bar{j}\,(F_{y1}+F_{y2}) \qquad \bar{F}_w = \bar{i}\,(F_{x2}-F_{x1}) + \bar{j}\,(F_{y2}-F_{y1})$$

Since equations (4A) can be obtained from (4B) by replaxing α_3, α_4, ξ, η, and $\bar{Q}_w$ by α_1, α_2, 1, 1, and $\bar{Q}_R$ respectively, one only needs to solve equations (4B).

4. Stability analysis

The condition at threshold of instability can be found by taking homogeneous equations of (4B) and letting $\bar{R}(t) = \tilde{R}e^{-ivt}$. The elimination of $\bar{W}_o$ and $\bar{W}_b$, and the vanishing determinant of scaler equations gives (in dimensionless quantities)

$$\bar{R} = \frac{\bar{K}_{xx}\bar{C}_{yy} + \bar{C}_{xx}\bar{K}_{yy} - \bar{C}_{xy}\bar{K}_{yx} - \bar{C}_{yx}\bar{K}_{xy}}{\bar{C}_{xx} + \bar{C}_{yy}} \tag{5A}$$

$$\gamma^2 = \frac{(\bar{K}_{xx}-\bar{R})(\bar{K}_{yy}-\bar{R}) - \bar{K}_{xy}\bar{K}_{yx}}{\bar{C}_{xx}\bar{C}_{yy} - \bar{C}_{yx}\bar{C}_{xy}} \tag{5B}$$

$$\bar{R} = \frac{\bar{R}_s}{1 + \bar{R}_b \bar{R}_s} \tag{5C}$$

$$\bar{R}_b = \frac{1/\bar{k}}{1 - \gamma^2 S^2 S_n^2} \tag{5D}$$

$$\bar{R}_s = \frac{\frac{\xi^2}{\alpha_3}\gamma^2 S^2}{1 - \gamma^2 S^2} \tag{5E}$$

Where: $\gamma = \frac{\nu}{w}$, $S = \frac{\omega}{\omega_{ns}}$, $\omega_{ns}^2 = \frac{1}{\gamma_3 M}$ $S_n^2 = \frac{k\gamma_3 M}{m}$

$\bar{k} = \frac{c}{W}k$ $\bar{K}_{xx} = \frac{C}{W}K_{xx}$ $\bar{C}_{xx} = \frac{c}{W}\omega C_{xx}$ etc

The quantity ω is the rotating speed at the threshold of instability. Equations (5A-B) give values of $\bar{k}$ and γ and then (5C-E) determines the value of S at the threshold of instability.

5. Response Calculations

For the response to $\bar{Q}_w(t) = \bar{Q}_w e^{-i\omega t}$, the solution takes the form $\bar{R}(t) = \bar{R}e^{-i\omega t}$ and Equations (4B) can be solved by elimination. The results are:

$$\frac{1}{C}(U_s - U_b) = \frac{1}{\Delta}\frac{\bar{R}}{\bar{R}_s}\left(\eta + \frac{\bar{\alpha}_4}{\xi}\bar{R}_s\right)\left[(\bar{D}-\bar{R})\bar{Q}_u - \bar{B}\bar{Q}_v\right] \tag{6}$$

$$\frac{1}{C}(V_s - V_b) = \frac{1}{\Delta}\frac{\bar{R}}{\bar{R}_s}\left(\eta + \frac{\bar{\alpha}_4}{\xi}\bar{R}_s\right)\left[\bar{C}\bar{Q}_u - (\bar{A}-\bar{R})\bar{Q}_v\right]$$

Where:

$$\Delta = (\bar{A}-\bar{R})\,(\bar{D}-\bar{R}) - \bar{C}\bar{B}$$

$$\bar{Q}_u = \frac{1}{W}\,(Q_{x2}-Q_{x1}) \quad , \quad \bar{Q}_v = \frac{1}{W}\,(Q_{y2}-Q_{y1})$$

$$\bar{A} = \bar{K}_{xx} - i\,\bar{C}_{xx} \quad \text{etc.}$$

Note that $\gamma = 1$ for $\bar{R}$, $\bar{R}_b$ and $\bar{R}_s$. Also,

$$\frac{1}{C}\,U_s = \frac{\bar{N}}{\bar{R}_s}\cdot\left[\ \frac{1}{C}\,(U_s-U_b) - R_b\left(\eta + \frac{\bar{\alpha}_4}{\xi}\,\bar{R}_s\right)\,\bar{Q}_u\ \right] \tag{7}$$

$$\frac{1}{C}\,V_s = \frac{R}{\bar{R}_s}\left[\ \frac{1}{C}\,(V_s-V_b) - R_b\left(\eta + \frac{\bar{\alpha}_4}{\xi}\,s\right)\ \bar{Q}_v\ \right]$$

$$\frac{1}{C}\,U_o = \frac{1}{1-S^2}\left[\ \xi\,U_s + \bar{\alpha}_4\,\bar{Q}_u\ \right] \tag{8}$$

$$\frac{1}{C}\,V_o = \frac{1}{1-S^2}\left[\ \xi\,V_s + \bar{\alpha}_4\,\bar{Q}_v\ \right]$$

For the unbalances,

$$Q_{x1} = m_o\delta_o\omega^2 \qquad Q_{y1} = i\,m_o\delta_o\omega^2$$

$$Q_{x2} = m_1\delta_1\omega^2(\cos\varphi + i\sin\varphi) \qquad Q_{y2} = m_1\delta_1\omega^2(-\sin\varphi + i\cos\varphi)$$

where m_o and m_1 are unbalance masses, δ_o and δ_1, are unbalance eccentricity and φ is the phase lag of m_1 from m_o.

Then

$$\bar{Q}_x = \frac{1}{W}\,M_o\delta_o\omega^2\left[\left(1 + \frac{m_1\delta_1}{m_o\delta_o}\cos\varphi + i\,\frac{m_1\delta_1}{m_o\delta_o}\cos\varphi\right.\right. \tag{9}$$

$$\bar{Q}_y = i\,\bar{Q}_x$$

$$\bar{Q}_u = \frac{m_o\delta_o\omega^2}{W}\left(\frac{m_1\delta_1}{m_o\delta_o}\cos\varphi - 1\right) + i\,\frac{m_1\delta_1}{m_o\delta_o}\sin\varphi \tag{10}$$

$$\bar{Q}_v = i\,\bar{Q}_u$$

III. MECHANICAL DESIGN

During this quarter, several mechanical design modifications to the previously used test rig were considered for the journal bearing test rig assembly. The selected design was finalized, and detail manufacturing drawings of its components are essentially complete. In addition, manufacturing drawings required to convert the test rig used on the previous program (NASA Contract NAS 3-2111) to a rig for the development and proof testing of Bently gages were completed. The resulting shop work is presently underway.

Bearing Test Rig Design

In the evolution of the test rig design, several arrangements were considered, based upon the following general requirements:

1. Adjustability for obtaining controlled angular and transverse misalignment between test bearings without major disassembly of the test rig.

2. Ability to control and vary the flexibility of the test bearing mounts, and to measure bearing reaction forces.

3. Provide an accurate means for checking bearing alignment.

4. Ability to establish gage-zero readings and calibration of shaft proximity gages after test rig assembly, and between tests.

5. Make use of existing test rig hardware where possible by modifying parts, and maintain simplicity of assembly.

One design approach for obtaining misalignment employed the use of eccentric rabbets between the main housing and the lower test bearing assembly for transverse misalignment, and wedge-shaped spacers between flanges for angular misalignment. This configuration required some disassembly of the test rig for adjustment, and was therefore rejected. An alternate design involved mounting the test bearings in spindle assemblies, which in turn were mounted in the upper and lower flanges of the test rig, and at right angles to each other. Because of difficulty in obtaining alignment, this was also rejected.

Figure 6 shows the assembly drawing of the adopted design. A pictorial view of the test rig is depicted in Figure 7. The upper test bearing is mounted centrally in the test rig by rabbeted flanges. The lower bearing housing subassembly can be either aligned or misaligned with the fixed upper bearing by use of four adjustable clamps. This technique allows the upper bearing to be installed in the housing with its centerline considered as the datum or zero position. The lower bearing will then be assembled and aligned with it. Misalignment of the lower bearing is accomplished by controlling the adjustment screws of the adjustment ring assembly. The bearing center distance is 12.5

inches, and the test shaft is driven by a variable speed electric motor through a quill shaft assembly. This drive is identical to that used during the previous program (Contract NAS 3-2111). Radial side loads are imposed on the test shaft by the same pad loader bearings which were employed previously. The shaft will be initially balanced, and then purposely unbalanced in controlled amounts during test by balance disks located on its ends.

Assembly and Alignment

The major problem in the test rig assembly will be to obtain very accurate initial alignment of the bearings, and reliable verification of their alignment. This must be gotten during assembly, and requires special techniques. A twofold approach for initial alignment has been investigated and pursued in design. One involves the use of precision-made, expandable dummy shafts to accurately extend the centerline of the upper test bearing through the housing of the lower, to allow the second bearing to be aligned with it. An additional approach uses the Proficorder available at R&DC to entend a rotable shaft through both test bearings and obtain their alignment with it to a high degree of precision. This basic technique is used in aligning the NASA gas bearing test rigs.

Initial bearing alignment will be obtained by installing an expandable dummy shaft while assembling the test rig. After

obtaining its best alignment, the rig will be mounted on the Proficorder for final alignment. The dummy shafts will also be used for interim alignment checks during testing to minimize the need for nearly complete disassembly and removal of the test rig from the test installation, as required for use of the Proficorder. In aligning the bearings with the dummy shaft, the Bently proximity gages themselves will be employed as alignment tools. The lower housing assembly will be set up on the Proficorder with a short stub shaft inserted along the centerline to simulate the actual test shaft. The gages will be installed and readings with this"zero" aligned condition will be taken. The test rig will then be assembled with the expandable dummy shaft mounted through this bearing. The adjustable bearing will be then moved so as to repeat these zero readings on the Bently gages, corresponding to the proper aligned condition. This alignment accuracy using the dummy shaft is estimated to be about $\pm$ 200 micro-inches.

definition of true bearing axis	$\pm$ 10 micro-inches
concentricity of ends of alignment arbor	$\pm$ 100 micro-inches
statistical error in gage reading	$\pm$ 30 micro-inches
error in setting-up and checking 8 gages	$\pm$ 50 micro-inches

Of the intended 0.004 inch transverse misalignment, this 200 micro-inch comprises 5% of the total misalignment. In addition, compared with the loss of radial clearance at the bearing ends

caused by the 400 seconds-of-arc intentional misalignment (which is 0.001188 in.) this 200 micro-inch transverse alignment inaccuracy comprises 0.84% of the total required angular misalignment.

Following initial alignment, the entire test rig will be set up on the Proficorder shown schematically in Figure 8. This is a precision measuring device containing a circular tracing spindle with a surface sensing probe capable of tracing circular paths with deviations less than 3 micro-inches from perfect roundness. The work is mounted on a horizontal table which can travel vertically. Read-out and/or plotted charts of the bearing alignment can be obtained from the console accompanying the sensing mechanism.

In aligning the test rig, the rotable shaft with a longitudinally sliding sensing-head is extended downward through the assembled test rig, and alignment is obtained by rotating the sensing probe on the test bearings and adjusting the test rig as necessary until it is aligned with the Proficorder spindle. The test rig is then removed from the Proficorder and its actual test shaft is installed. The alignment which can be obtained on the Proficorder is estimated to be 100 micro-inches as follows:

Definition of true center of Upper Bearing:	Top Plane	25 micro-inches
	Lower Plane	25 micro-inches
Definition of true center of Lower Bearing:	Top Plane	25 micro-inches
	Lower Plane	25 micro-inches

After installing the test rig into its supporting facility, adjustments in alignment from test to test can be made using the contact position sensor probes (Electro Jet Cartridges) indicated in Figure 7, or the test rig can be removed from its test-mounting, set up on the Proficorder once more, and aligned as desired using the above technique.

Force Gages*

Shown in Figure 9 are the "force gages" which are used to hold the bearing and its housing in the assembly, and allow for adjustability of their spring constants. Eight such buttons are used on each bearing, four on each side of the bearing, and located in the same transverse plane as the Bently gages. The buttons are spaced alternately between the Bently gages, and measure the bearing loads by strain gages. The force button basically comprises a diaphragm element with a strain gage attached to its back face which measures the flexure of the diaphragm under load. The force buttons hold the bearing in position and are loaded by belleville springs forced downward by a threaded loading nut (Figure 9).

Bently Gages

A number of Bently gage holders and gage installation designs were also investigated. Figure 6 and 7 show the gages installed in

*Prior usage referenced in the following report:
Bearing Atenuation Experimental Evaluation - By: J.D. McHugh and J.W. Lund, Report of August 28, 1961, Contract No. NO bs 78930

the test rig, and Figure 10 shows an enlarged view of the gage holder assembly and its associated parts. The gage holder extends out through the wall of the main test rig, and can be assembled from outside. The gage is held rigidly by a locking collet assembly pulled tightly into the sleeve of the gage holder (Figure 10). The entire assembly is threaded into the inner bearing housing. Provisions have been made for a curtain of air to be flowed through the gage holder and out into the vicinity of the gage tip as protection against excess moisture in the sensing area. This air is introduced into an annulus at the outer extremity of the gage, and flows radially inward through a series of holes machined into the gage holder. In addition to the air curtain, a teflon cap will be applied to each gage tip to minimize the deleterious effects of water on gage sensitivity. The depth of the gage itself is adjustable through the sliding sleeve held by the collet.

Contact Position Sensors

The contact position sensors used to monitor the misalignment motions are used in the same manner as a dial indicator, by maintaining contact with the housing and providing an electrical signal corresponding to movements to the gage tip. These are inductance-type gages.

Figure 11 shows the proposed thermocouple and pressure tap locations through-out the test rig. Data obtained from the therm-

ocouples will be used to control the temperature of the test rig to eliminate differential thermal expansion error. This temperature control is discussed below.

Test Rig Installation

In parallel with the test rig design effort, basic plans for mounting and for temperature control of the test rig have been underway. Figure 12 shows a manufacturing drawing of the proposed means for mounting the test rig. It is hung in a vertical position and suspended from its top flange through three rubber mounts, in turn supported by three vertical columns. The drive motor is above the test rig, in the same manner as during the previous test program. The mounting stand is hinged at a point below the test rig to allow it to be tilted into the horizontal position for any necessary assembly, disassembly, or required work on either drive motor or test rig. The test rig support columns double as air manifolds for the loader bearings and Bently gage purge.

Figure 12 also shows the proposed casing to be put around the test rig and mounting stand. Its purpose is that of temperature control of the test rig to within closely prescribed limits to minimize its differential thermal expansion. The casing comprises three clam-shell cylindrical segments of sheet metal covers, backed with thermal insulation. Each clam-shell segment is equipped with electrical heating elements on its inner surface to provide radiant and convective heat to the test rig as required.

Procurement Status

At this time, the drafting work on the main test rig is about 90% complete. The layout drawing is finished, and all detail manufacturing drawings have been made. However, minor corrections have to be made and detailed checking of their dimensions has yet to be completed. Also, detail drawings of the installation equipment are not complete.

IV. INSTRUMENTATION AND MEASUREMENTS

The previous discussion of rotor-bearing dynamic analysis has shown that the system response to dynamic load depends upon the fluid film bearing characteristics and the geometric configuration such as the L/D ratio. From experimental observations on the system response for known imposed conditions, the fluid-film characteristics can then be calculated. Thus, it is then possible to extend the experimental results to cover rotor configurations other than the particular one under test and to provide a useful quantitative measure of the effects of bearing misalignment.

The information which is needed to permit such calculation is: the amplitude of shaft rotor-frequency vibration at a given plane transverse to the shaft centerline in two mutually orthogonal directions in that plane; the phase angle between the motion in the x and y directions with respect to the force produced by the rotor unbalance; the amplitude of this transmitted force at rotor frequency in each of two mutually orthogonal directions; the phase angle between each of the dynamic force components and the unbalance. This is represented schematically in Figure 13.

As indicated previously, shaft displacement in the x and y directions will be measured by two pairs of non-contacting, eddy-current Bently inductance gages opposed in a push-pull arrangement

which will cancel symmetrical effects. Each of the two test bearings will have two planes of measurement for detection of shaft slope within the bearing. A total of eight pairs of such opposed gages is therefore provided for shaft rotor detection.

The motion detection system consists of a regulated D.C. power supply (Appendix B); a sensing head in proximity to the shaft; and a distance detector unit which converts the regulated D.C. supply voltage into a high frequency supply for the sensing head and provides the output signal in response to a change in displacement. To provide a push-pull arrangement for the gages, one of the detector units of the pair is designed to produce a reversed output voltage for a given shaft motion. The output of the two detector units is then algebraically summed in a summing amplifier and the output signal fed into appropriate read-out equipment. A schematic diagram of the shaft displacement detection system is given in Figure 14.

Several different read-out instruments will be used in evaluating shaft displacement data. For steady state, non-orbiting shaft positions, the output voltage will be measured with a precision differential D.C. voltmeter. When the shaft center is orbiting, the x and y components of the displacement at rotor frequency will be measured with a conventional harmonic wave analyzer. Visual observation of the shaft center orbital

path will be obtained from a dual trace oscilloscope, which can permit two simultaneous orbital paths to be observed on one screen.

The phase relationship between the x and y displacement vectors and the unbalance vector can be measured in two different ways. First, it is necessary to know the angular position of the deliberate unbalance relative to the shaft and the residual unbalance. Assuming the shaft itself to be balanced i.e. negligible residual unbalance, unbalance is introduced by means of the eccenters shown in Figure 15. As the discs are rotated relative to one another an angle θ from the zero unbalance position, an unbalance $W\bar{y}\ \theta$ is introduced. The ratio of this unbalance to the maximum unbalance $W\bar{y}_m$ is given by the expression:

$$\frac{W\bar{y}_\theta}{W\bar{y}_m} = \sqrt{\frac{2}{2}} \left[1 - \text{Cos } \theta \right]^{1/2}$$

The previous equation is plotted in Figure 16, which also defines the displacement angle θ.

Measurements of maximum unbalance described in Reference 4 show a maximum unbalance $W\bar{y}_m = 35.2$ gram inches, which compares well with a calculated value of 36.3 gram inches.

Both the amplitude and angular position of the center of gravity of the shaft assembly vary as the eccenter disks are

rotated. It can be shown that the angular position φ of the mass center of the disks is given by:

$$\tan \varphi = (1 - \cos \theta) / \sin \theta$$

Where the angle θ is as previously defined (Reference Figure 16 and the angle φ is measured from the same axis and in the same direction as θ. A plot of the previous expression is given in Figure 17.

Thus, for a given angular setting of the disks, both the magnitude and position of the unbalance are known relative to the rotating shaft. It then is possible to establish when the unbalance vector rotates past a fixed point on the test rig casing. An interruption on one of the eccenter discs is sensed by a magnetic pick-up. The signal provided by the magnetic pick-up can be used to intensify the "Z axis" of the oscilloscope trace of displacement versus time, as shown schematically in Figure 13. The phase angle between unbalance and displacement (or force) can then be determined for each of the displacement or force traces in turn.

It should be noted that the "Z" axis scope intensification will not in general coincide with the unbalance vector position, as shown schematically in Figure 13. Depending upon the magnitude of unbalance selected, a fixed angle will exist between the time marker and the unbalance angle which must be taken into account.

An alternative method may also be used to establish phase angle between the unbalance vector and displacement or force vectors. Rather than establishing the phase angle of each trace in turn, the relative phase angles of the x and y displacement or force traces may then be measured as described previously.

Dynamic force measurements will be made using strain-gaged transducers preloaded against the bearing shell. In a given axial plane, one pair of the transducers are diametrically opposed, and a similar pair is oriented at 90° to the first pair of transducers. The bearing shell is supported at two planes by a total of eight such force gages.

Figure 18 illustrates the force vector diagram when the fluid film is transmitting a dynamic load. The vector sum of the forces sensed by the load cells are equal and opposite to the fluid film force F_t, since the shell is in equilibrium. The force F_t can be resolved into a static (or unidirectional) component W and a dynamic component F_d as shown in Figure 18. Thus the output signal from the pairs of gages can be combined to give the total force magnitude and direction at any instant by displaying the two components on an oscilloscope. Alternatively, the individual components in the X and Y directions can be measured.

In the system previously described, the force signals produced by the gages 180° apart are subtracted to yield one component

of the bearing force; the second set of gages are similarly subtracted to give the remaining force component. A simplification of this sytem can be obtained, however, by electrically subtracting the output signal of opposed gages so as to give a signal proportional to the difference between the loads sensed by each of the gages. A block diagram of the instrumentation is shown in Figure 19.

Torque input to the test shaft is measured with a special non-contacting instrumentation system detecting the twist in the long, thin drive shaft. Details of this system are given in Reference 5 and a schematic diagram is shown in Figure 20.

The system detects the phase shift between two toothed wheels at opposite ends of the thin drive shaft. Calibration of the system is obtained by mounting the two toothed disks on a rigid shaft extension of the motor. The disks were rotated relative to one another preset amounts and the torque output meter readings later at various speeds. Figure 21 shows the resulting calibration curve.

Other instrumentation to be used in the collection of data is conventional. It includes an electronic frequency counter sensing the once-per-revolution pulse from an electromagnetic pick-up mounted adjacent to one eccenter; multi-point temperature recorder for lubricant inlet and exit temperature;

a lubricant temperature controller; rotameters for lubricant flow rate measurements; bourdon gages for air and water pressure measurements. These devices are also listed in Appendix B - List of Instrumentation.

V. TESTING SUB-TASKS

In parallel with the design and manufacture of the main test rig, a number of tests are being set up and performed to check-out and establish the functional characteristics of the Bently gages, force pickups, and to measure loader bearing viscous friction torque.

Shaft Displacement Gage Evaluation

Measurements of shaft motion under static and dynamic load are critical to the evaluation of bearing-rotor performance. It is therefore worthwhile to review the reasons for selection of inductance gages as the shaft sensing element; their calibration; performance in the test rig; short comings; and potential improvements.

In the previous bearing investigation, a comparative evaluation test (Reference 6) was conducted between the eddy-current inductance gage and a capacitance gage in measuring shaft runout in a humid environment simulating that of the test rig. When the capacitance probe became wet its signal could not be restored by blowing air around the sensing tip. The eddy-current inductance gage was not affected. In addition, the inductance gage displayed the further advantages of a high and adjustable sensitivity, requiring no amplification of the signal for display on an oscilloscope; linearity within 1% and the ability to choose a large gap (greater than 0.010 inches) between

probe end and shaft, decreasing the probability of damage from the orbiting shaft.

In these comparative tests, the inductance gage was placed adjacent to a rotating mild steel shaft to indicate shaft run-out. Oscillogram traces obtained showed sharp spikes not attributable to a changing gap between the probe and the shaft. Further investigation revealed that the signal spikes coincided with definite small portions of the shaft circumference over which the motion measurements were made. Since the eddy-current gage depends upon the electrical resistance of the sensed material, the sensor was presumably detecting local flaws or inhomogeneities in the material. In view of its superior stability in a humid atmosphere however, the inductance gage was chosen as the shaft displacement sensor despite this one disadvantage.

To investigate the possible magnitude of calibration error due to such potential flaws in the actual stainless steel test shaft, static calibration of the gages was conducted at ten different locations on the shaft surface. These data are reported in Reference 4. The procedure employed in effect determined the slope of the curve of sensor output voltage versus change in gap between the probe and shaft. The standard deviation of the calibration data was found to be only 21 micro-inches, indicating a uniform sensitivity for the probe-shaft combination.

Subsequent in place calibration checks were made in which the displacement of the non-rotating shaft was varied in increments. Measurements made simultaneously with both the inductance gage and an electronic contacting probe in the test assembly showed reasonable agreement with an average difference of only 76 micro-inches for 21 readings.

The effect of water on non-rotating shaft displacement measurements was also investigated. It was found that an air supply pressure of 6 psig at the gage manifold was sufficient to protect the gages against a 10 psig lubricant supply pressure; an average difference of only 40 micro-inches existed between measurements made with and without lubricant flow.

Despite these optimistic indications of accuracy, the data of eccentricity ratio and attitude angle was found to exhibit considerable scatter. This is attributed primarily to the shift in gage zero, i.e., the output of the gage sensor corresponding to the shaft concentric with the bearing. Figure 22 illustrates the observed gage zero shift, as evidenced by traces of shaft orbit during half-frequency whirl at two different speeds. The similarity of the orbit curves is evidence of a similar calibration sensitivity. The sizes of the orbits are compatible with the possible orbit size predicted from static calibration curves. The apparent center of the two orbits, however, has changed between the two test conditions. The effect is similar to that which would

occur if the displacement probe were to move away from the shaft a small amount. The shift in apparent zero is not identical for both gages, which are 90° apart.

Static calibration checks of the original calibration following testing in general showed satisfactory repetition. The apparent shift in gage zero therefore appears to be a speed related phenomenon which could not show up in the preliminary gage evaluation. Temperature gradients changing with speed, for example, can cause such zero shifts.

To identify the cause of this apparent zero shift and improve the accuracy of shaft displacement measurements, a number of steps are being taken. As indicated previously, the test rig has been designed to permit opposed gages to measure shaft displacement in a given direction. Opposed gages can eliminate symmetrical effects due to temperature, centrifugal force or shaft surface speed. Also, temperature gradients within the test rig will be reduced by raising the external ambient temperature surrounding the test rig casing to correspond with lubricant temperature.

Improvements to the sensor-shaft calibration are also being evaluated. One such step is eliminating the probe sensitivity to water droplets. Tests have shown that an air curtain can protect the gage sensing tip when the shaft is stationary. It is possible, however, that the air protection is ineffective against water when the shaft is rotating at high speeds.

Figure 23 shows the effect of immersion in water upon the static calibration curve. It will be seen that immersion in water changes substantially the probe-to-shaft clearance for a given voltage with little change in the curve slope, i.e., sensitivity. It will also be seen that little effect is observed between "dry" calibration and with the probe immersed in a silicone oil. Shielding of the probe by means of a Teflon cap has been found to reduce the effect of water upon the probe static calibration, as shown by Figure 24. The differences between wet and dry static calibrations were not distinguishable, in sharp contrast to the tests without the protecting cap.

Bently Gage Checkout Test Rig

To provide for adequate checkout and verification of the accuracy of the Bently gages in the water environment, prior to installing them in the main test rig, a program of testing the gages in the previously used test rig (Contract NAS 3-2111) is underway.

It is planned to evaluate the effectiveness of the Teflon shielding cap when the shaft is rotating in the test rig and with lubricating water and/or oil supplied to the test bearings. The test shaft will be supported on MRC #7207, Class 5 angular contact bearings to establish a reference position for the gages. Opposed Bently gage sensors will be installed to measure shaft center position adjacent to the bearings. With such an arrangement,

it should then be possible to assess the gage improvements (i.e. opposed probes, teflon tips), in a dynamic evaluation from 3600 to 30,000 rpm.

The rig for this testing is shown in Figure 25. The test shaft is held in two axially pre-loaded angular contact bearings which are oil-lubricated. The lube oil is discarded with the water used in the test. This rig is designed for operation over the full speed range of 3600 to 30,000 rpm. At this time the detail manufacturing drawings of the components for the test rig modification have been released, and fabrication of the parts is about 90% complete.

Effects of Shaft Inhomogeneities

Means for minimizing calibration errors due to shaft flaws or inhomogeneities are also being thoroughly investigated. Figure 26 is a photograph of the basic calibration device. The stainless steel test shaft is mounted on lathe centers. A dual micrometer head carrying the inductance gage and a standard is attached to the lathe bed. The micrometer head permits traversing either along the axis of the shaft or normal to it in 0.0001 inch increments. Displacement of the probe relative to the shaft is measured by a contacting probe (Sheffield Electrojet Sensor with Accutron amplifier direct read out) calibrated against Hoke gage blocks. Adjacent to the contacting probe (standard) is the inductance gage whose output is being calibrated versus shaft

displacement. Output voltage is measured on a high precision differential voltmeter. The set-up permits a given gap to be maintained between the inductance probe and the shaft limited only by the tolerance of the shaft fabrication so that the effect of flaws upon output voltage can be established.

Figure 27 shows the maximum shift in the calibration curve which existed along the circumference of the test shaft used in the previous program. It will be seen that the slopes of the extreme calibration curves are nearly identical. They are separated, however, by an apparent distance of 300 micro-inches. Thus, the clearance between shaft and bearing can be established accurately by back and forth motion of the shaft for either extreme. The zero position of the gage (i.e., the output voltage of the gage when the shaft and bearing are concentric) however, will depend upon the particular spot on the shaft which is being sensed by the gages.

Similar measurements were carried out using the calibration device on a brass shaft; a chrome plated steel shaft; and bushings plated with nickel and silver with the object of producing a homogeneous surface for the gages to sense. Among these tests, the stainless steel bushing plated with 0.003 inch silver displayed only an apparent 50 micro-inch zero shift when evaluated at 6 different axial stations. Such an apparent shift could be accounted for by variation in the plating thickness on the bushing.

To produce the maximum uniformity of plating thickness, the stainless steel test shaft was provided with grinding centers; four reference sections were ground to less than 10 micro-inch runout. One of the reference sections was silver-plated and the shaft remounted in the grinder (Figure 28) with the object of regrinding the plated section to 0.010 inch thickness with a uniformity of 25 micro-inches. Even the simple act of remounting the plate shaft on the identical shaft centers, however, tends to vary the apparent runout owing to slight shifts in the axis of rotation. By adjusting the center position, the original reference surfaces were held to within 16 micro-inches runout after grinding the silver-plated section.

Visicorder traces were made of the "true" and "apparent" runout of the test shaft when mounted in the precision grinder. Probes are located adjacent to one another in the fixture shown in Figure 26. True runout is measured by the Electrojet contacting probe; apparent runout is measured by the calibrated Bently probe.

Figure 29 compares the true and apparent runout when the Bently gage is sensing the unplated stainless steel shaft. It will be seen that the apparent runout is nearly 10 times the true value. Figure 30 shows the improvement attained when the shaft segment sensed by the Bently probe was silver plated and reground to 0.010 inch uniform overlay. The apparent runout was substantially reduced; a difference of about 60 micro-inches exists between the true and apparent values.

Different silver plating thicknesses were evaluated on the stainless steel test shaft; the uniformity of plating thickness was maintained by grinding, using the reference sections on the shaft to insure a uniform grinding reduction. These tests have indicated that a plating thickness of about 0.005 inch (Appendix C) is about optimum; a maximum shift in the calibration curve of only 40 micro-inches occurs, as shown in Figure 31. This represents less than 1% of the diametral clearance of the bearings to be investigated.

In addition to the static or slow speed gage evaluation tests previously described, a series of tests were carried out to see whether speed itself adversely affected the Bently probe signal. To accomplish this, a capacitance gage was employed as a standard of comparison. Capacitance gages are not affected by rotational speed (Reference 17). A short shaft segment of type 420 S.S. (from the same batch as the test shaft) was attached to a variable speed spindle. Photographs were taken of the simultaneous Bently and capacitance gage probe signal against a time base. These photographs are shown in Figures 32 and 33.

Again, the presence of shaft flaws produces sharp spikes on the Bently gage traces, which are evident on the slower speed traces. At higher speeds, the spikes do not show up, presumably because of insufficient intensity on the oscilloscope beam. The shaft flaws (or spikes) do not coincide with the test shaft

minimum and maximum runout positions. Hence, the amplitude of shaft runout measured by the two different probes is a good agreement over a speed range between 2600 and 26,000 rpm. This information is presented in Figure 34.

Force-Gage Evaluation

As was discussed in the previous section on dynamic analysis, simultaneous measurement of dynamic force and shaft displacement permits the bearing spring and damping coefficients to be established. The system for force-measurements has also been previously described. To evaluate the adequacy of the force measuring system, a special test fixture has been designed. This device is shown in Figure 35.

A short drive shaft is supported on rolling element bearings which are mounted in a cylindrical housing. The housing in turn is supported on 8 strain gage transducers in an arrangement similar to that which will be used in the water-lubricated bearing test rig.

Dynamic forces will be imposed on the shaft by unbalance weights on the symmetrical disks attached to the rotating shaft. Thus, known unbalance forces will be imposed, which can be verified before actual installation in the test device.

One of the design objectives for the test device is to minimize shaft deflection at the unbalance disks. The unbalance

then will not be speed dependent. A second objective is to minimize radial restraint provided by the drive. These objectives are not by the design shown, in which the unbalance disks are located adjacent to the precision support bearings and the assembly driven through a small diameter, flexible drive attached at the center of the hollow bearing shaft. Overhang weights and shaft couplings are therefore eliminated.

It is planned to rotate the test shaft at speeds up to 7500 rpm to create dynamic load of 100 lbs. with a total unbalance of 63.6 gram-inches. For the force-measuring system, a sensitivity of about one pound without excessive signal amplification is desired. This should be accomplished while maintaining a bearing housing support stiffness in excess of 100,000 lbs/inch.

Strain gage transducers have been fabricated, assembled and calibrated to accomplish the force measurements (Reference Figure 9). Each transducer contains four strain elements attached to the underside of the plate section in a complete bridge arrangement. Increased sensitivity and temperature compensation are thereby attained. The gages are protected from moisture by an epoxy coating, which also serves to anchor the lead wires.

To determine the proper plate thickness of the transducer for the desired sensitivity and stiffness, the plate thickness

of one transducer was machined to different values. Calibration data for this transducer is shown in Figure 36. From this information, a plate thickness of 0.05 inch appears to produce adequate sensitivity for the force measurements.

Loader-Bearing Friction Torque

A test rig has been designed to permit measurement of loader bearing friction torque. This is shown in Figure 37. Two opposed partial arc loader bearings bear against a variable speed shaft projecting from a spindle. The partial arc bearings are attached to a box-like structure which in turn is supported at its upper end by low friction rolling element bearings. The opposed loader bearing arrangement produces a net zero load on the rotating shaft, minimizing bending effects of the shaft within the bearings. Bearing friction torque is measured by torque arms which restrain the box-housing from rotating. A somewhat similar scheme was used successfully to measure screw-seal friction torque in a different program. The speed range for this test is 3600 to 30,000 rpm and is necessary since the loader bearing pads are identical to those that will be used in the journal bearing test unit. In this manner the measured total torque of the bearing test unit can be broken down and isolated.

REFERENCES

(1) Electrical Power Generator Systems for Space Applications National Aeronautics and Space Administration Report NASA-SP-79, 1965

(2) D.D. Fuller, "Theory and Practice of Lubrication for Engineers: John Wiley and Sons, Incorporated, New York, New York

(3) H. Schlichting, "Boundary Layer Theory" McGraw Hill Book Company, New York, New York, 1960

(4) E. B. Arwas, B. Sternlicht, R. J. Wernick "Analysis of Plain Cylindrical Bearings in Turbulent Regime" ASME Paper No. 63, Lub 11

(5) M.I. Smith and D.D. Fuller, "Journal Bearing Operation at Super-Laminar Speeds" Trans. ASME, Vol, 78, 1956

(6) W. N. Constantinescu, "On Turbulent Lubrication," Proc. I. Mech. E., Vol. 173, 1959

(7) C.W. Ng and C.H.T. Pan, "A Linearized Turbulent Lubrication Theory" ASME paper 64 - Lub 29, presented at the International Lubrication Conference, Washington, D.C. October, 1964.

(8) R. A. Burton, "Turbulent Film Bearings Under Small Displacements" Paper No. 64AM3B1 presented at the 1964 ASLE Annual Meeting, May 26-28, Chicago, Illinois

(9) M.C. Shaw, E.F. Macks, "Analysis and Lubrication of Bearings" McGraw Hill Book Company, Incorporated, New York, New York, 1949

(10) O. Pinkus and B. Sternlicht, "Theory of Hydrodynamic Lubrication" McGraw Hill Book Company, Incorporated, New York, New York, 1949

(11) J. Lund, B. Sternlicht, "Bearing Attenuation" G.E. Report No. 61GL100, 1961, Contract NObs 78930

(12) P.C. Warner, "Static and Dynamic Properties of Partial Journal Bearings", Journal of Basic Engineering, June, 1963, p 247-257

(13) B. Sternlicht, H. Poritsky, E. Arwas
"Dynamic Stability Aspects of Cylindrical Journal Bearings Using Compressible and Incompressible Fluids"
General Electric Company Report, February, 1960
Under Contract Nonr 2844(00)

(14) A.C. Hagg and G.O. Sankey, "Some Dynamic Properties of Oil Film Journal Bearings with Reference to the Unbalance Vibration of Rotors", Journal of Applied Mechanics, Volume 23, Trans. ASME, Volume 78, 1956 pages 302-306

(15) J. D. McHugh, J. W. Lund, "Bearing Attenuation-Experimental Evaluation", General Electric Company Report, August 28, 1961, under Contract NObs 78930

(16) F. K. Orcutt, C. W. Ng, J. H, Vohr and E. B. Arwas
"Lubrication Analysis in the Turbulent Regime"
NASA Report CR-54259, under Contract NASw-1021

(17) K.S. Lion, "Instrumentation in Scientific Research Electric Input Transducers", McGraw Hill Book Company, Incorporated, New York, New York, 1959

(18) "Low Viscosity Bearing Stability Investigation"
National Aeronautics and Space Administration
Report NASA-CR-54039

Table 1

SUMMARY OF BEARING VARIABLE TEST RANGE

Bearing Type	Length / Diameter Ratio	Lube Temp. (°F)	Lube Abs. Viscosity $\frac{lb.sec. \times 10^7}{in^2}$	Nom. Diametral Clearance (in.) ($\times 10^{-3}$)	Speed Range (RPM)	Film Reynolds No. Range	Taylor* No.	Bearing Static Radial Load (Lbs.)	Bearing Deliberate Unbalance Load (Lbs. at 100 cps)
2-Axial Groove	1	90°F 120°F 150°F	1.1 0.82 0.64	2, 3, 5	3,600 to 34,200	216 to 3,713	9 to 222	0 to 77.4	Residual, to 7.4 14.1
2-Axial Groove	$1\frac{1}{2}$	75°F 120°F	1.4 to 0.82	2 3 5	3,600 to 34,200	190 to 4,000	7.4 to 244	0 to 77.4	Residual to 7.4
Tilting Pad (4-Pads)	1	120°F	0.82	3.2 4.3 6	3,600 to 21,000	388 to 5,500	18 to 400	0 to 77.4	Residual
3-Lobe	1	120°F	0.82	1 mil nom.	3,600 to 21,000	78 to 756	3.2 to 20	0 to 51.6	Residual
Compound Cylindrical	1	120°F	0.82	3 mils nom.	3,600 to 21,000	408 to 2,530	20 to 126	0 to 34.4	Residual
Displaced Elliptical	1	120°F	0.82	3 mils 5.4	3,600 to 23,500	414 to 4,580	20 to 310	0 to 51.6	Residual to 7.4

* Based on minimum nominal clearance for bearing type.

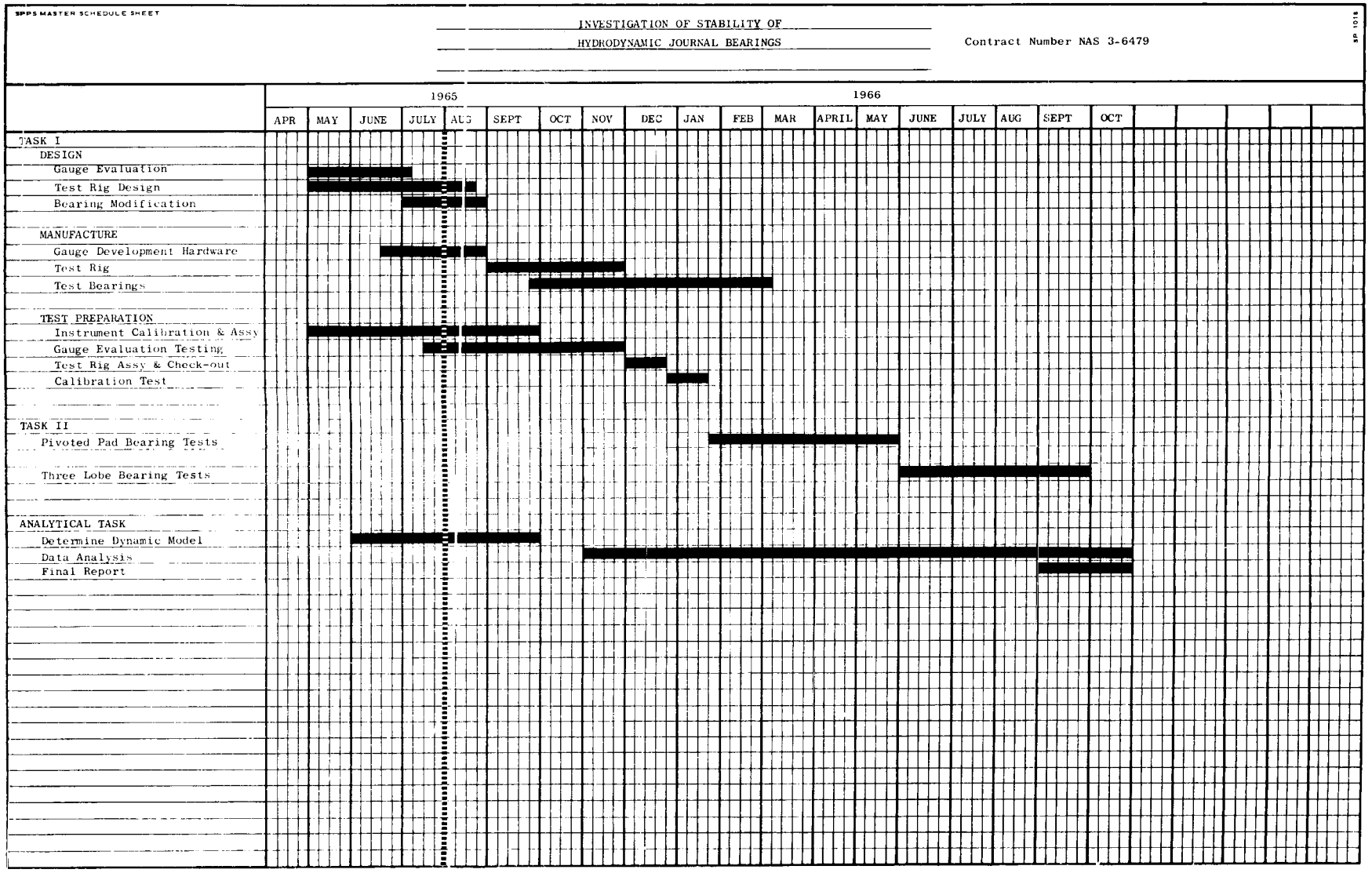

Figure 1. Program Schedule.

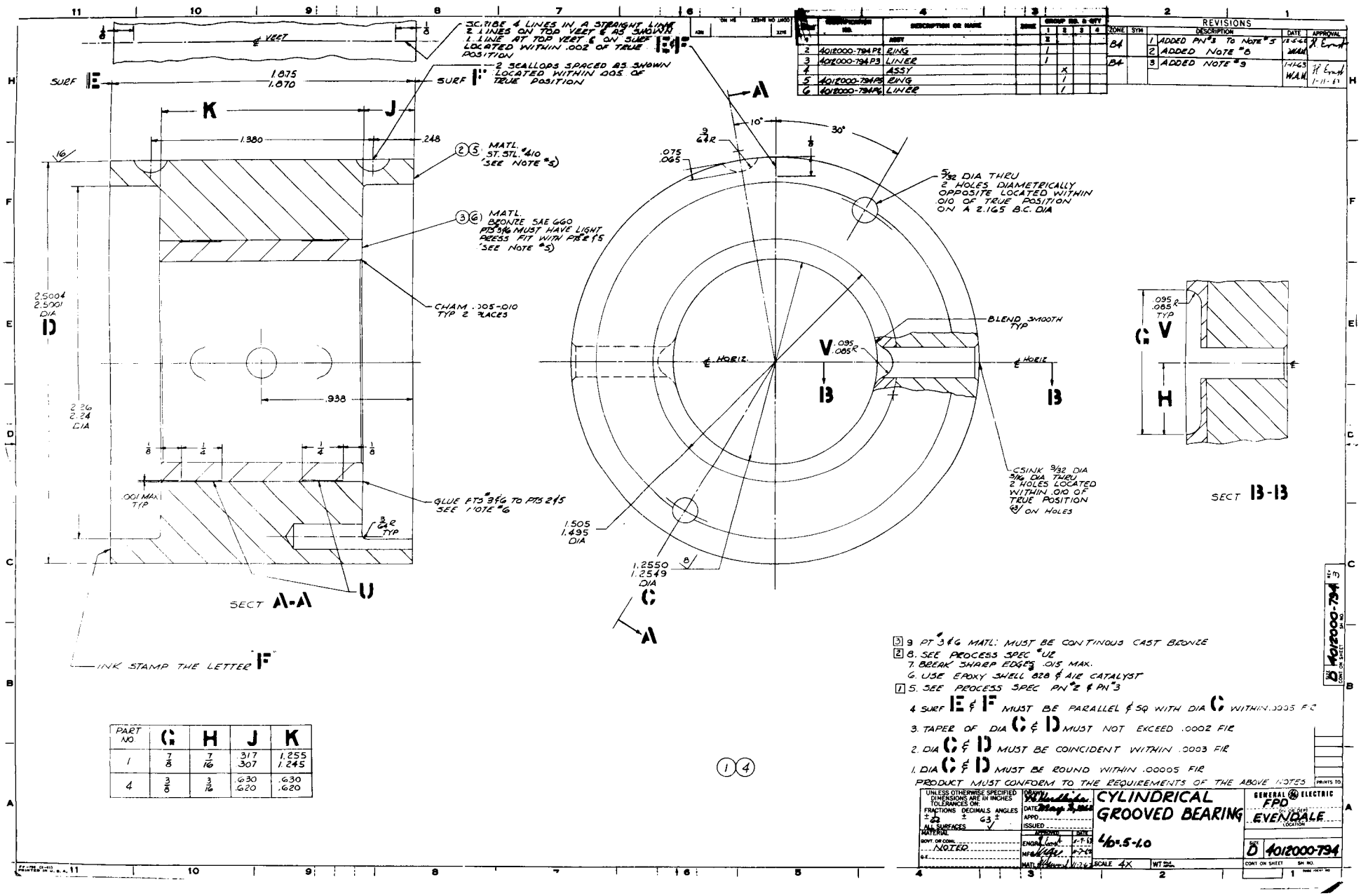

PART NO	G	H	J	K
1	7/8	7/16	.317 .307	1.255 1.245
4	3/8	3/16	.630 .620	.630 .620

Figure 2. Two-Axial-Groove Cylindrical Bearing
L/D = .5 -1.0

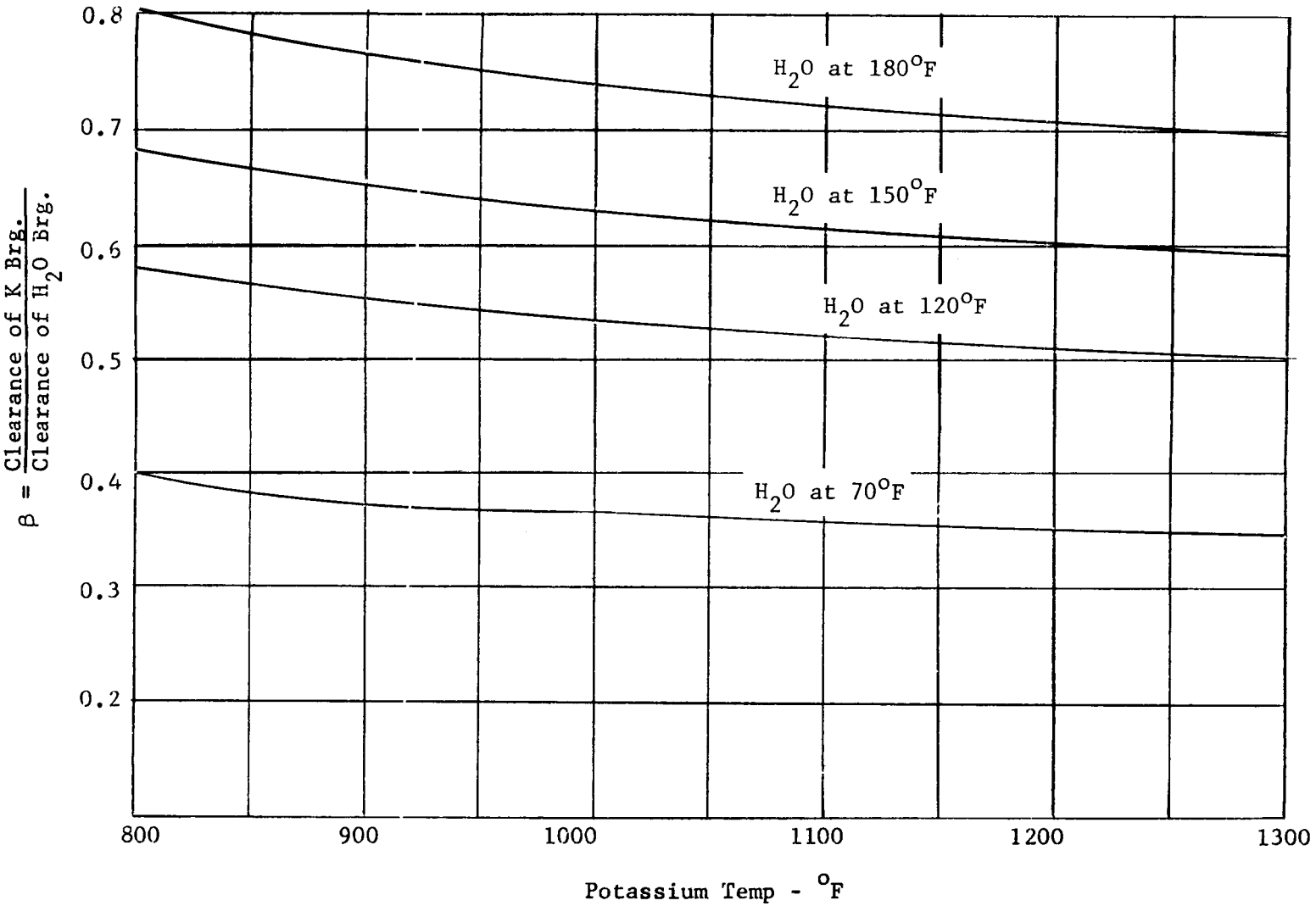

Figure 3. Clearance Ratio Between Potassium and Water Lubricated Bearings for Equal Taylor Numbers.

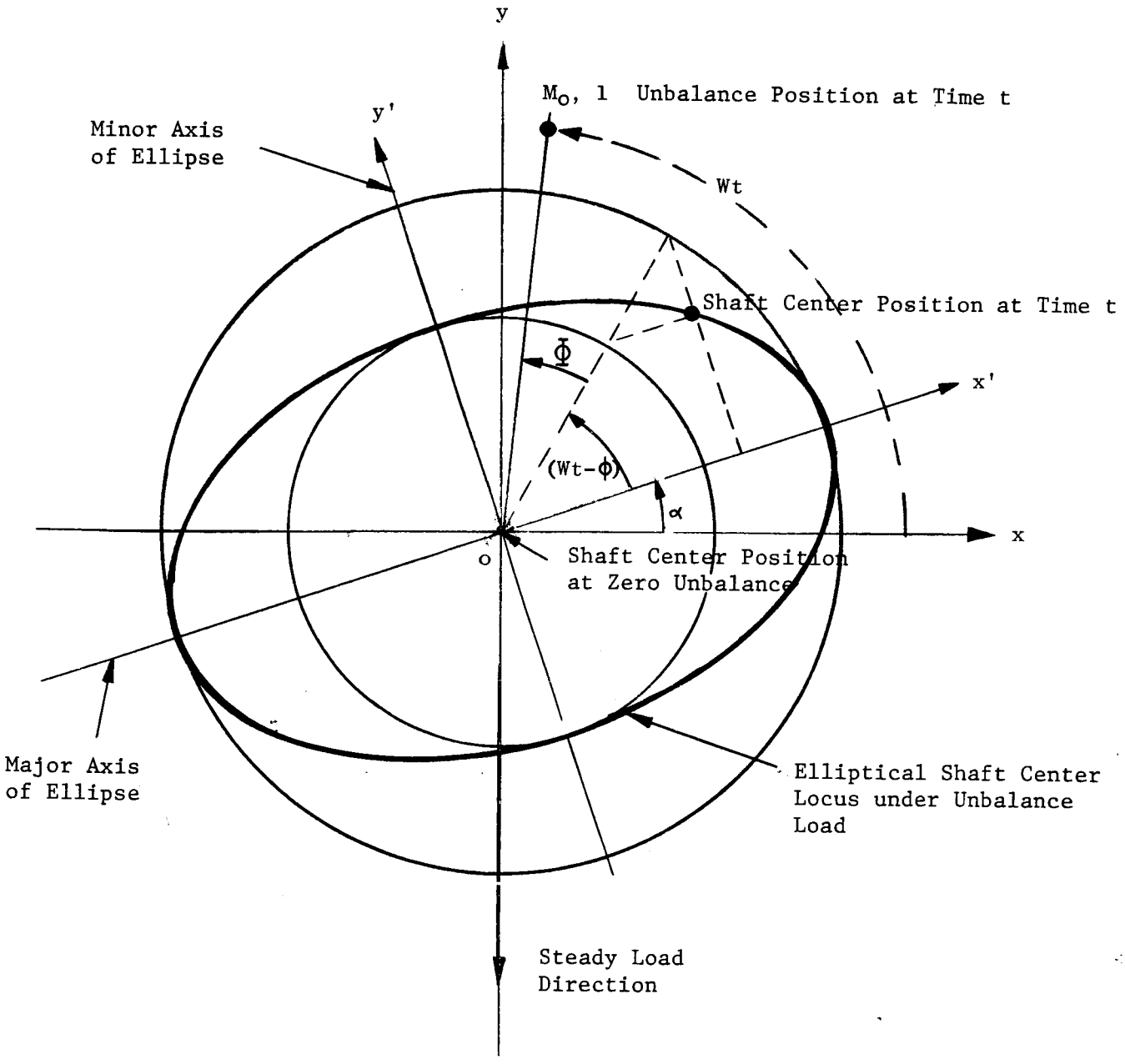

Figure 4. Elliptical Path

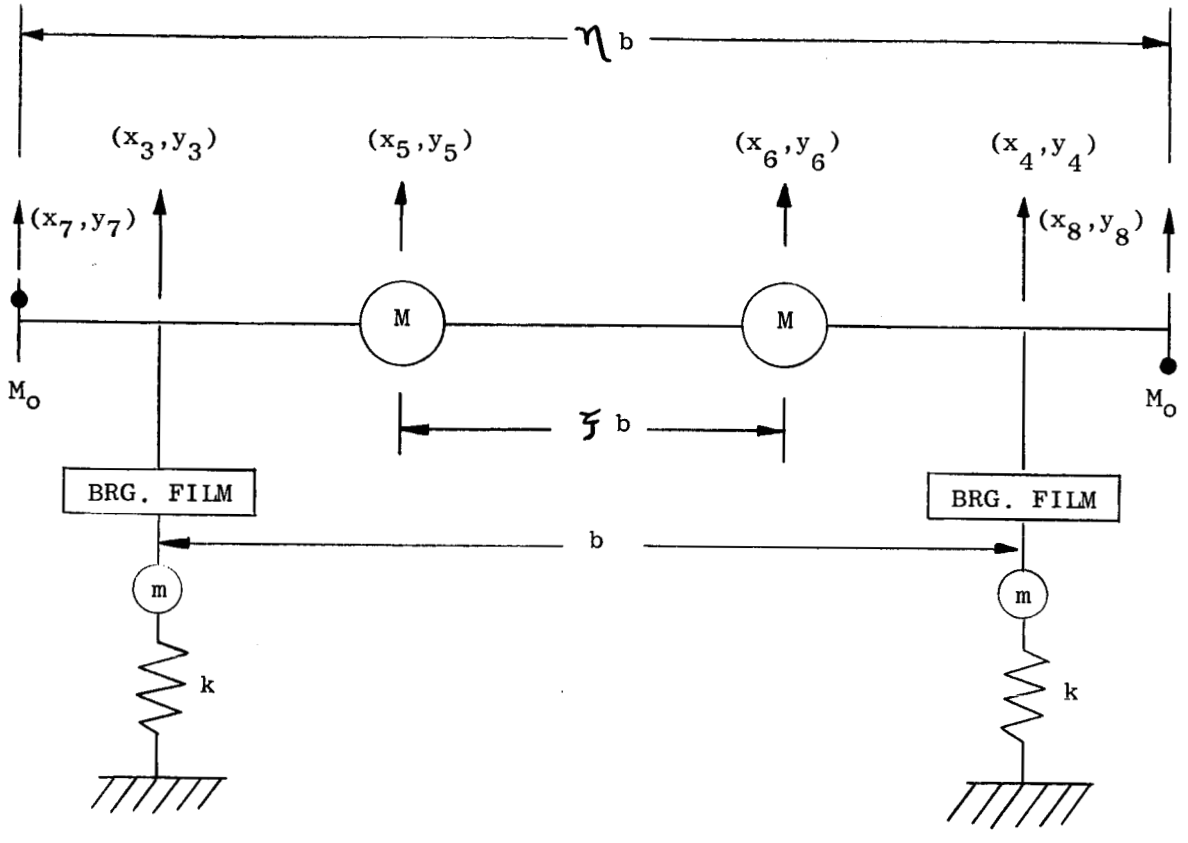

Figure 5. Rotor - Bearing - Pedestal System.

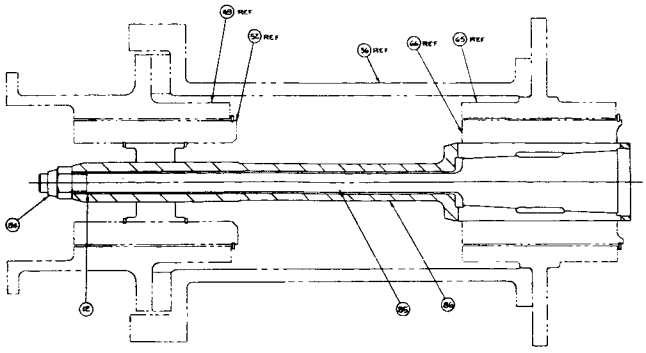

SHAFT ALIGNMENT
ASSY 41 (REF AE5)

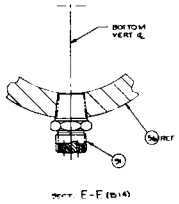

SECT E-E (5:1)

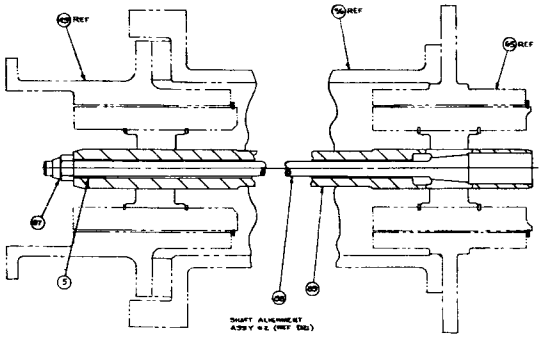

SHAFT ALIGNMENT
ASSY 42 (REF DB2)

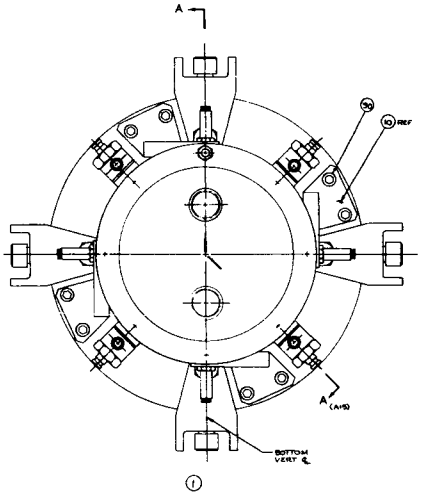

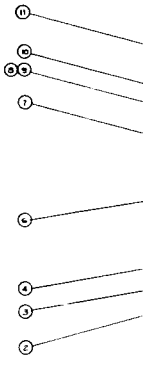

510

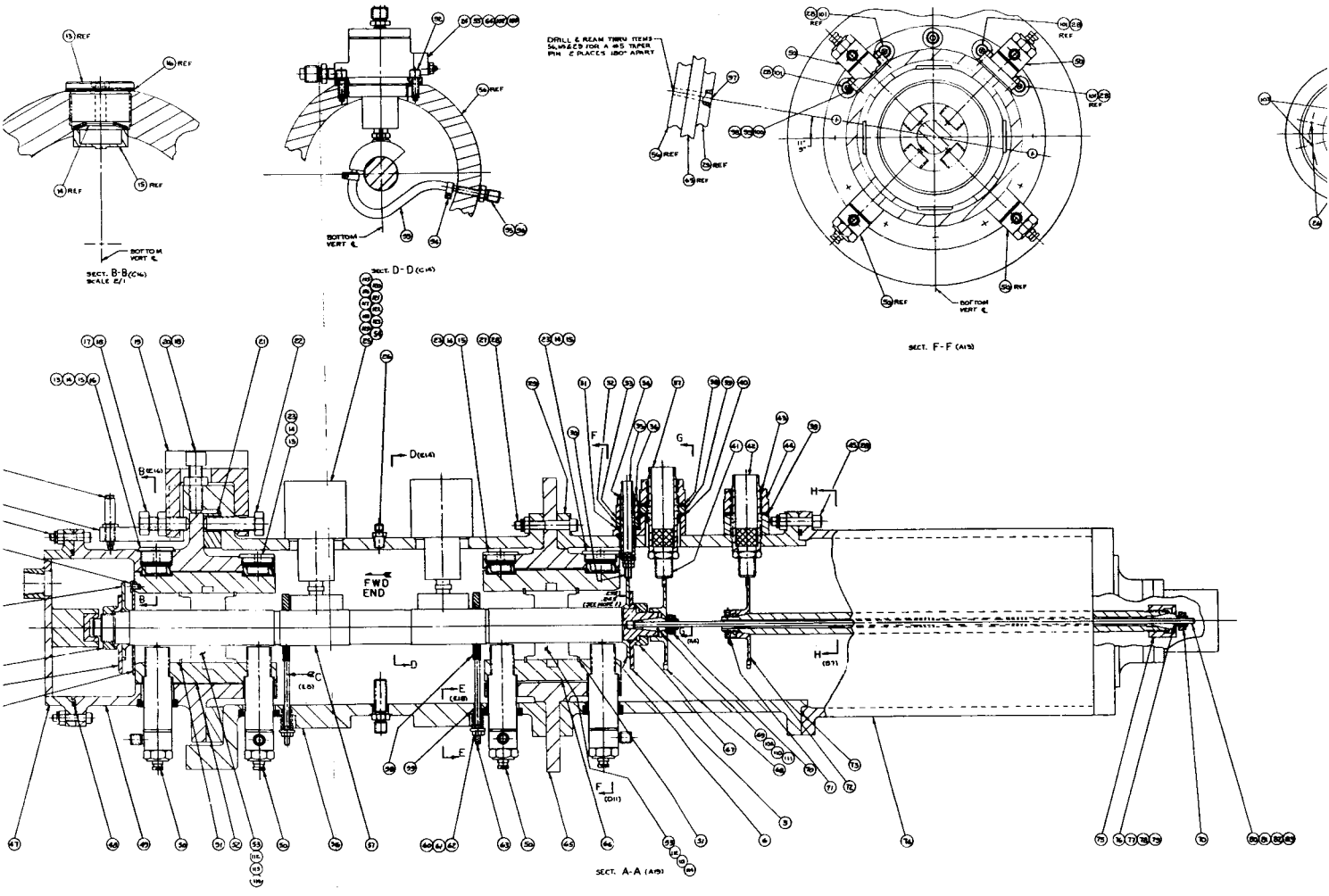
SECT. B-B (C14)
SCALE 6/1
SECT. D-D (C14)
DRILL & REAM THESE ITEMS
SLAVED FOR A #5 TAPER
PIN 6 PLACES 180° APART
SECT. F-F (A13)
FWD END
SECT. A-A (A13)

5/12

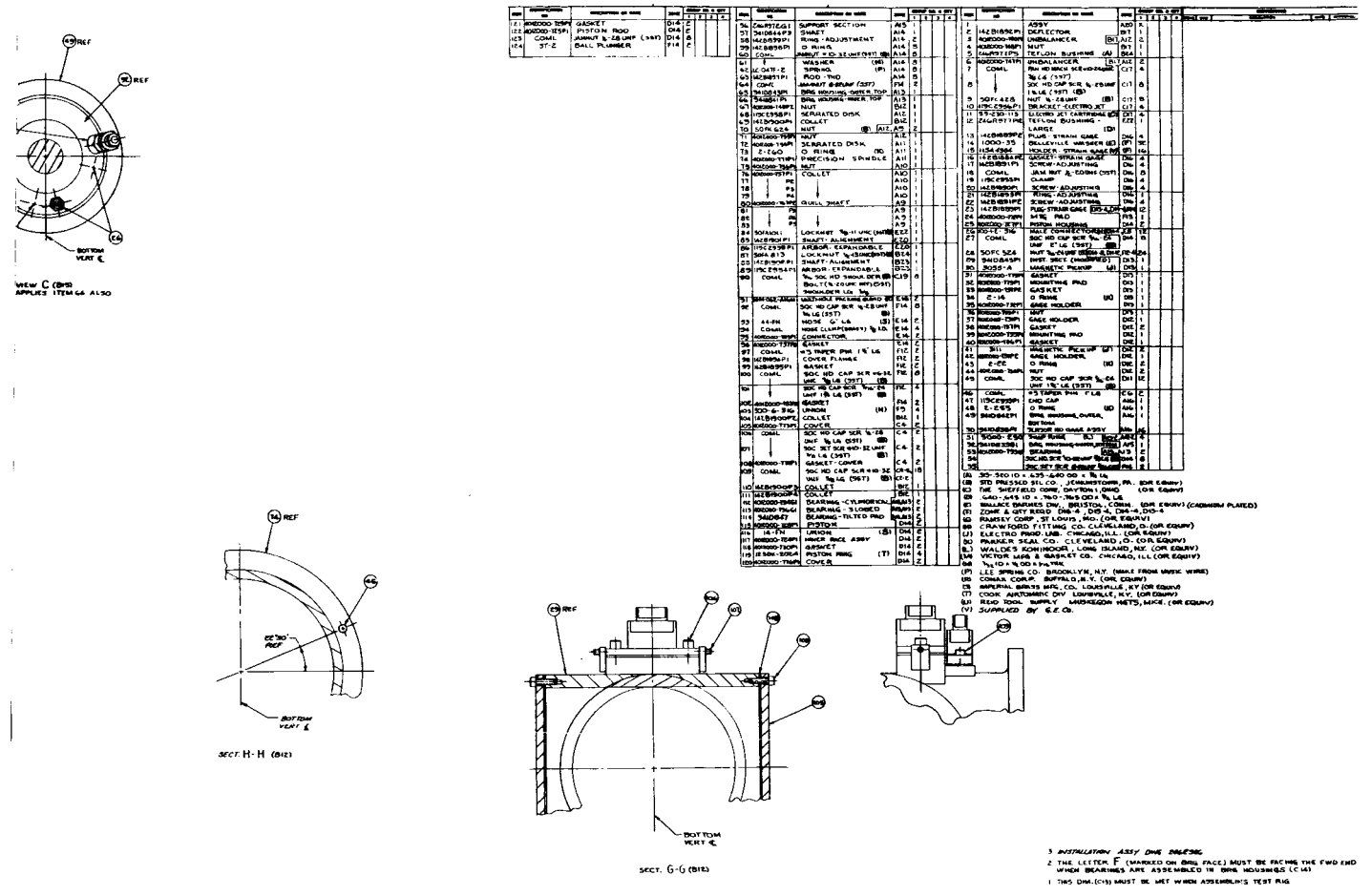

Figure 6. Test Rig Assembly Drawing.

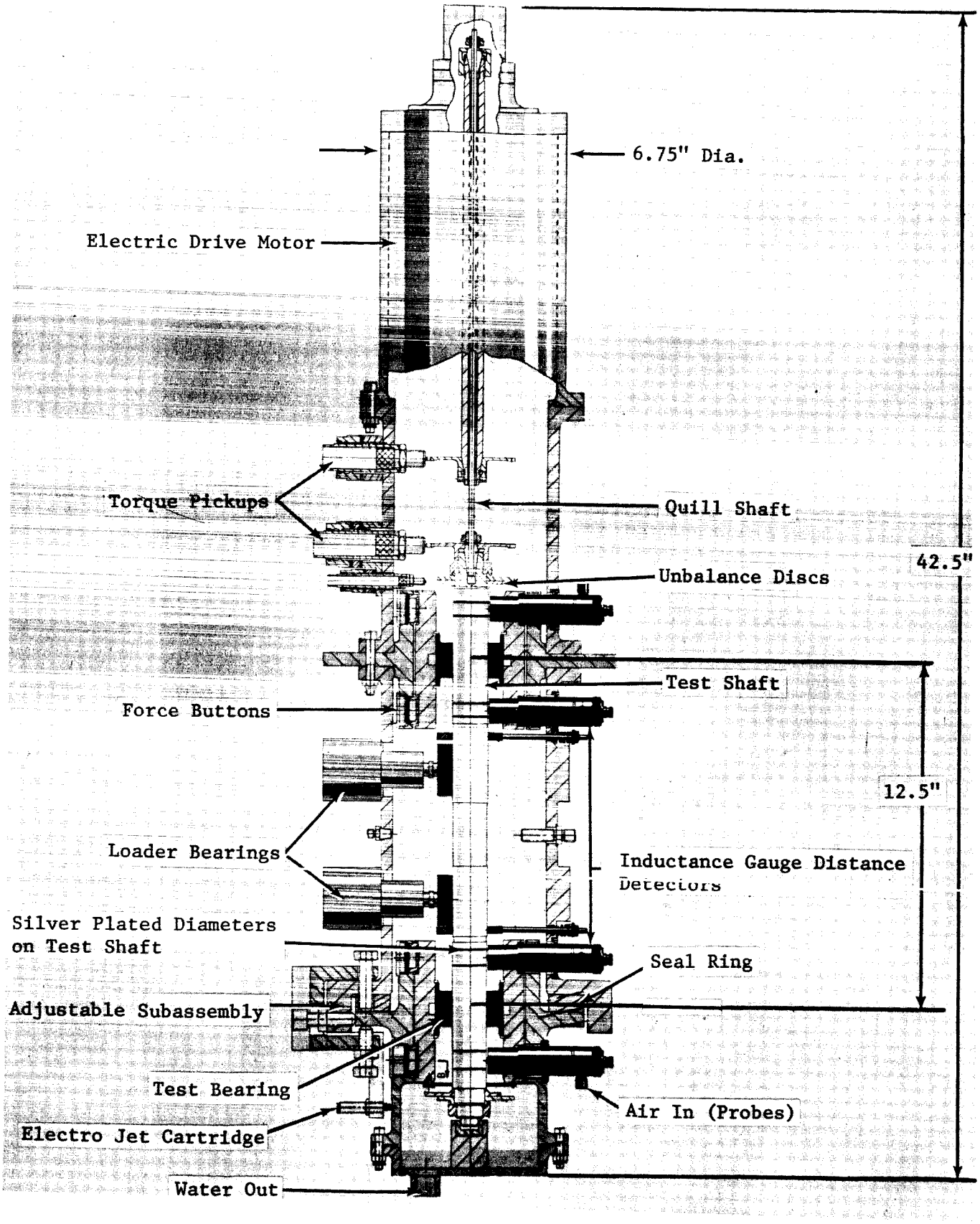

Figure 7. Bearing Stability Test Rig.

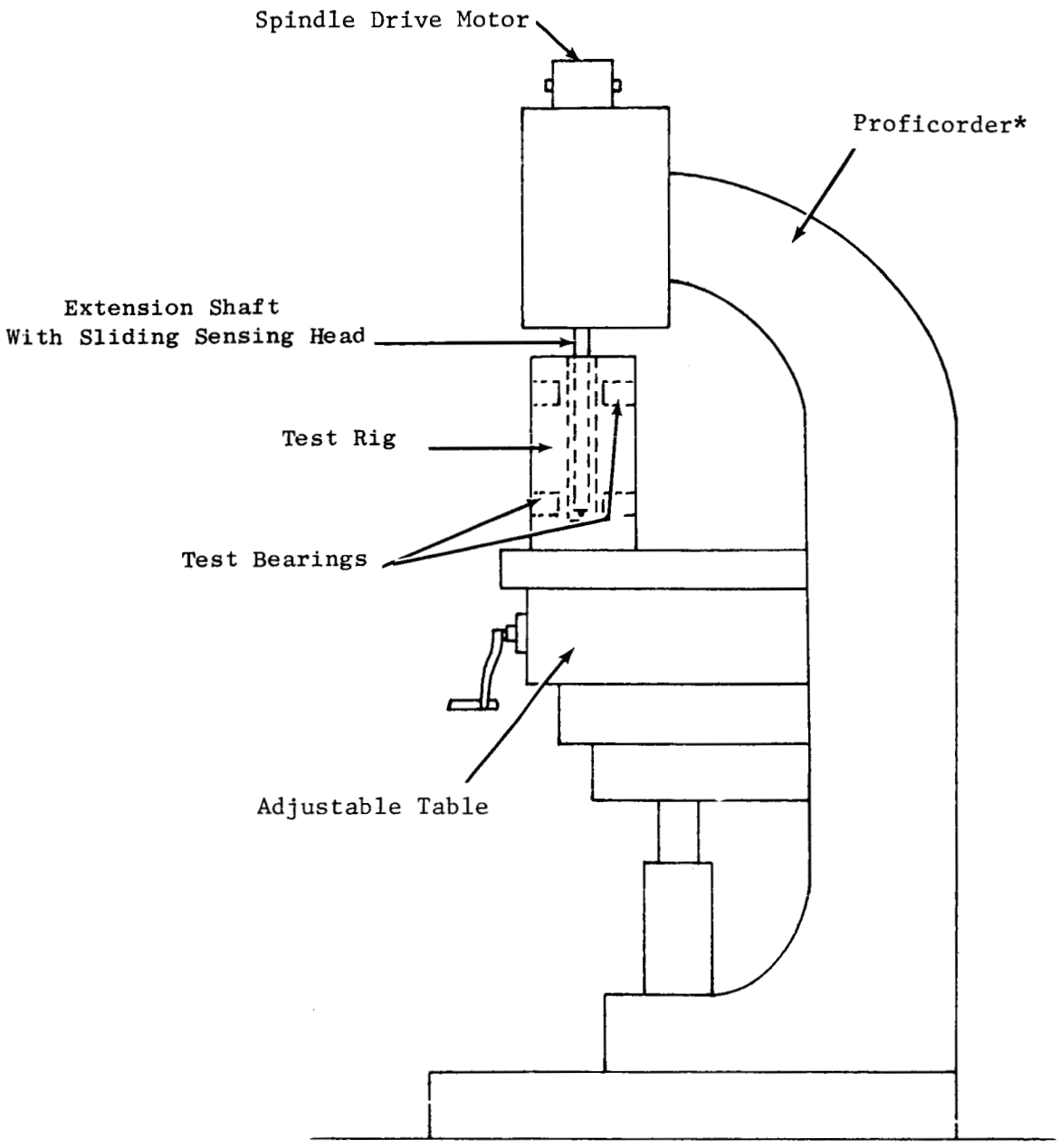

Figure 8. Alignment Scheme Using Proficorder.

*Manufacturer - Micrometrical Corporation
Model - RLF Rotary Pilotor
Overall Dimensions - 24" Wide x 35" Deep x 72½" High

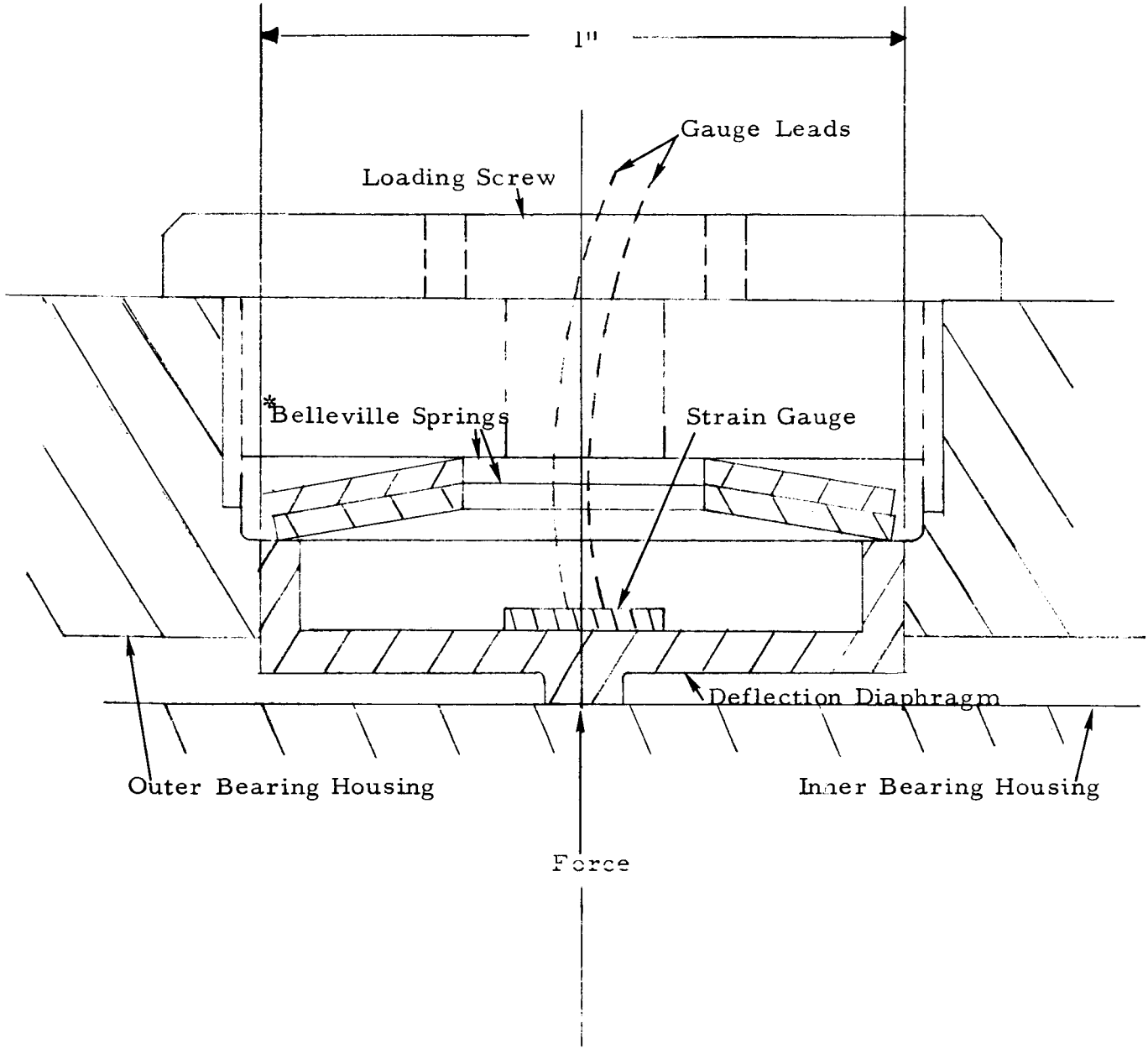

Figure 9. Force Gauge Detail.

*Material - SAE 1075 Spring Steel with Cadmium Plate.
Model #1000-35 (Wallace Barnes Division)

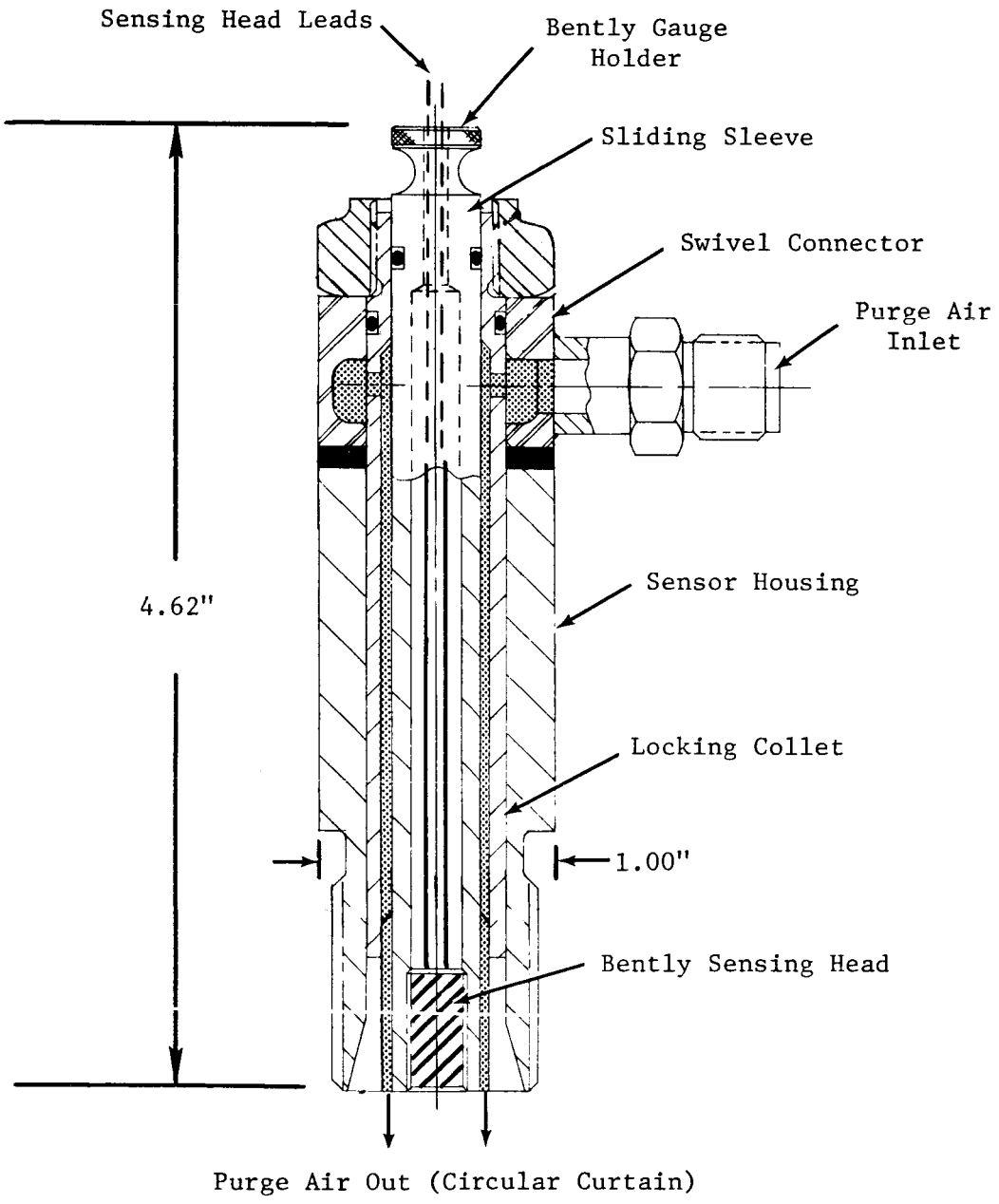

Figure 10. Bently Gauge Holder Assembly.

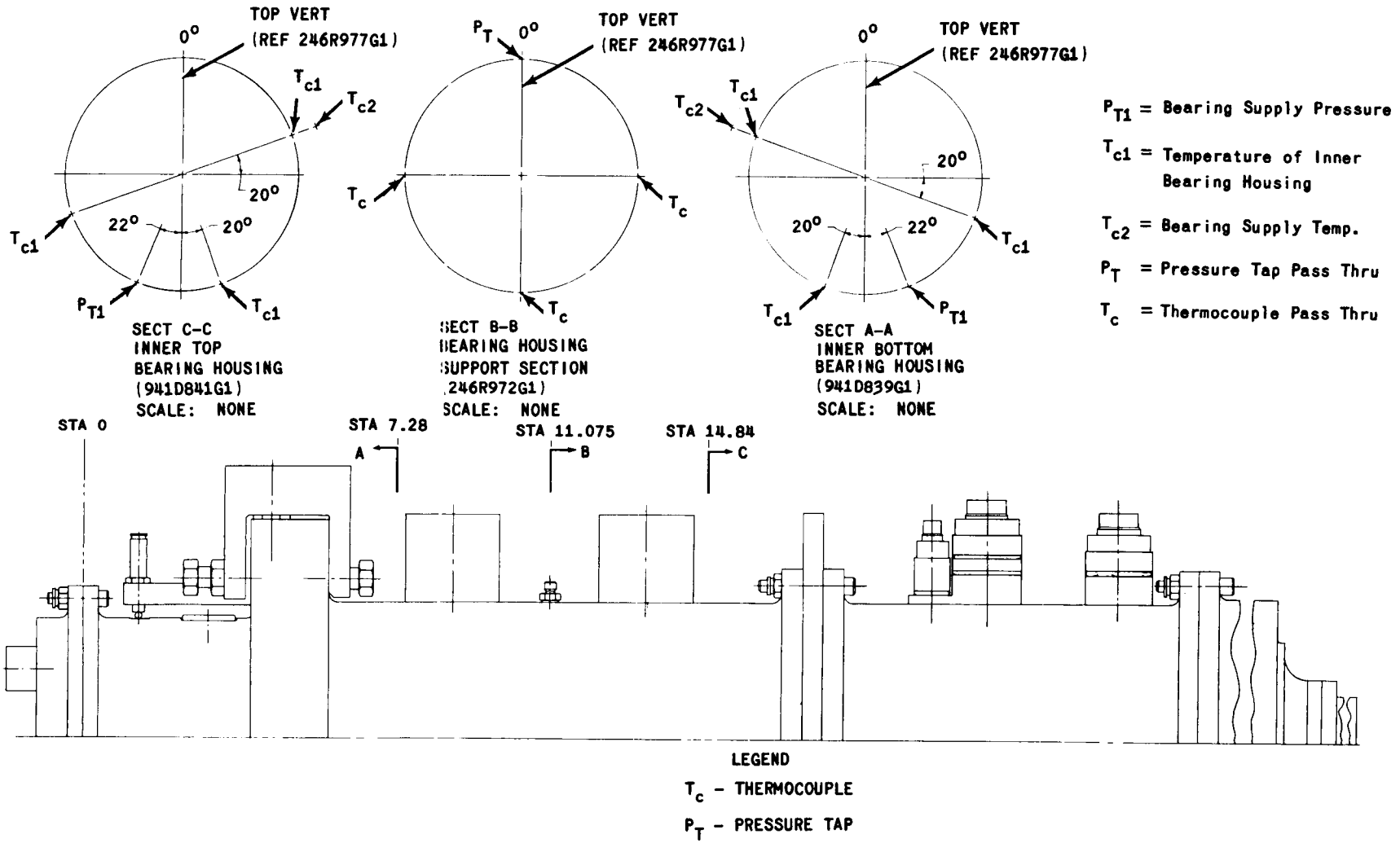

Figure 11. Instrumentation Schematic of Journal Bearing Test Rig.

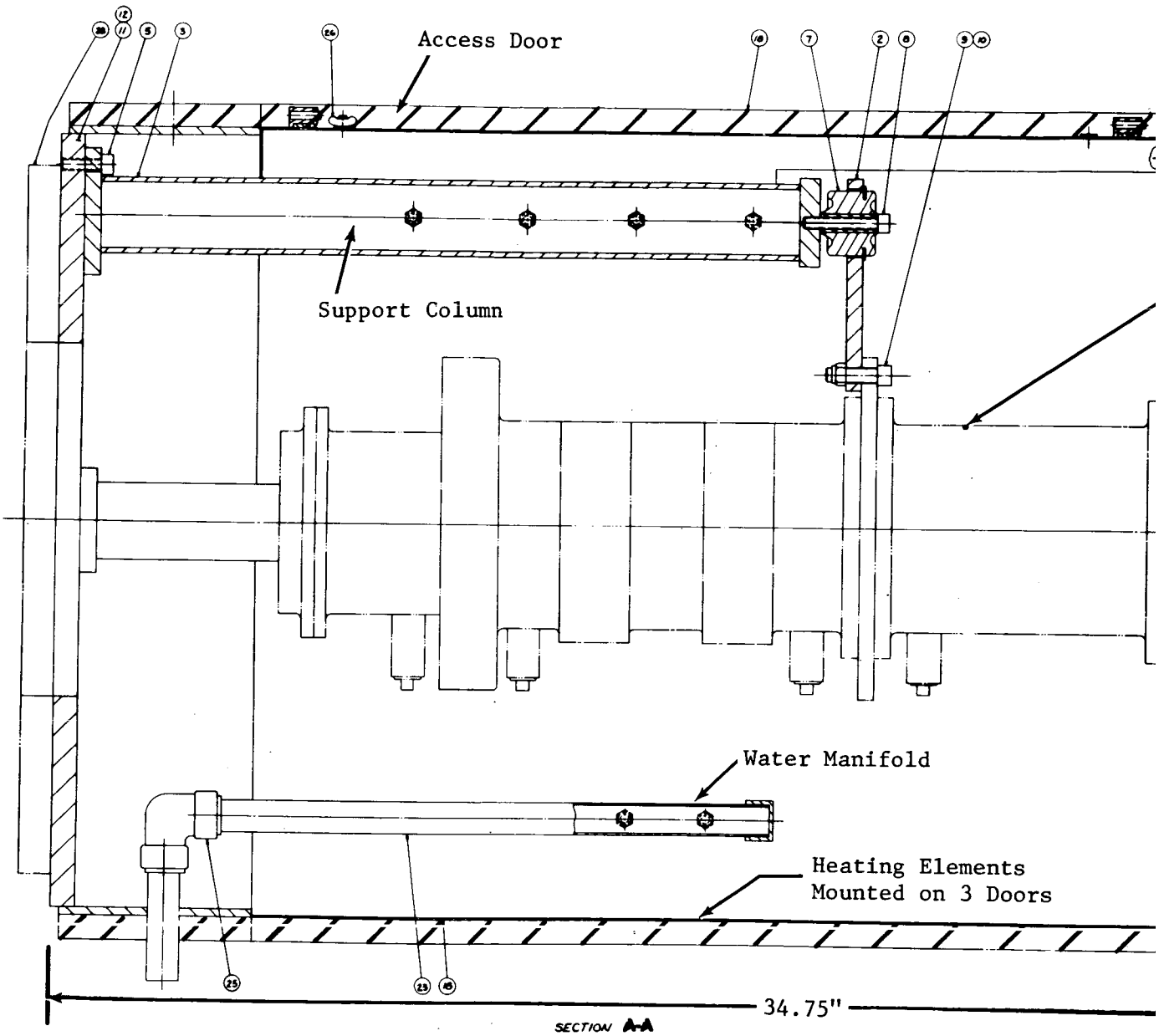
Access Door
Support Column
Water Manifold
Heating Elements
Mounted on 3 Doors
34.75"
SECTION A-A

510

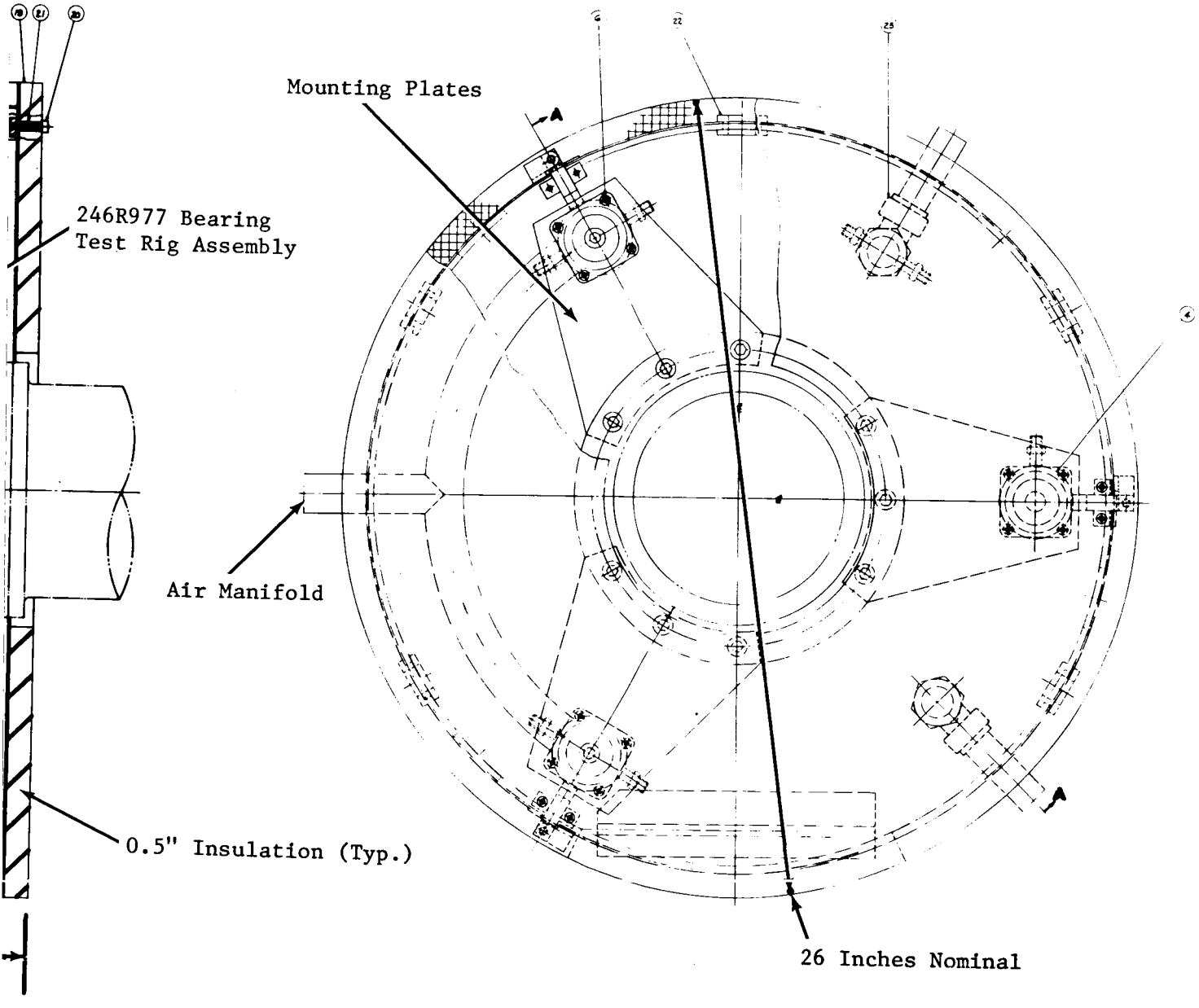
Mounting Plates
246R977 Bearing
Test Rig Assembly
Air Manifold
0.5" Insulation (Typ.)
26 Inches Nominal
A
A

5720

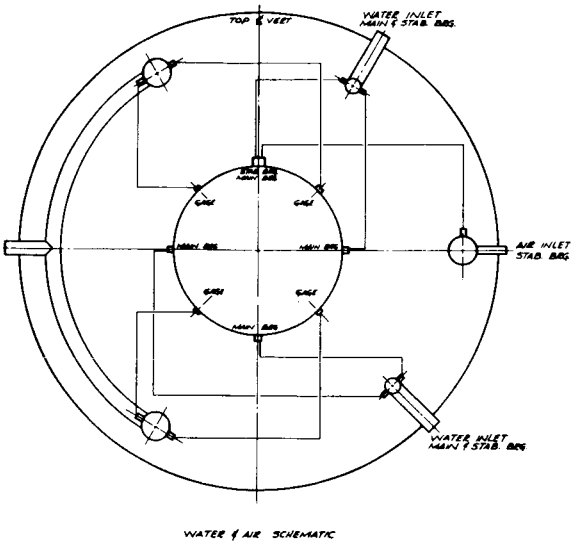

WATER & AIR SCHEMATIC

1							
2	1428/1904	MTG. ARM	CRS	8			
3	2036798	MTG. COLUMN	AB	8			
4	2697800	MTG. COLUMN	BR	1			
5	COMM	SOC. HD. SCR. ⅜-16UNC1 1½ LG.	AB	16			
6	COMM	SOC. HD. SCR. TO BRAND ⅜-16	GU	12			
D 7	2001KP-30	PLATE, MOUNT, MTG.	GRA	3			
8	COMM	SOC. HD. SCR. ⅜-16UNC 2¼ LG	GAE	3			
9	COMM	SOC. HD. SCR. ⅜-16UNC 1¼ LG	GA	3			
10	COMM	LOCKNUT ⅜-16UNC	GA	9			
11	2655T34	BASE	CA	1			
12	COMM	SOC. HD. SCR. ¼-20UNC 2LG	GBB	2			
13	1428/1941	HINGE SUPPORT	AT	1			
14	1428/1942R	HINGE SUPPORT	BA	1			
E 15	1576784	HINGE	AB	1			
16	COMM	SOC. HD. SCR. ⅜-16UNC2 ¾ LG	AB	6			
17	COMM	SOC. HD. SCR. ⅜-16UNC2 ¾ LG	AB	12			
18	2636801	DOOR COVER	AB	8			
19	1428/1908	TOP COVER	BM	2			
20	COMM	SOC. HD. SCR. ¼-20UNC2 1 LG	GM	16			
F 21	COMM	SPACER	BM	3			
G 24	4270	GASKET	GU	3			
25	1428/1955	WATER MANIFOLD	GB	2			
26	941/0859	AIR MANIFOLD	AT	1			
H 27	1600-3-316	ELBOW	AM	2			
28	COMM	MACHINE ¼-20	GB	16			
29	COMM	LOCKNUT ¼-20UNC2	AB	12			
30		MTG. TABLE	BZ	4M			

D: LORD MFG. CO. ERIE, PA. OR EQUIV.
E: MCMASTER CARR SUPPLY CO. CHICAGO, ILL. OR EQUIV.
F: ¼ I.D. ⅜ O.D. TUBE
G: ATLANTIC INDIA RUBBER WORKS CHICAGO, ILL. OR EQUIV.
H: CRAWFORD FITTING CO. CLEVELAND, OHIO

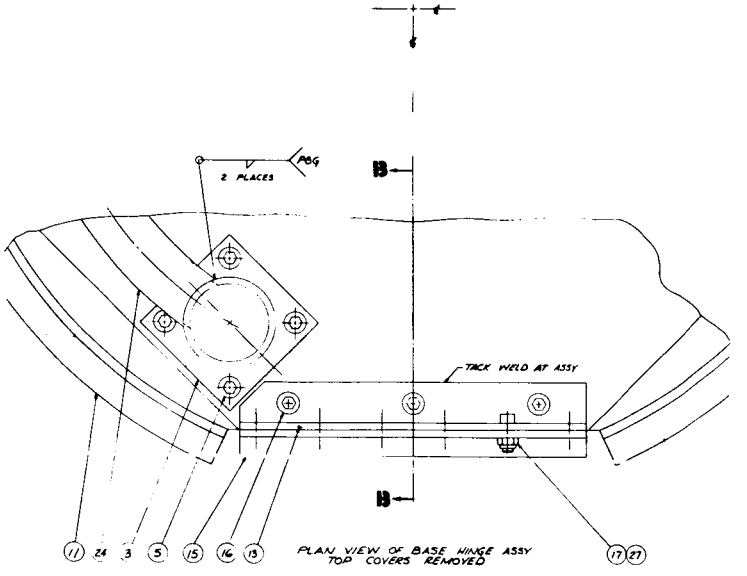

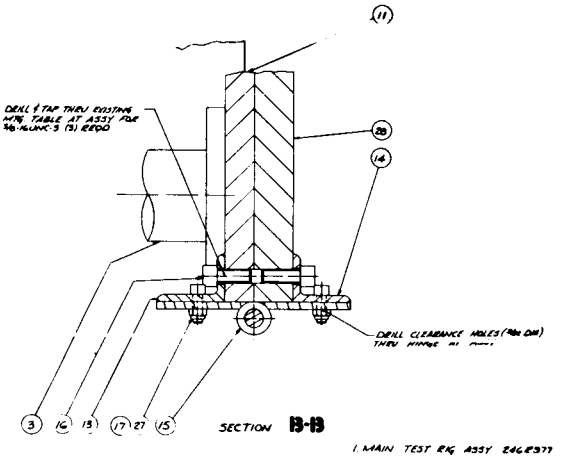

1 MAIN TEST RIG ASSY 246E977

	JOURNAL BRG TEST RIG INSTALLATION ASSY	246R986

Figure 12. Support Structure for Test Rig

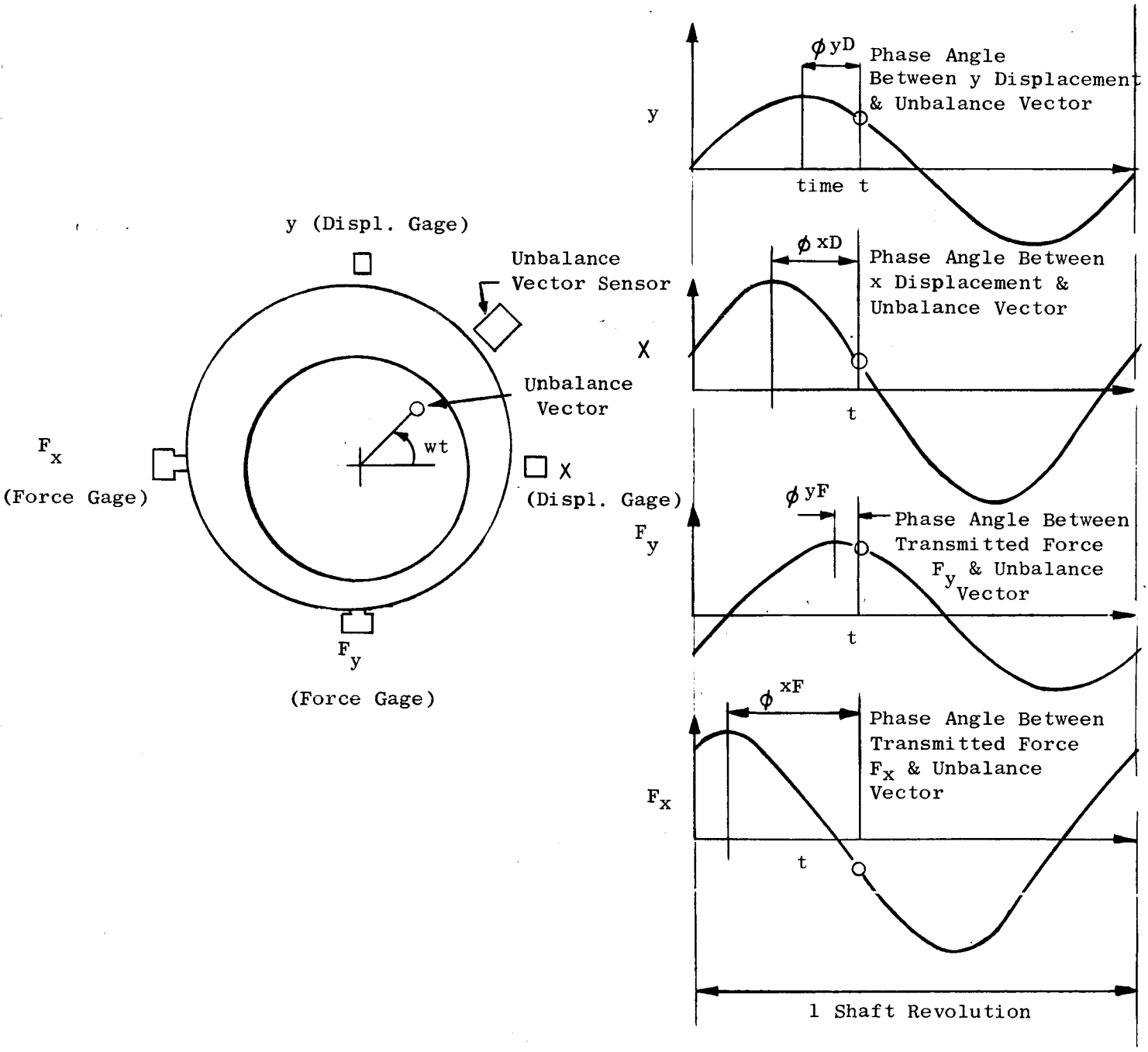

Figure 13. Schematic of Shaft Displacement & Force Gage Instrumentation Requirements.

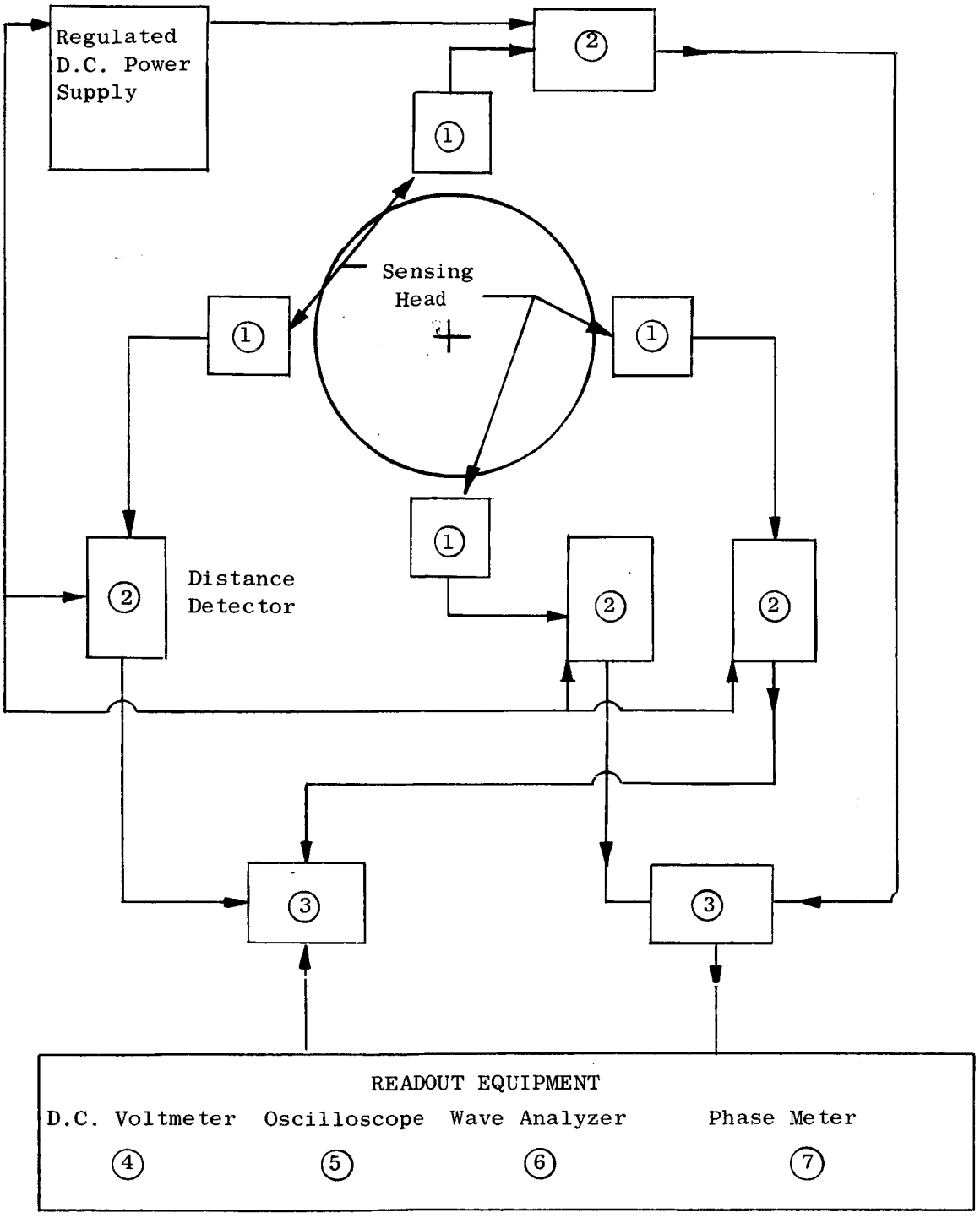

For instrumentation details, see corresponding numbers in Appendix A.

Figure 14. Block Diagram - Shaft Displacement Instrumentation.

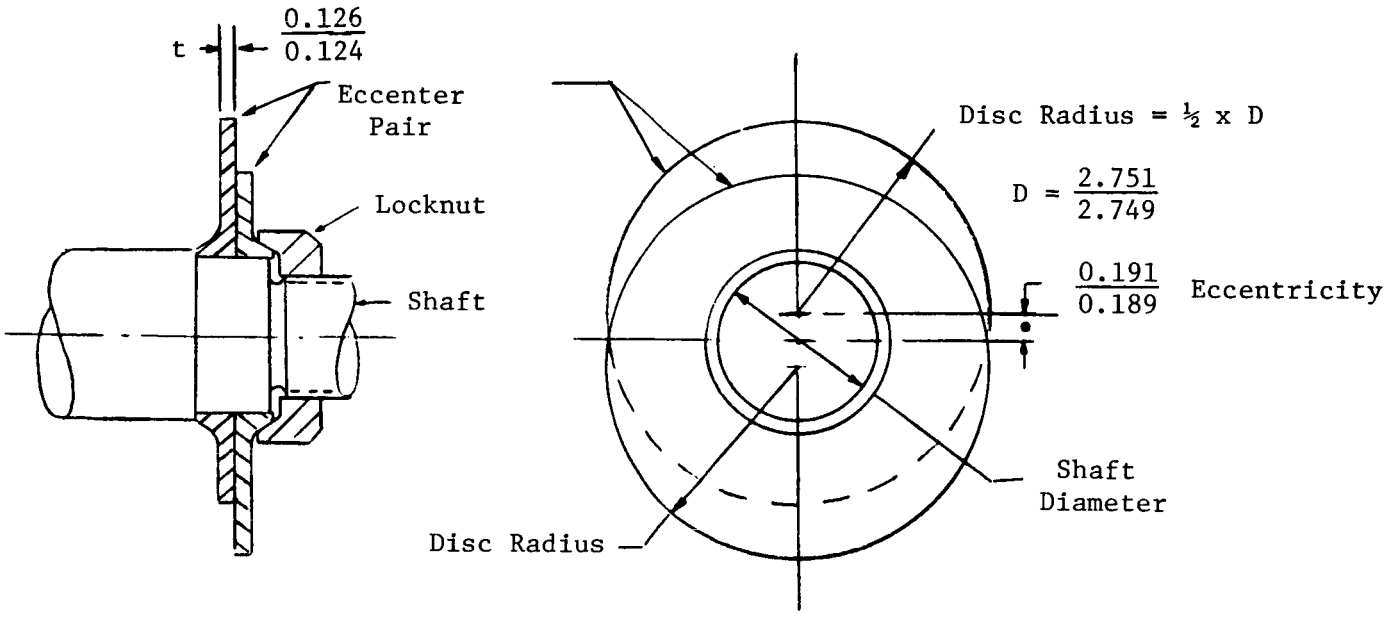

Figure 15. Eccenters for Dynamic Load Application
(Zero Unbalance Shown)

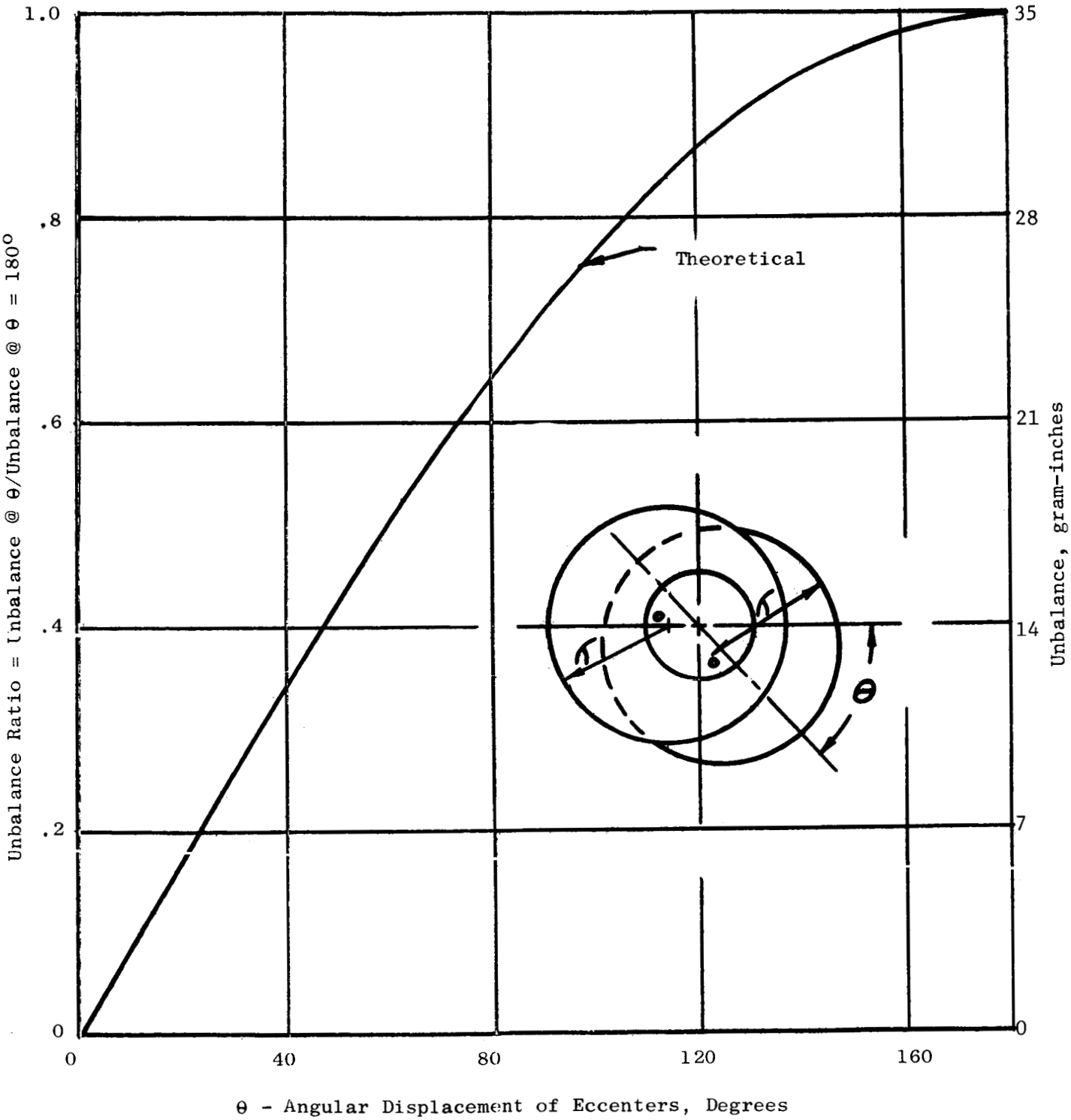

Figure 16. Eccenter Unbalance Ratio at Different Angular Settings.

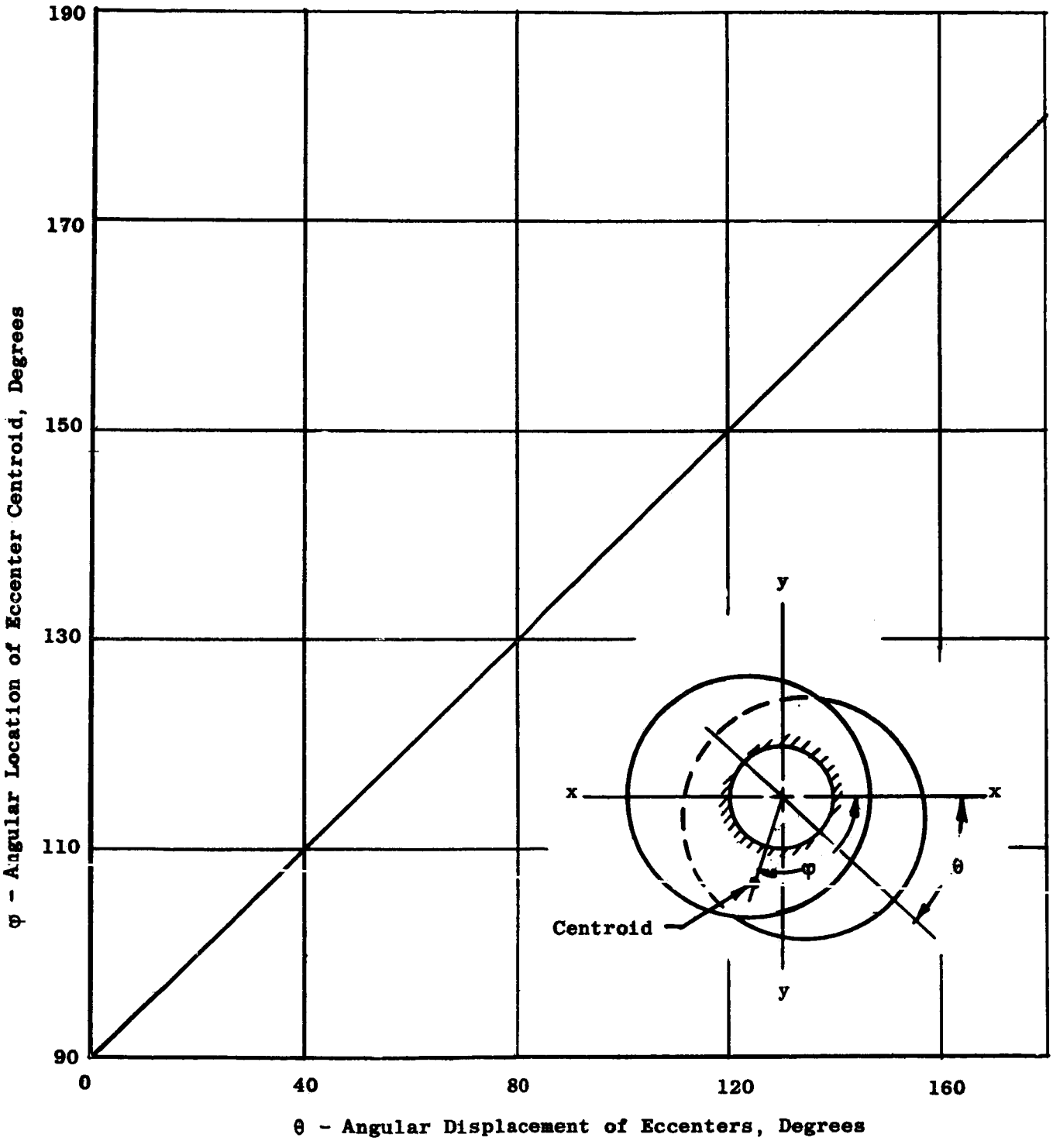

Figure 17. Angular Location of Eccenter Center of Gravity at Different Angular Settings.

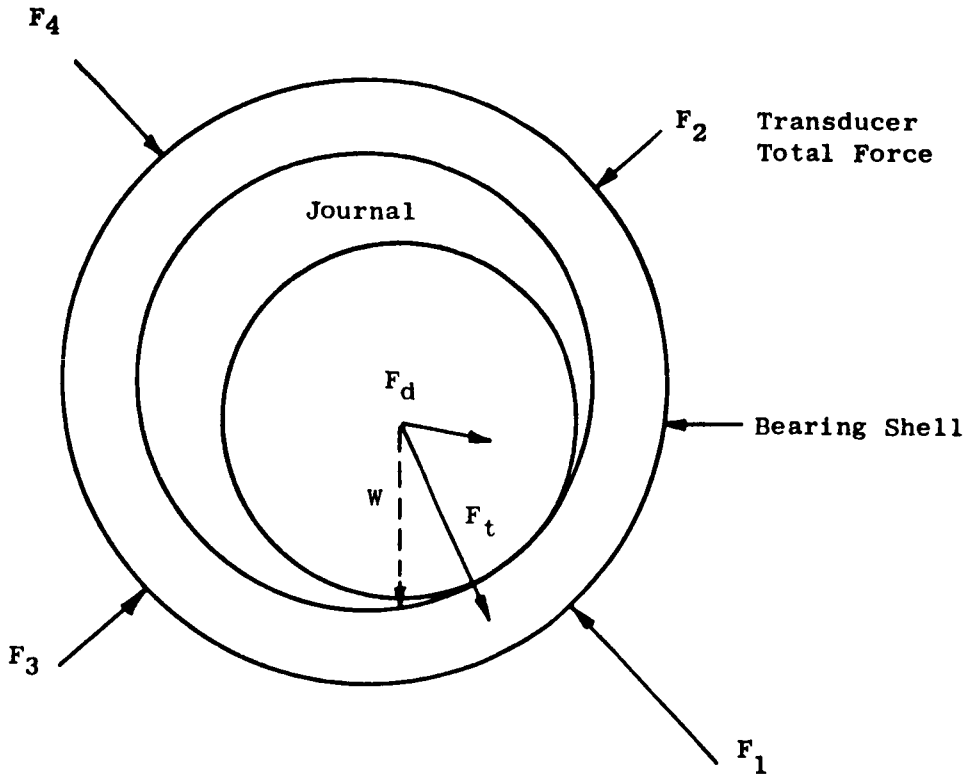

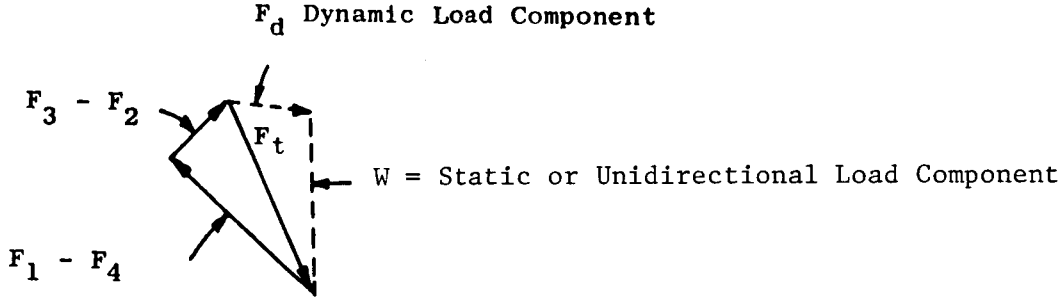

Figure 18. Force Vector Diagram, Dynamic Loading.

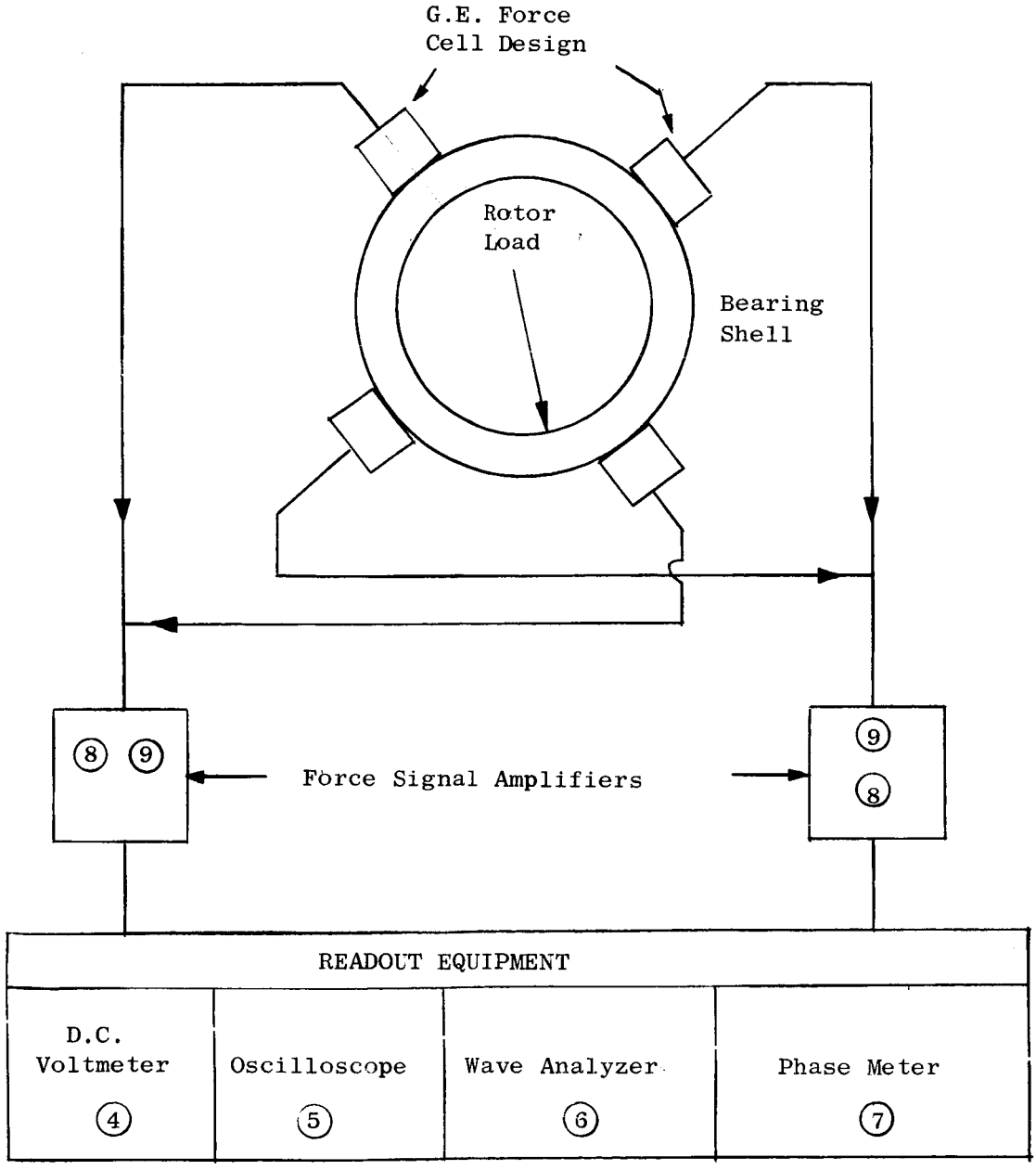

For instrumentation details, see corresponding numbers in Appendix B.

Figure 19. Block Diagram - Rotor Force Instrumentation.

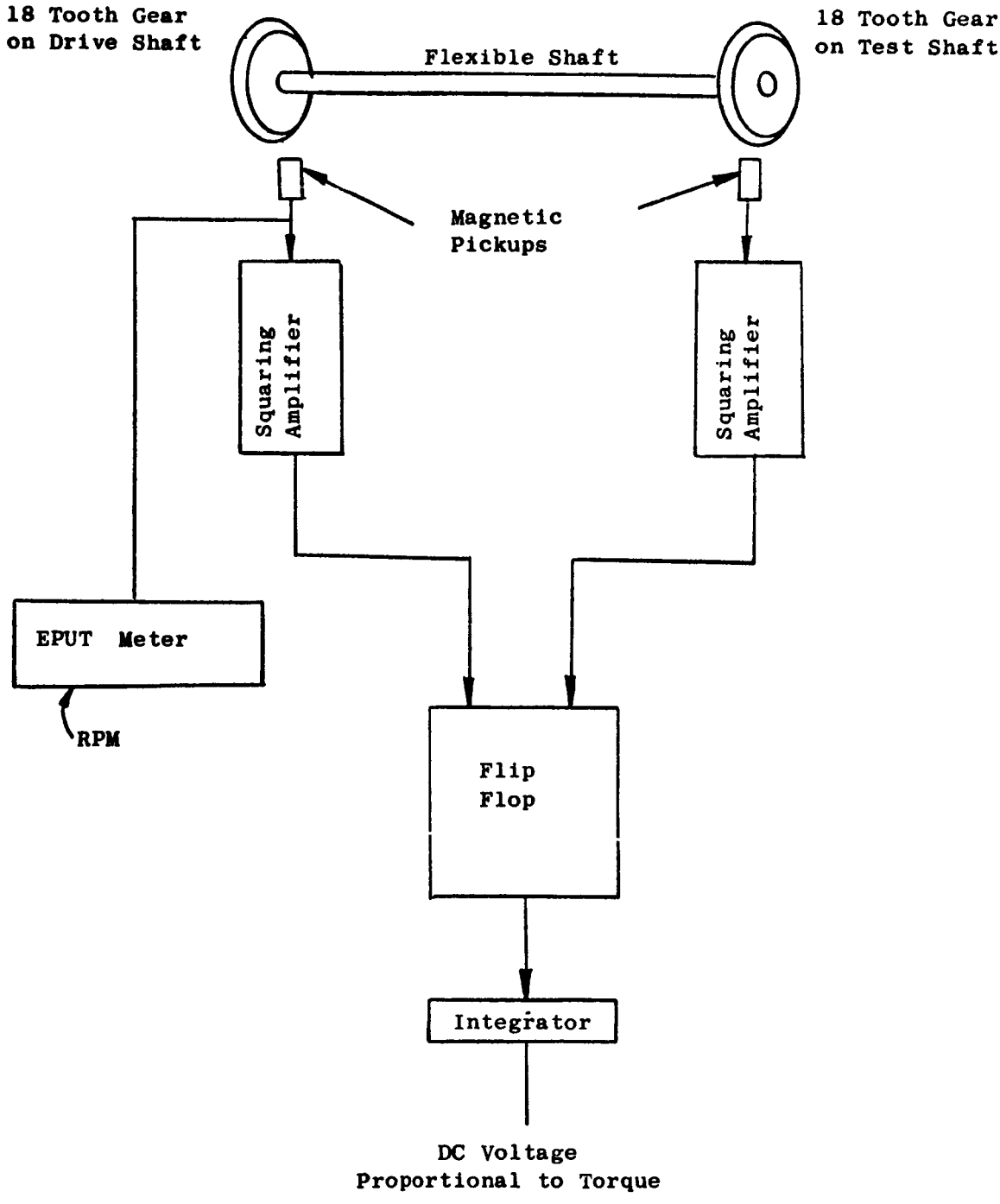

Figure 20. Torque Measurement Instrumentation.

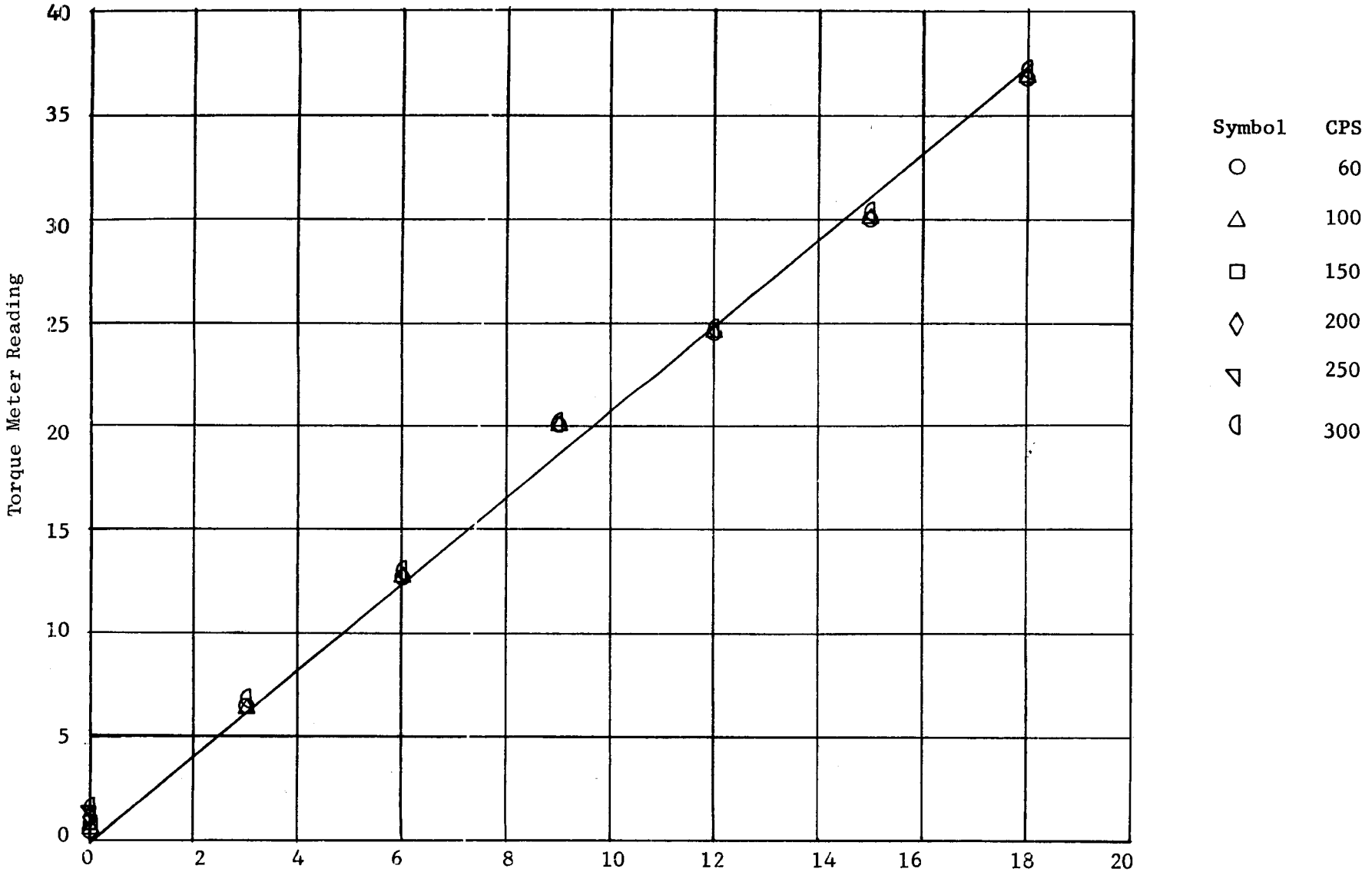

Figure 21. Torque Readout System Calibration.

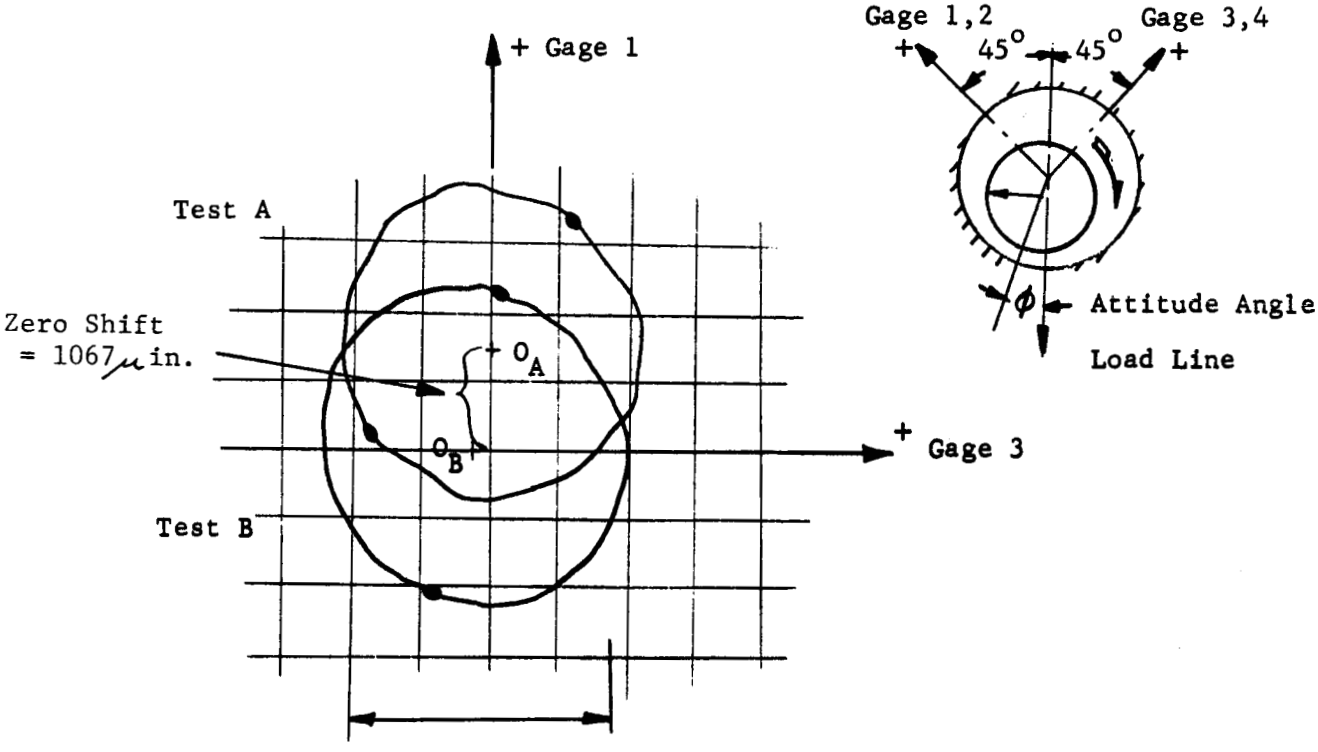

Calculated Brg. Diametral Clearance = 3 mils
0.2 volt/Cm. Scope sensitivity; 0.25 volts/mil gage-scope calib.

Gage zero shift with speed

Two axial groove bearing L/D = 1

3 mil diametral clearance shaft

Data of November 4, 1963

Test A - Half frequency whirl at 17.5 cps shaft speed

D.C. voltmeter readings

#1 gage - 1.8V calibration .09628 mils/volt
#3 gage - 2.3V calibration .09706 mils/volt

Test B - Half frequency whirl at 168 cps shaft speed

D.C. Voltmeter readings

#1 gage - 13.2V
#3 gage - 3.8V

Figure 22. Gage Zero Shift with Speed.

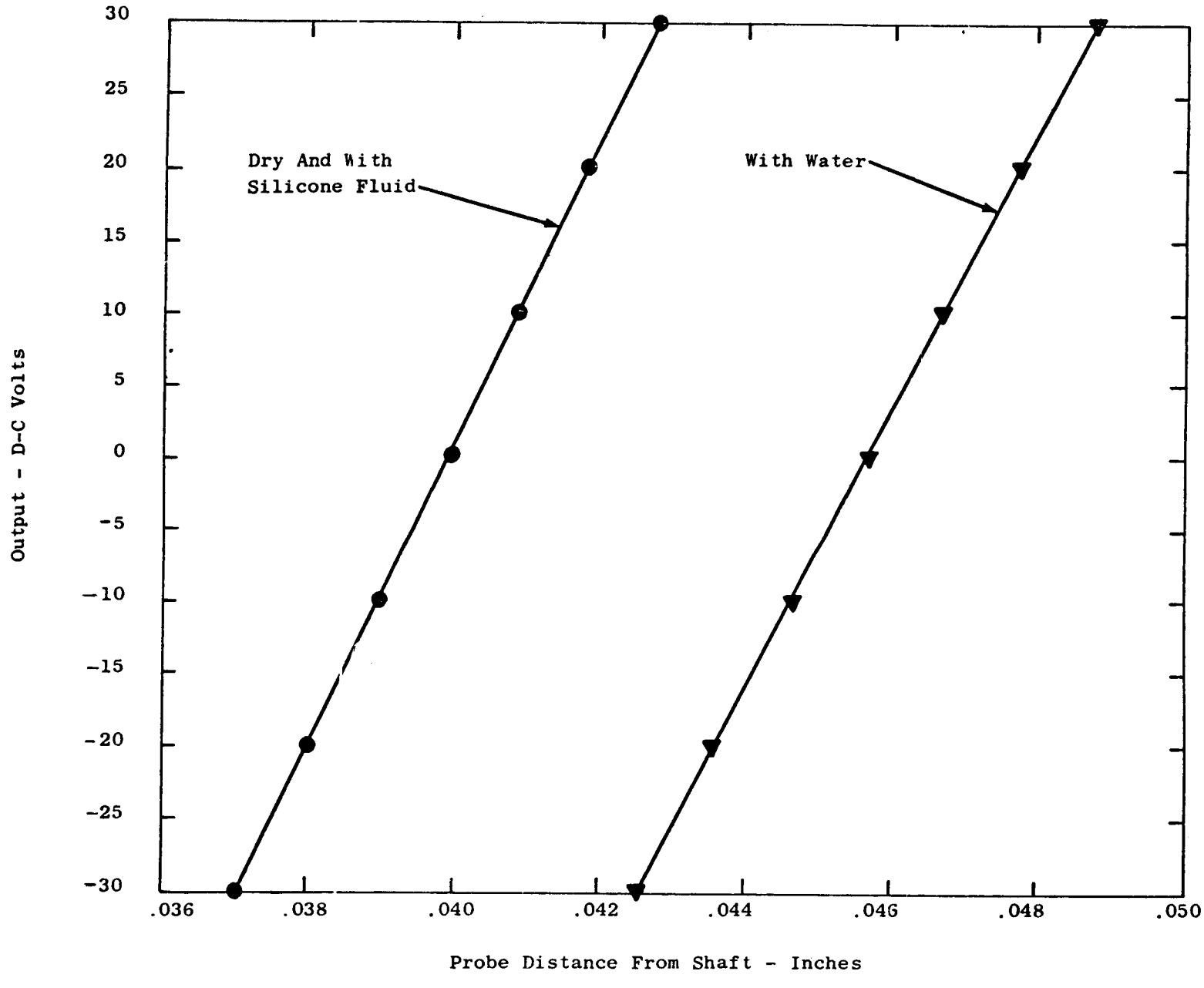

Figure 23. Proximity Gage Calibration Curve for Various Media.

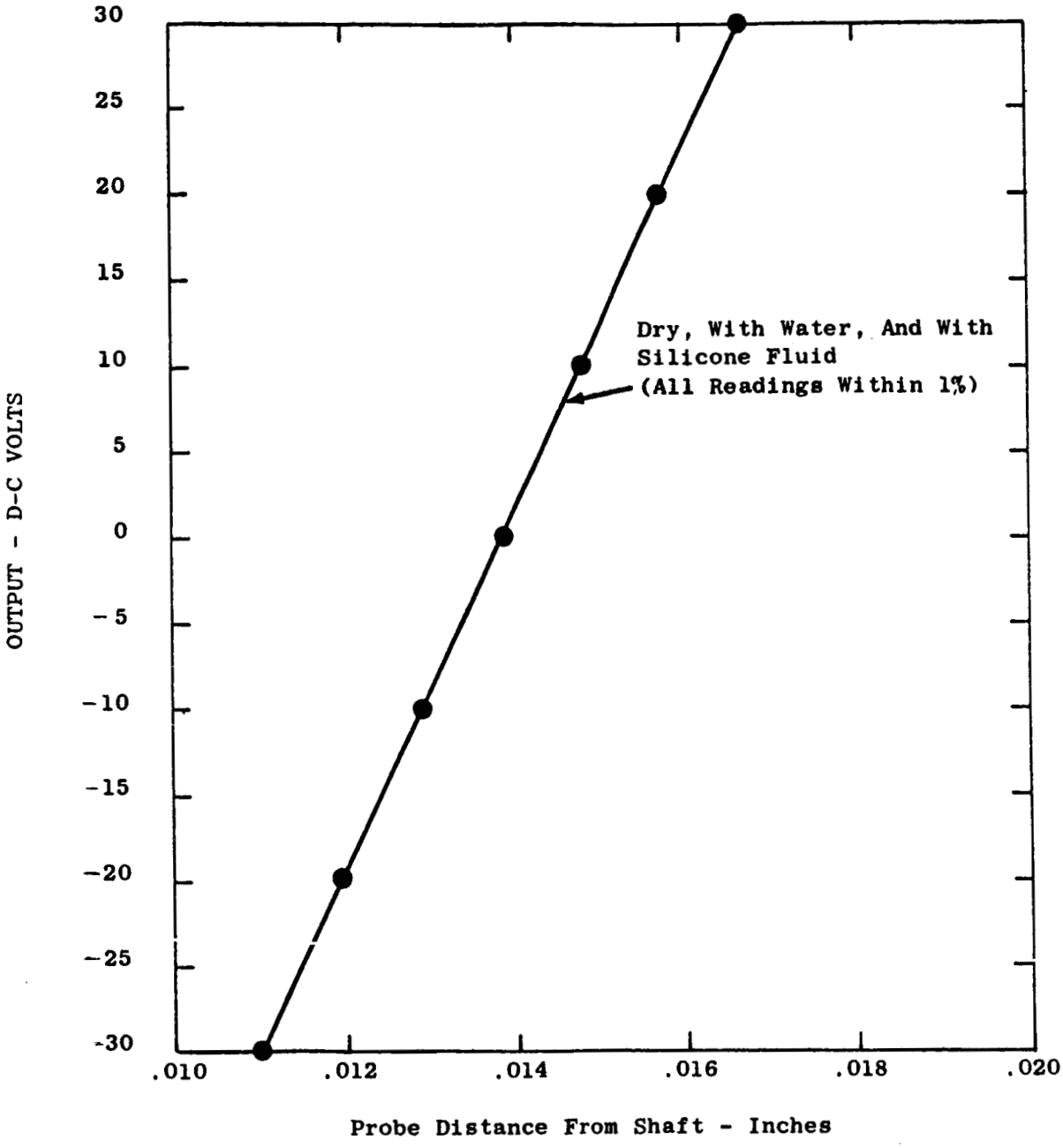

Figure 24. Proximity Probe Calibration Curve, Probe Tip is Shielded With a Teflon Cap.

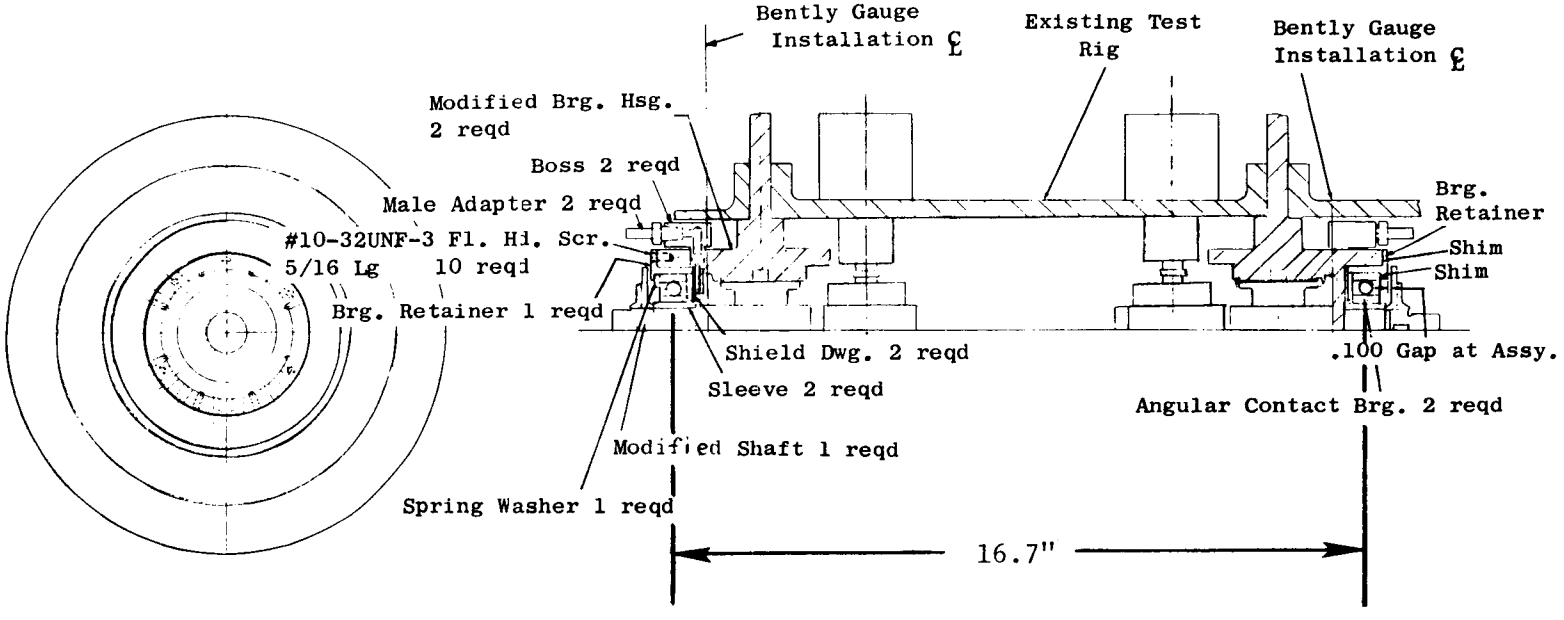

Figure 25. Gauge Check-Out Test Rig.

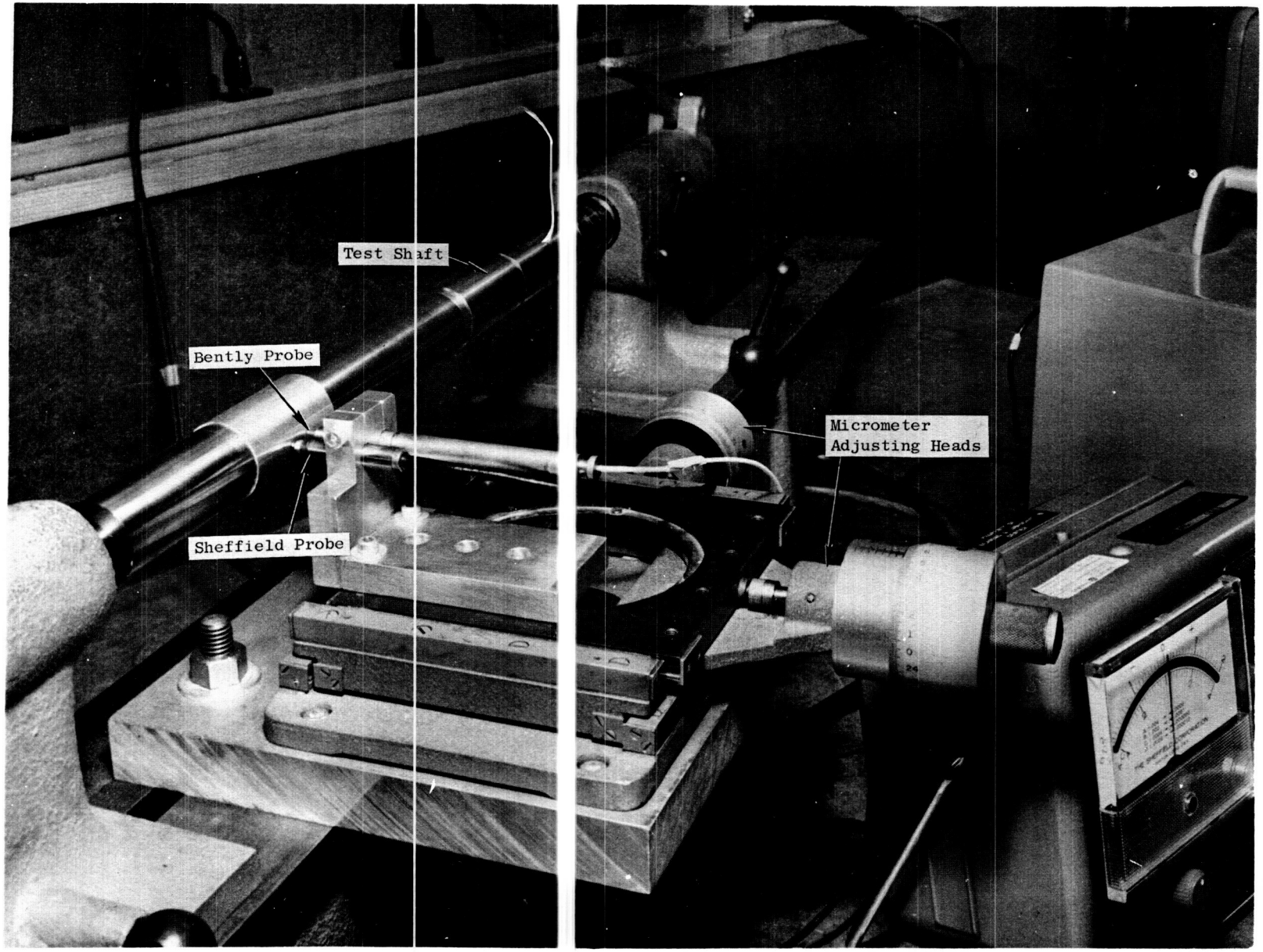

Figure 26. C libration Test Device

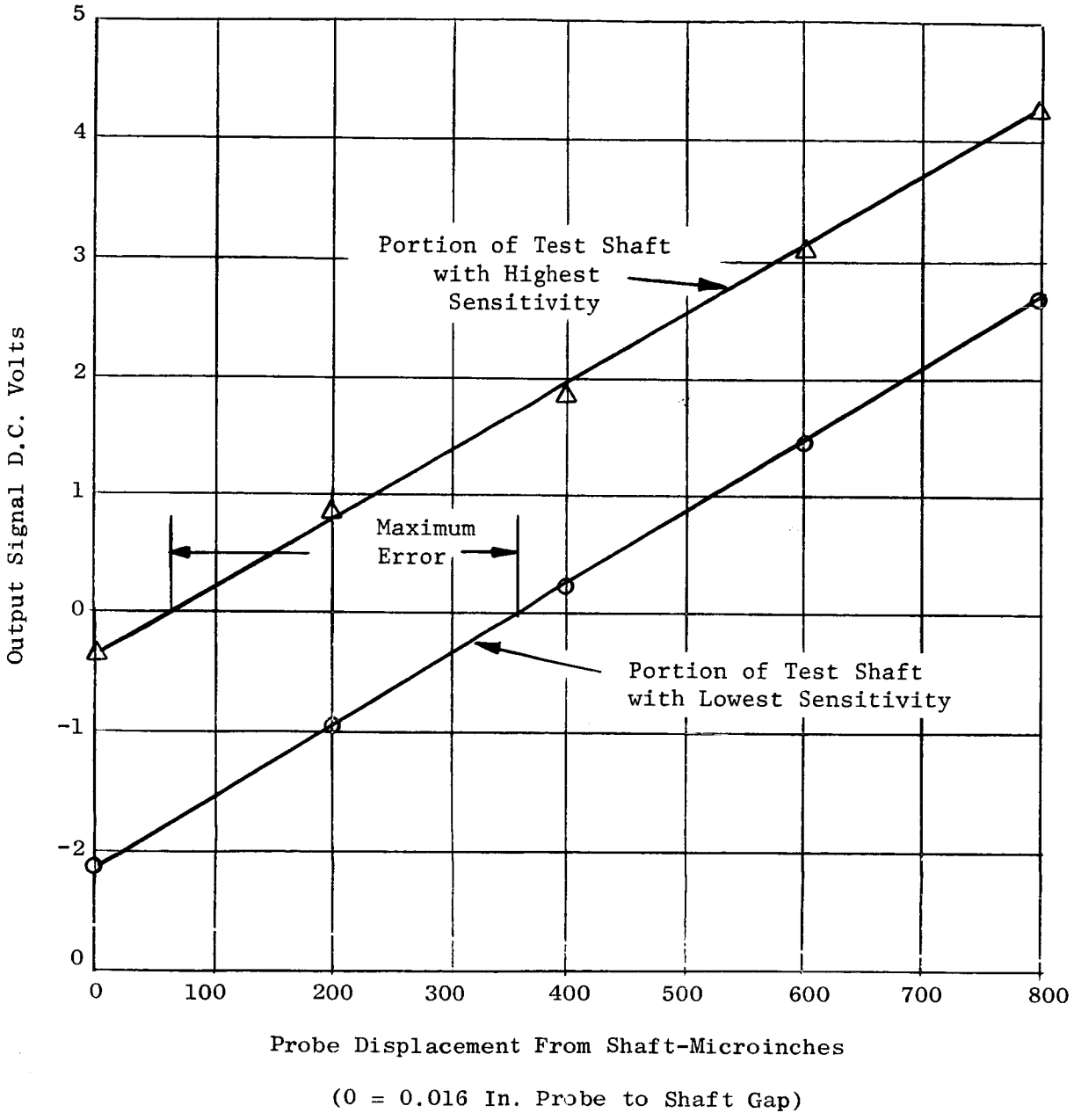

Figure 27. Maximum Variation in Bently Probe Calibration Over the Circumference of a 420 S.S. Shaft Because of Non-homogeneities in the Shaft Material.

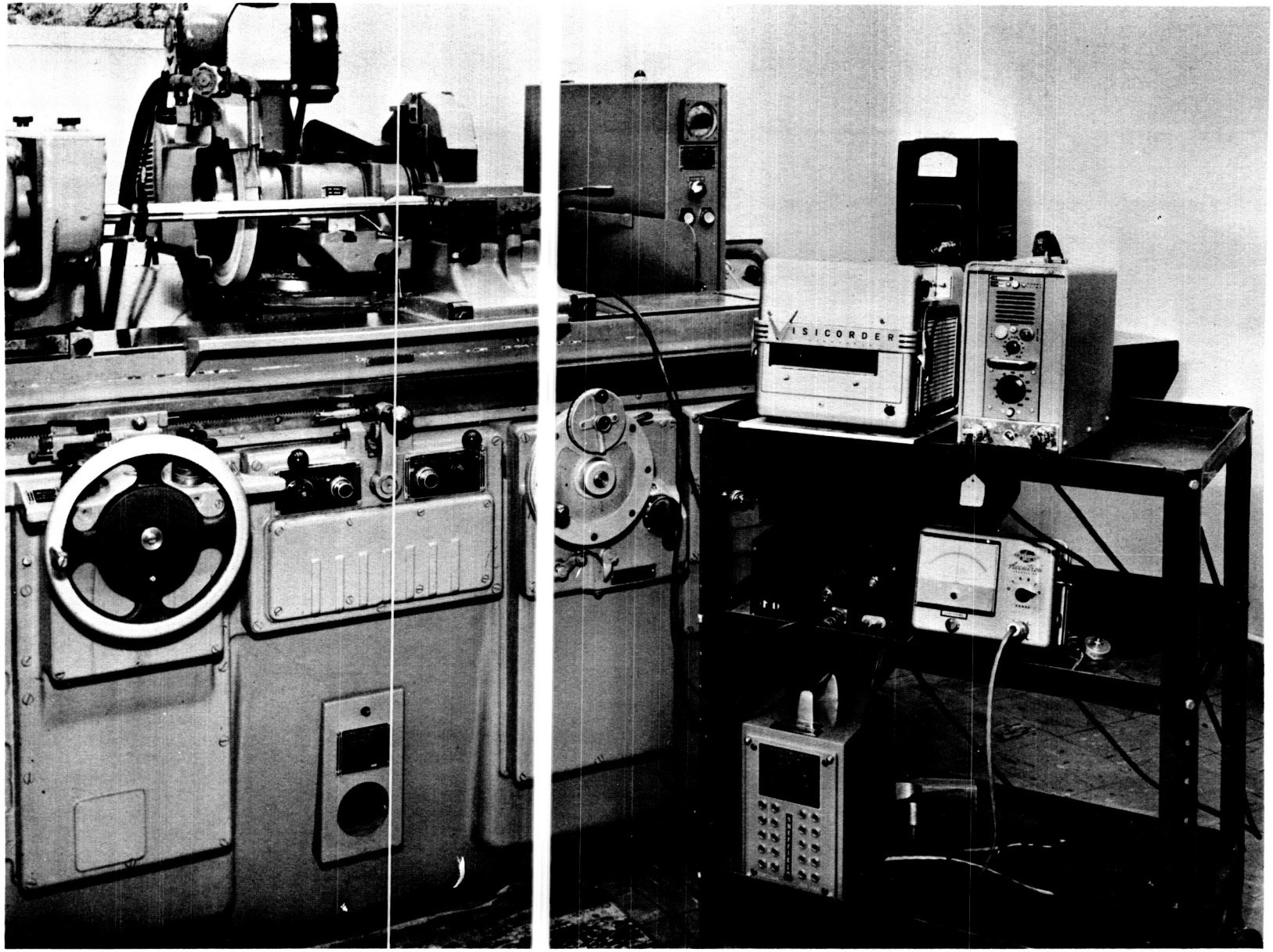

Figure 28. View of Grinder Used in Shaft Runout Measurements.

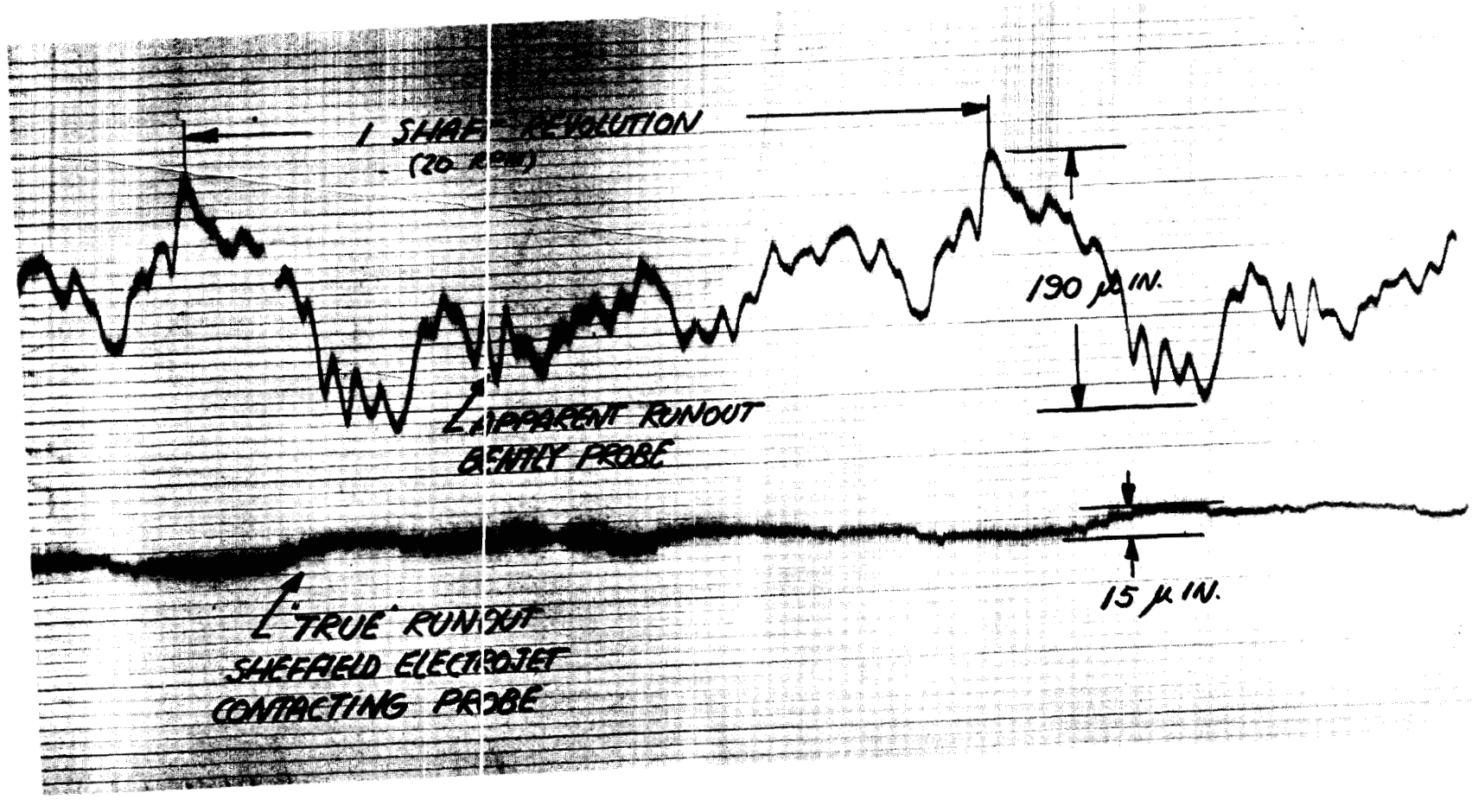

Figure 29. True and Apparent Shaft Runout. Type 420 S.S. Shaft 1.25" Dia.

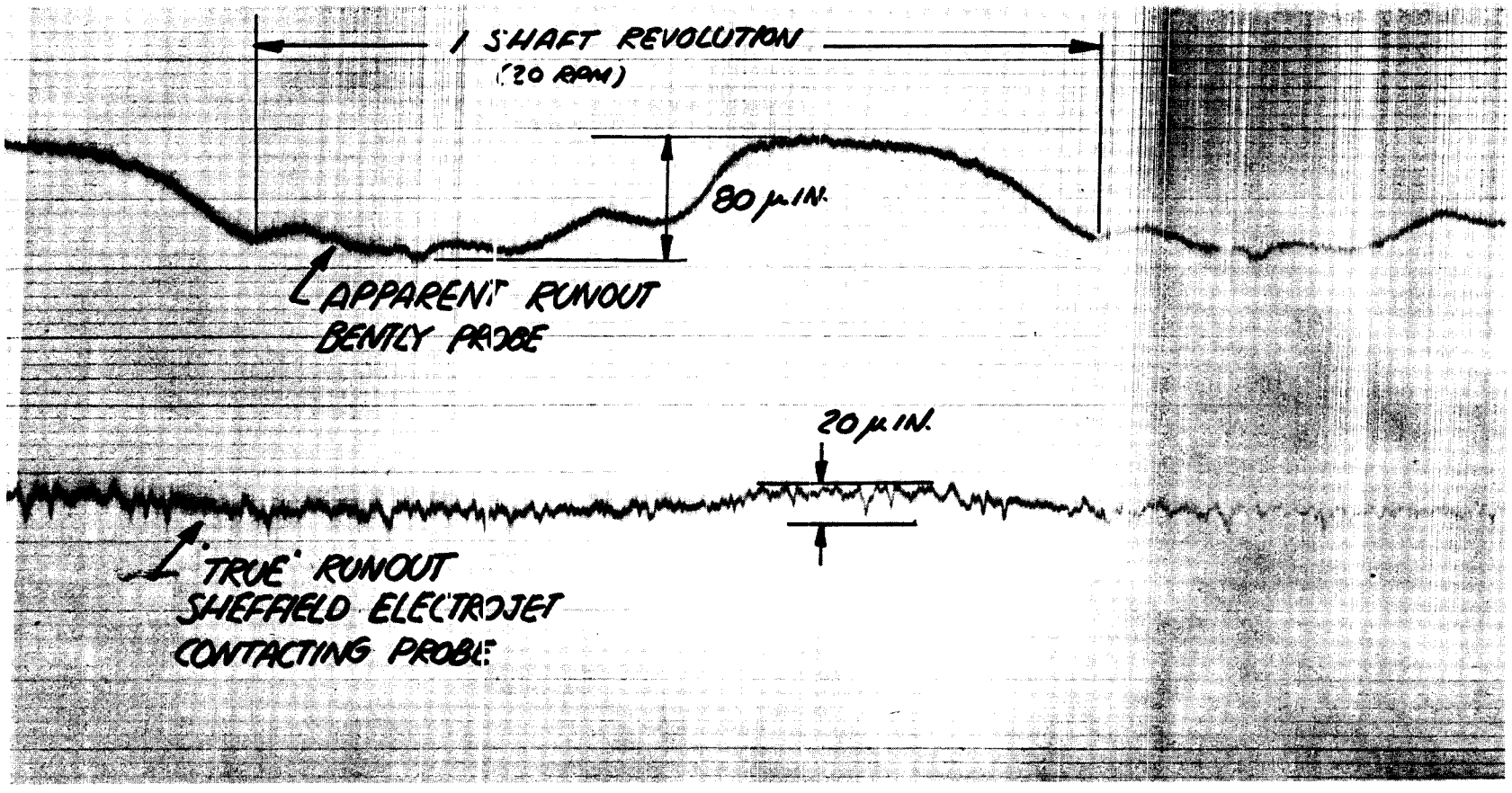

Figure 30. True and Apparent Shaft Runout. Type 420 S.S. Shaft 1.25" Dia. With Silver Plate 0.010" Thick.

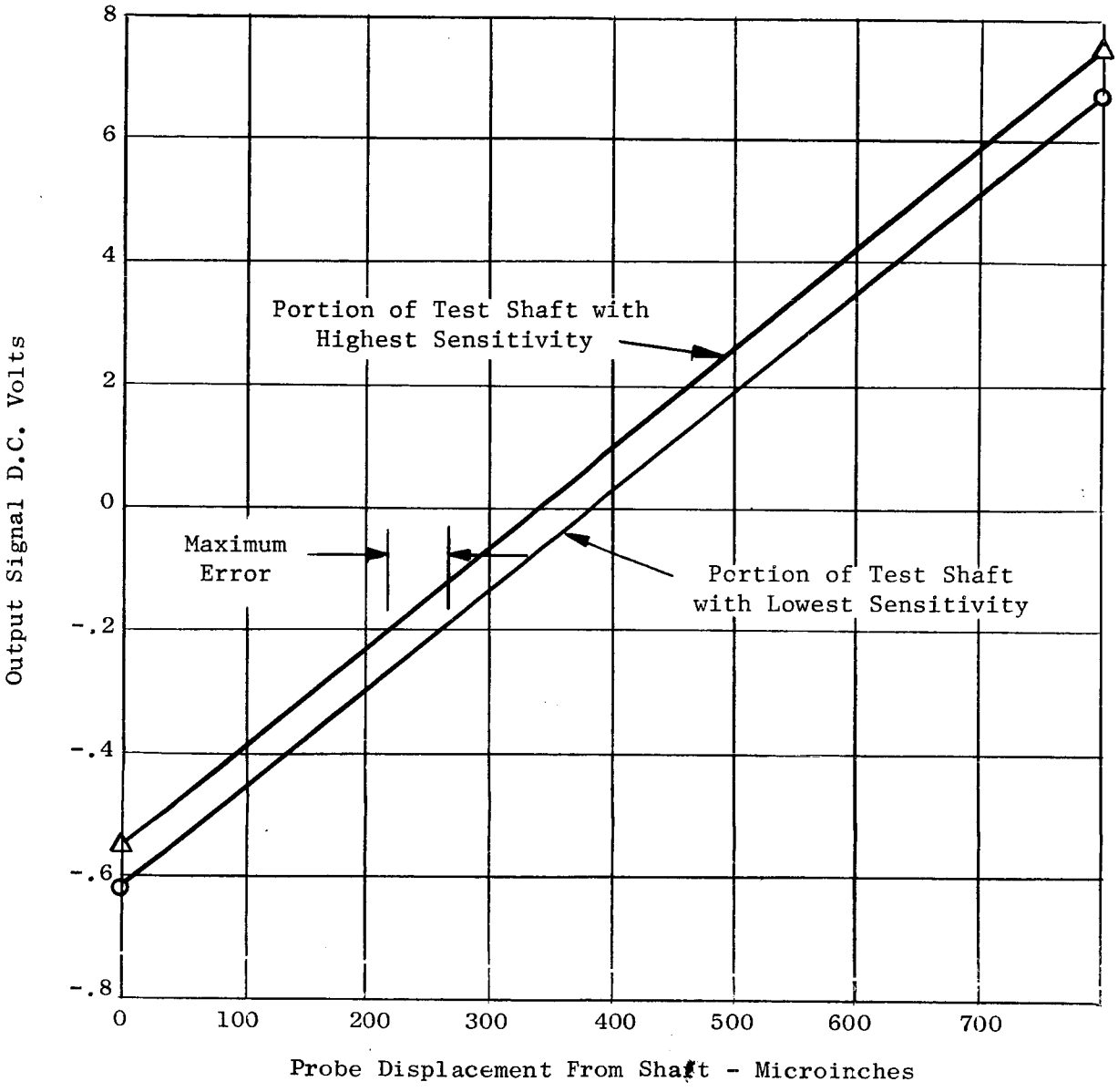

Figure 31. Maximum Variation in Bently Probe Calibration Over the Circumference of a 420 S.S. Shaft Overlaid with 0.005 Inch Silver Plate Because of Non-homogeneities in the Plating.

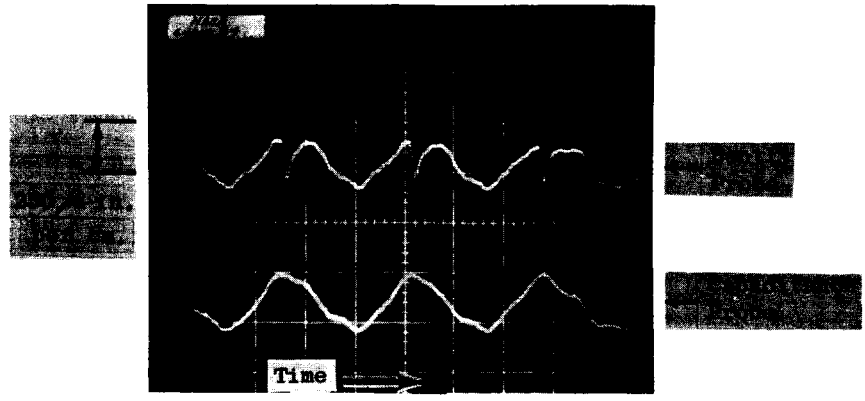

11,400 RPM

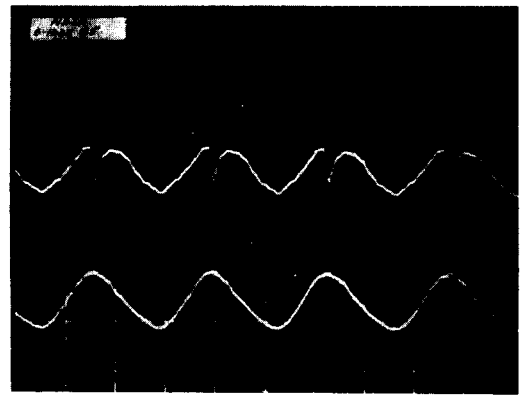

12,440 RPM

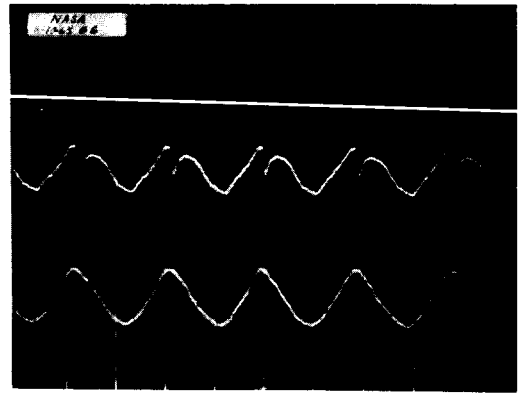

14,600 RPM

Figure 32. Comparison of Shaft Runout Measurements Bently and Capacitance Probe at Various Speeds.

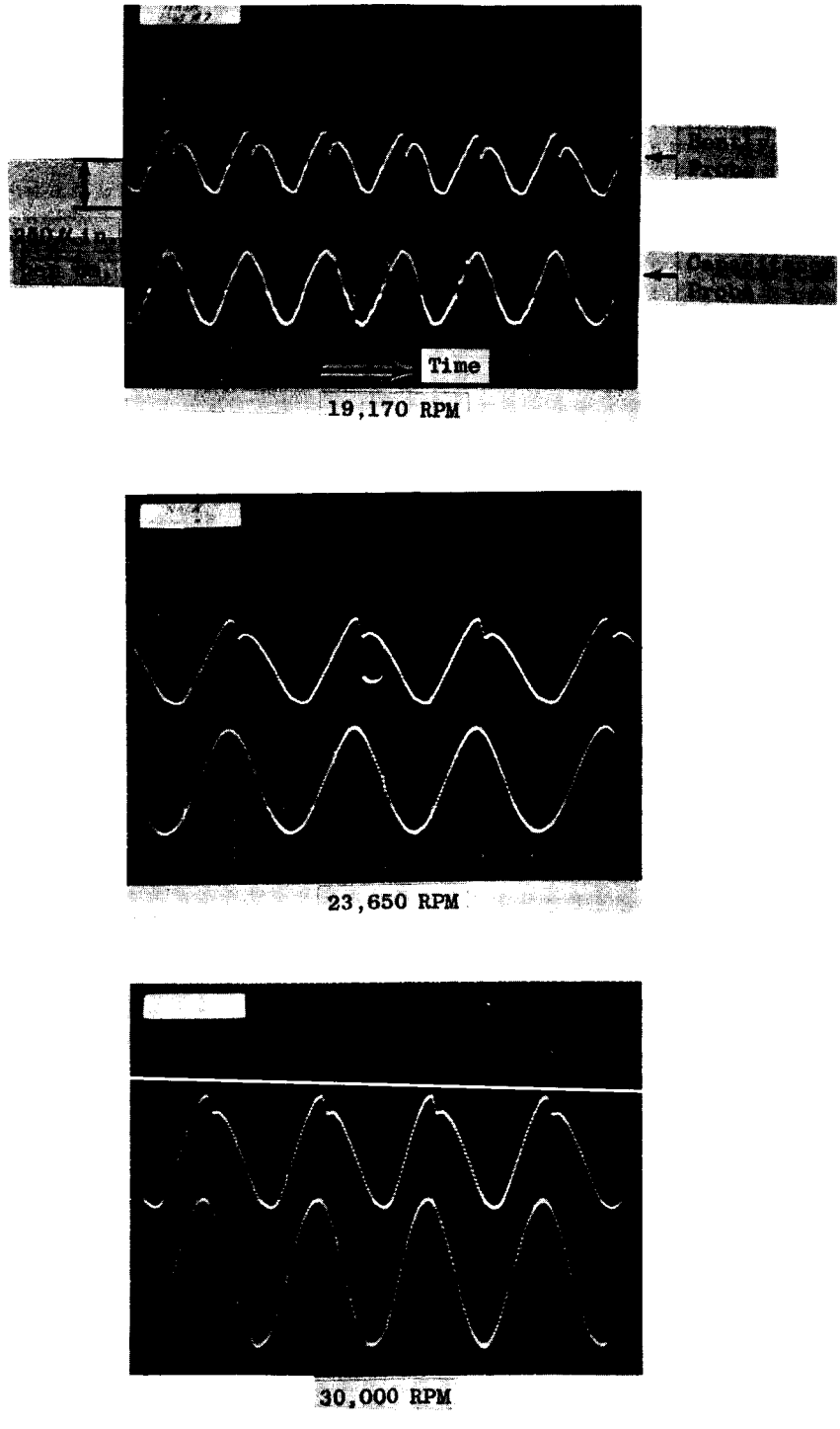

Figure 33. Comparison of Shaft Runout Measurements Bently and Capacitance Probes at Various Speeds.

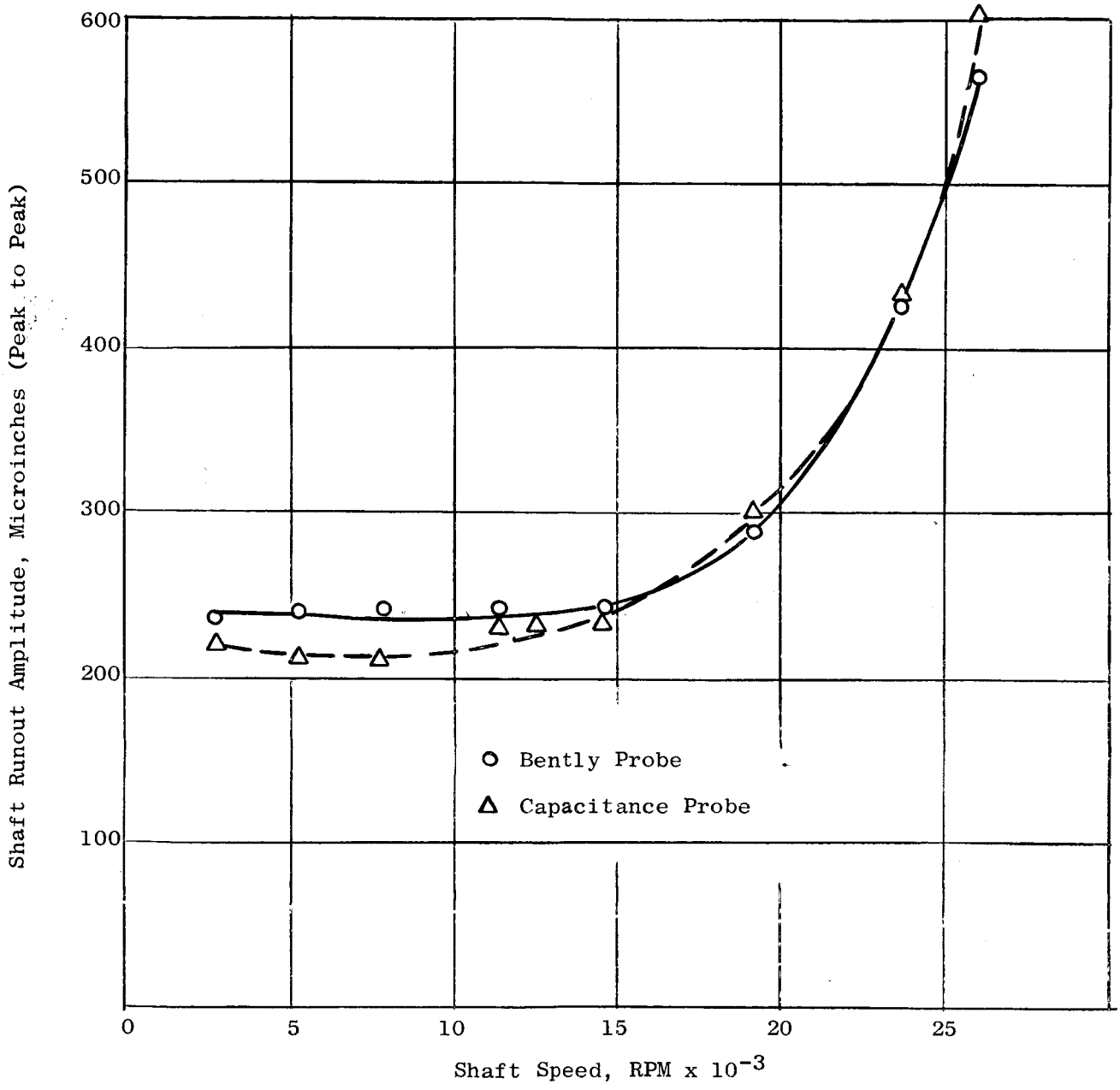

Figure 34. Comparison of Shaft Runout Measurements Using Bently and Capacitance Probes.

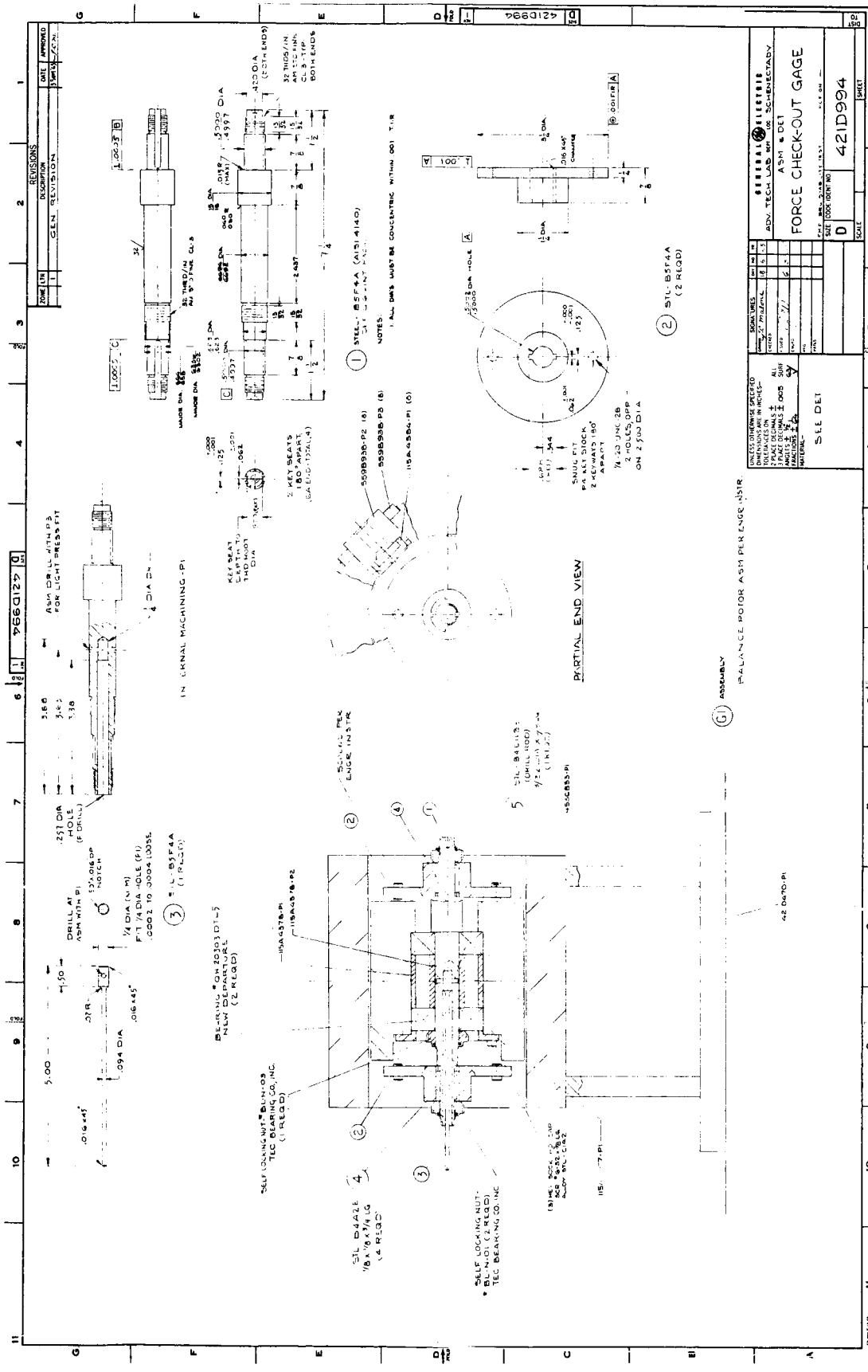

Figure 35. Force Check-out Gauge

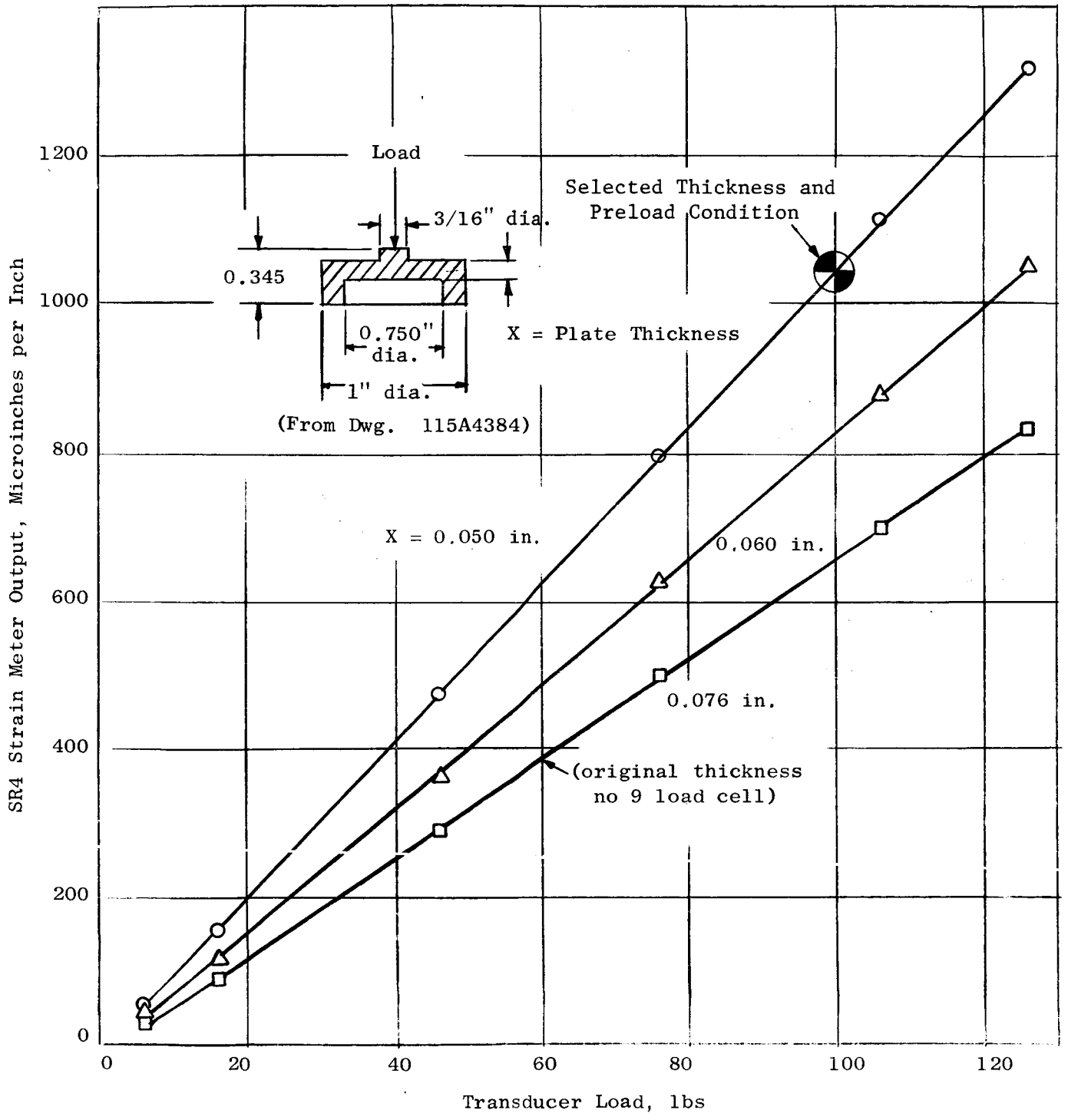

Figure 36. Force Gauge Calibration Curve.

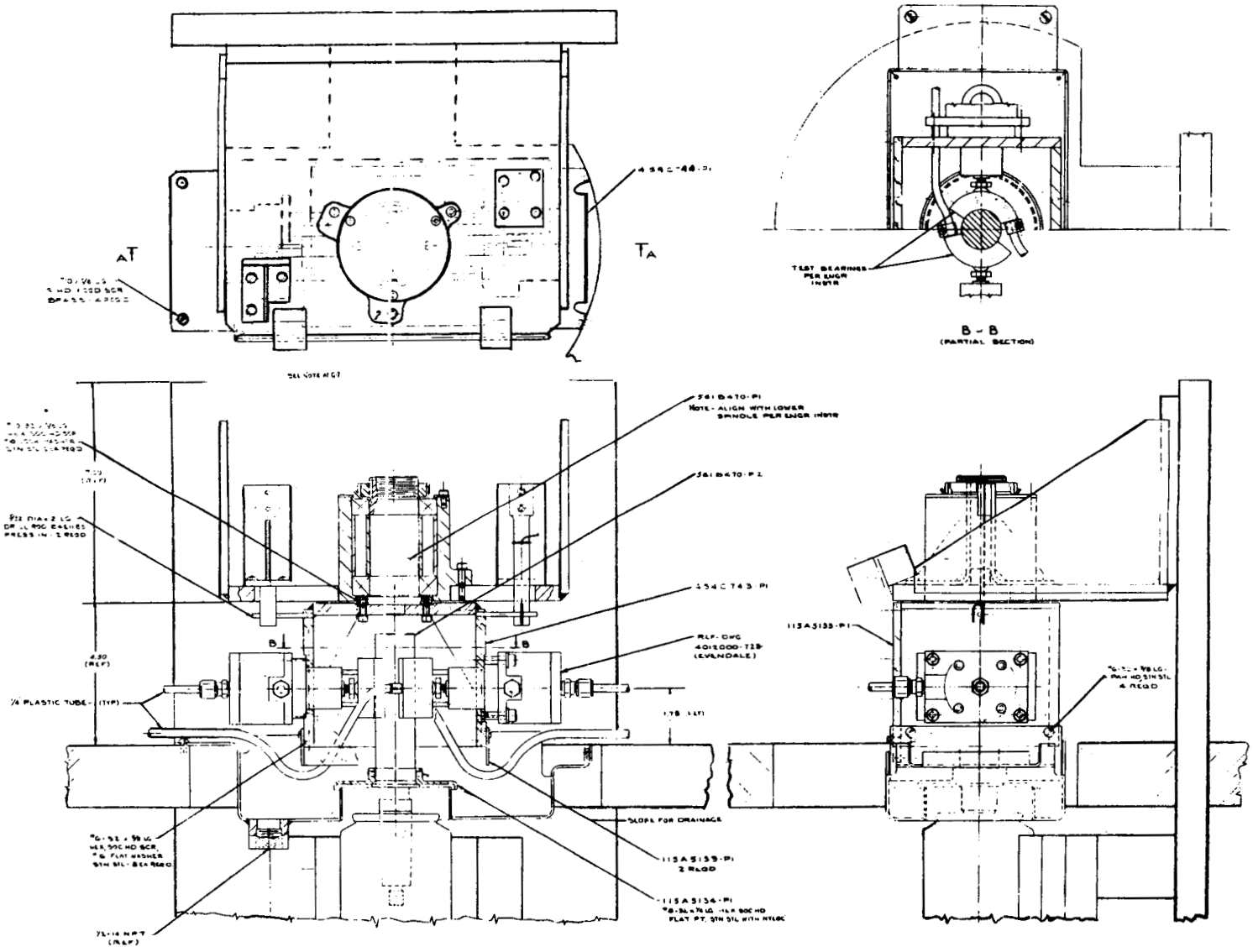

Figure 37. Test Rig for Measuring Loader Bearing Friction Torque.

APPENDIX A

ANALYSIS NOMENCLATURE

a_j	Major axis of ellipse	in.
A	$= K_{xx} - i\omega C_{xx}$	lbs/in.
b	Distance between bearings	in.
b_j	Minor axis of ellipse	in.
B	$= K_{xy} - i\omega C_{yx}$	lbs/in.
C	$= K_{yx} - i\omega C_{yx}$	lbs/in.
C	Radial clearance, according to text	in.
D	$= K_{yy} - i\omega C_{yy}$	lbs/in.
F	Force	lbs.
K	Pedestal stiffness	lbs/in.
M	One-half the rotor mass	lb-sec^2/in.
m	Bearing mass	lb-sec^2/in.
m_o	Unbalance mass	lb-sec^2/in.
$\bar{P}$	Force vector	lbs.
$\bar{Q}$	Unbalance force vector (equation 6)	lbs.
$\bar{q}$	Unbalance force vector (equation 7)	lbs.
$\bar{R}$	Displacement vector (translational mode, equation 4)	in.
U	Displacement amplitude (rotational mode, x-component)	in.
V	Displacement amplitude (rotational mode, y-component)	in.
W	Load	lbs.
$\bar{W}$	Displacement vector (rotational mode, equation 4)	in.
X	Displacement amplitude (translational mode, x-component)	in.
x	Displacement, x-component	in.
Y	Displacement amplitude (translational mode, y-component)	in.

APPENDIX A (CONTINUED)
ANALYSIS NOMENCLATURE (CONTINUED)

y	Displacement, y-component	
α	Angle between x and x'	degrees
α_{ab}	Influence coefficient, displacement at b due to unit force applied at a	in/lb.
α_j	Influence coefficients	in/lb.
S	Frequency ratio at threshold of instability	dimensionless
δ_o, δ_1	Unbalance eccentricity	in.
$\bar{\delta}$	Statical displacement vector	in.
ξ, η	See Figure 4	dimensionless
ν	Self-sustained vibration frequency at threshold of instability	dimensionless
ϕ	Phase angles (see Figure 3)	degrees
ψ	Angle between unbalance vectors	degrees
ω	Rotational speed	rad/sec.
ω_{ns}, ω_{np}		rad/sec.

Superscripts

$(\bar{\ })$	Dimensionless quantity of (nonvectorial)
$(\dot{\ })$	Time derivative

Subscripts

x, y	x - and y - components
c, s	cosine - and sine - component
o	Rotor mass station
s	Journal station

Subscripts (Continued)

b Bearing station

q Unbalance station

j = 1, 2, ...8 Station number as shown in Figure 4

APPENDIX B

NASA DYNAMICS INSTRUMENTS

1. Bently H-1-084-3 Sensors
2. Bently D-152 Detectors
3. Summing Amplifiers - Donner 3400
4. Readout - Fluke Voltmeter Model 801B
5. Readout - Tektronix 561A Oscilloscope
6. Wave Analyzer - General Radio Type 736A
7. Phase Meter Type 320-A - Technology Instrument Corporation
8. Ellis Bridge Amplifier Meter - Model BAM-I
9. Kintel D.C. Amplifier Model 111 BF
10. Hewlett Packard 521C Frequency Ccunter
11. Electro Products 3010 AN Magnetic Pickup
12. Brown Model 153X62P16-X-50 Recorder
13. Lube Temperature Control - Taylor 162RM131 Controller
14. Bearing Lube Flow - Brooks Rotameter Type 8-1110-10
15. Ashcroft Duragage
16. Sheffield Accutron Amplifier Readout for Electrojet Displacement Sensor - Model 51 #1530

APPENDIX C

PROCEDURE FOR SILVER PLATING CALIBRATION TEST SHAFT

420 Stainless Steel

Silver Plating

1. Anodic Electrolytic Cleaning
   Rinse
2. Nitric + Hydrofluoric Acid Etch
   Rinse
3. Fluoboric + Hydrofluoric Dip
   Rinse
4. Vapor Blast
   Spray Rinse
5. Nickel Strike
   Rinse
6. Silver Strike
7. Silver Plate
   Rinse + Dry
8. Grind to Tolerance
9. Apply "Tarniban"